UNIVERSITY OF ADELAIDE LIBRARY
18/12/03

University of Adelaide

School of Chemical Engineering

A Mie Scattering Investigation of the Zones of Soot Formation in Precessing Jet Flames

M.Sc. Thesis

Lilia Ilinichna Stamatova

2003

Abstract

This is an experimental study of soot formation in mechanical precessing jet (MPJ) burner flames. The Mie diagnostic technique was implemented to provide qualitative visualisation of the zones of soot formation. A range of conditionally sampled experiments was carried out. The characteristic Reynolds number based on the nozzle diameter, was varied from 4329 to 11223 and the Strouhal number based on the nozzle diameter, was varied from 0.0042 to 0.0245. The nozzle diameter was fixed at 5 *mm* and the jet exit angle at 45 degrees.

Experimental data were collected and used to perform semi-quantitative soot volume fraction calculations. The semi-quantitative measurements of soot intensity show that it increases with increase in both *Re* and *St* numbers, however, the latter is more influential.

The instantaneous images reveal that soot is predominantly formed in sheets of varying thickness, often reaching 30-40 *mm*. Very little soot is observed in the near nozzle region, which is consistent with the idea that the formation of soot in appreciable quantities is kinetically limited. Readily observable are very broad regions of low signal spanning much of the flame. These broad regions are more prevalent in the high *St* number flames where strain rates are lower and residence times are longer.

The experimental results support the hypothesis that low strain in a diffusion flame promotes soot formation and high emissivity (ie. soot formation correlates inversely with flame strain).

Table of Contents

Table of Contents

Table of Contents

Figures

Page

Table of Contents

Statement of Originality

The material in this thesis is original and has not been submitted or accepted for the award of a degree or diploma at any other university and to the best of my knowledge and belief, the thesis contains no material previously published or written by another person except where due reference is made in the text of the thesis.

Lilia Ilinichna Stamatova

17 September 2003

Permission to Copy

The author consents to the thesis being made available for loan and photocopying provided that the thesis is accepted for the award of the degree.

Lilia Ilinichna Stamatova

17 September 2003

Acknowledgments

Firstly I would like to thank to my husband - Dr. Venelin Stamatov and my son - Alexander whose unlimited support I could trust even in the hardest times.

This thesis has been made possible by the efforts, enthusiasm and support of many people. The supervisors of the project, Professor Keith King, Associate Professor Gus Nathan and Dr. Zeyad Alwahabi have provided unbounded enthusiasm and inspiration, which have had a profound influence on this document.

The work that is presented here has made use of new experimental facilities that have been established through the efforts of the technical staff in the School of Chemical Engineering. All the technical staff, in particular Mr. Peter Kay, made the contributions. The academic, clerical, and technical staff of the School of Chemical Engineering deserve my gratitude.

I would like to express my gratefulness to the University of Adelaide for providing partial financial support for the project.

Lilia Ilinichna Stamatova

17 September 2003

1. Introduction

The conversion of fossil fuels into energy is the most important chemical process used in stationary and mobile combustion devices. The detailed knowledge of all combustion phenomena in such combustion devices is therefore highly relevant. The limited resources of fossil fuels and the undesirable formation of air pollutants demand efficient control over the combustion processes. The interaction of the chemical kinetic system with its vast number of steps that describe the chemistry of combustion, with the dynamics of the fluids complicates this control. The process of formation of soot is the most complex process in flames because the soot particles, containing several thousands of carbon atoms are formed from simple fuel molecules within a few microseconds and the high number of molecules and particles, of different form and size, involved in this process can not be quantified. However, there are such diagnostic techniques as Laser-Induced Incandescence (LII) and Mie scattering technique that allow quantitative (LII) and semi-quantitative measurements (Mie scattering) of the soot intensity and its spatial distribution - a knowledge that is central to understanding of this combustion process.

The formation and destruction of soot (formula $\sim C_{8n}H_n$) is an important feature of non-premixed (diffusion) hydrocarbon/air flames. Soot particles are a primary source of the luminosity of such flames, contributing to radiant heat losses from the flame with peak emissions at wavelengths in the infra-red region of the spectrum. In processes where radiant heat transfer is desirable, such as in furnaces and boilers, soot formation during combustion is also desirable. As an example, in cement kilns heat is transferred from a flame to the bed and to the rotating walls of the kiln by radiation, which then transfer the heat to the reactants via conduction. However, the combustion in such flames is often not 100% complete and, if not optimised or controlled, can result in the emission of soot that exceed permitted norms, thus causing environmental problems.

1.1. The Precessing Jet Phenomenon

The mixing field produced by a nozzle affects the specific fuel consumption, the level of emissions and the excess air required, all of which should be minimised in industrial applications. An interesting engineering technology that allows high luminosity and low level of soot and NO_x emissions from a flame is realised in the Fluidic Precessing[1] Jet (FPJ) burner. The FPJ burner produces large-scale vortical roll-ups close to the nozzle exit plane, allowing pockets of air to be engulfed within the gas envelope without using high velocity gas or air jets. Fuel-rich combustion is deduced to take place locally in pockets within the gas envelope, resulting in cracking of the natural gas and the creation of intermediate soot particles, thereby creating a highly luminous flame. A schematic diagram of the FPJ nozzle is shown in Figure 1-1.

The precessing jet phenomenon is generated naturally by a fluid mechanical instability which results from the fluid passing through an orifice plate or nozzle and undergoing a large abrupt expansion in a short cavity. As the jet passes through the small orifice and into the

---

[1] The term "precession" is used here to describe the gyroscopic-like motion of a jet about an axis other than its own.

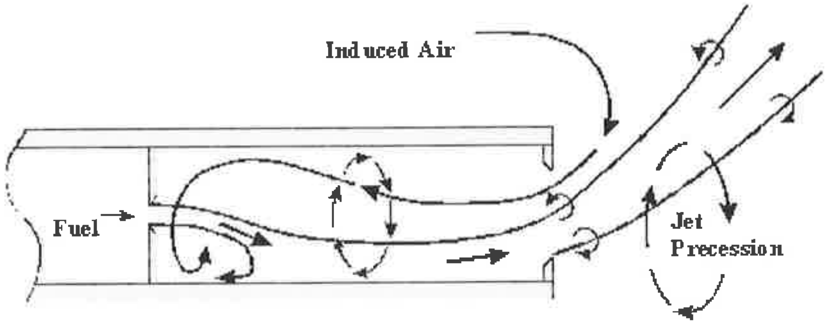

Fig. 1-1. Basic configuration of the Fluidic Precessing Jet (FPJ) nozzle and the flow patterns within it.

chamber, it experiences a sudden expansion. This produces a jet which then asymmetrically re-attaches to the inside wall of the chamber where it remains attached until it approaches the exit lip, at which point it separates before being deflected at an angle of about 60° across the nozzle axis. As the deflected jet leaves the chamber it precesses, and stabilisation of the flame occurs within the region immediately downstream from the nozzle exit[1].

While the efficacy of the FPJ burner has been proven in practice, its very nature means it is difficult to study at the fundamental level. This difficulty arises because the flow field it produces is continuously unstable, which is believed to be the source of the efficacy. In order to aid in understanding the mechanisms of the precessing jet flow, the mechanical precessing jet (MPJ) burner that simulates important aspects of the FPJ burner was developed in the School of Mechanical Engineering, at the University of Adelaide. The MPJ flame is well suited to providing further insight into the relationship between mixing, radiation, soot

---

[1] Further details can be found in Parham *et al.* (2000).

formation and NO emissions because it allows a wide range of flame strains to be generated with constant jet Reynolds number and fuel flow-rate. Further details of the MPJ burner can be found in Chapter 3.

1.2. Objectives of the Current Work

[Because of the relative simplicity of the experimental system and high level of the signal, the Mie scattering technique will be used to explore the structure of soot in flames whose turbulence structure is modified by precession for different conditions of flow and frequency of precession.] An MPJ burner that allows the parameters that determine the mixing field, such as jet diameter, exit velocity, frequency of precession, and deflection angle to be varied independently, will be used as a source of the required turbulent non-premixed flame.

Data about the dependence of the soot intensity on important parameters that determine the mixing field (exit velocity and frequency of precession) will be collected. The relationship between flame strain and soot formation, and its role in radiant heat transfer will be assessed.

1.3. Thesis Overview

The basic principles of Mie scattering technique, the generally accepted theories about the origin of soot in flames, and the experimental methods are described in Chapter 2.

The experimental equipment, procedures and sources of error used in the present study are described in Chapter 3. This includes a concise description of the experimental operating procedure, the safety operating and personal protection requirements. The data correction procedure is also given in this chapter.

The semi-quantitative measurements of soot intensity and their correlation with flame strain are presented and discussed in Chapter 4.

Conclusions are given in Chapter 5 together with the plans for future development of the findings of the current work.

Finally, Appendix A gives a broad selection of images at various experimental conditions, while Appendix B provides the results from a visual examination of zones of high luminosity.

This work contains 22 Figures, 7 Tables and 2 Appendices. A Thesis Map illustrates the structure of the current work.

1. Introduction

Thesis Map

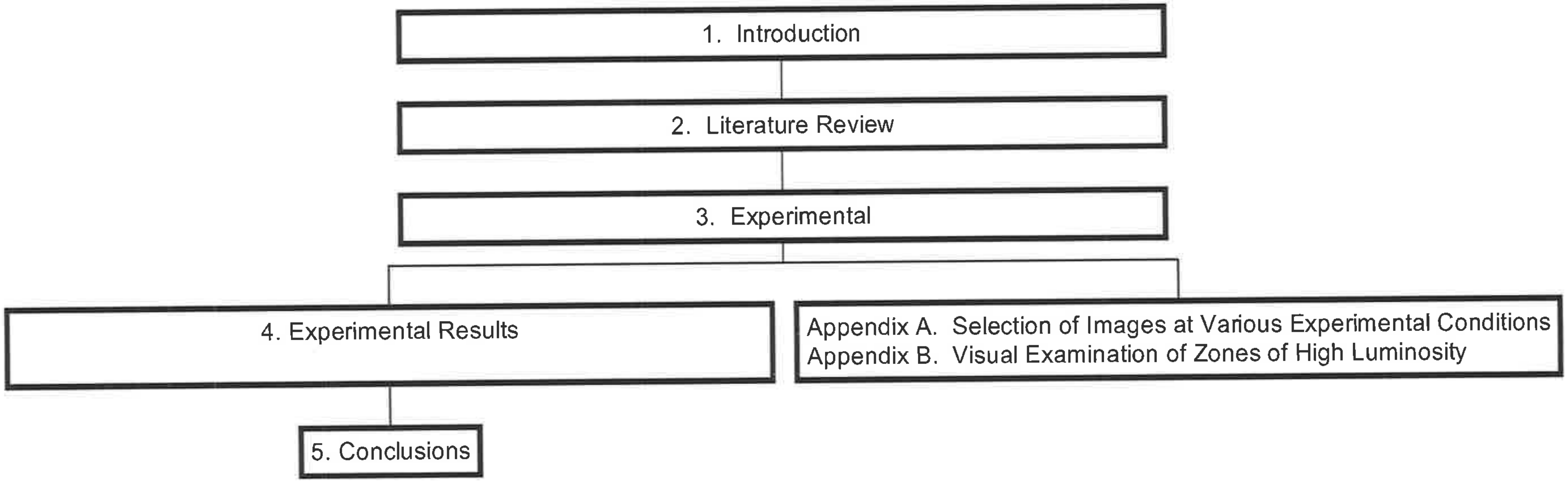

2. Literature Review

2.1. Soot Diagnostic Techniques

Generally, the techniques that allow imaging in a two-dimensional plane include LII[1] (eg. Eckbreth (1977), Melton (1984) and Shaddix *et al.* (1996)), Mie scattering (eg. Chao *et al.* (1990) and (1991), Clemens *et al.* (1991)), Raman scattering (eg. Schefer *et al.* (1994)), Rayleigh scattering (eg. Everest *et al.* (1995)) and Planar Laser Induced Fluorescence (PLIF) (eg. Dimotakis *et al.* (1983)). Fundamental elements of the layout of the experimental apparatus are the same for all of these techniques. The essential ingredients are a sheet of light produced by a laser beam, suitable optics through which the beam is passed and a detector, which can be a solid-state array or photographic film. The beam produced by the laser generates a signal either by scattering from particles or molecules or by excitation of species within the flow field. The signal is collected by the detector and is stored for processing.

A comparison of the relative signal strengths from an analysis by Eckbreth (1988) of comparable experiments using the various laser diagnostic techniques is shown in Figure 2-1. It highlights that the Mie scattering signal is orders of magnitude larger than the signal from Raman and Rayleigh scattering, and PLIF.

---

[1] LII uses pulsed laser excitation to heat soot to far greater temperatures than the flame and exploits the resultant emission. The laser light is directed through the flame in a line or sheet. The temperature of a soot particle rapidly rises to its vaporisation temperature, roughly 4000 K, for high laser intensities. The particle thermal emission at these elevated temperatures increases and shifts to the blue, in contrast to the non-laser-heated soot and flame gases. One- and two-dimensional imaging measurements can then be made with a gated, intensified array camera.

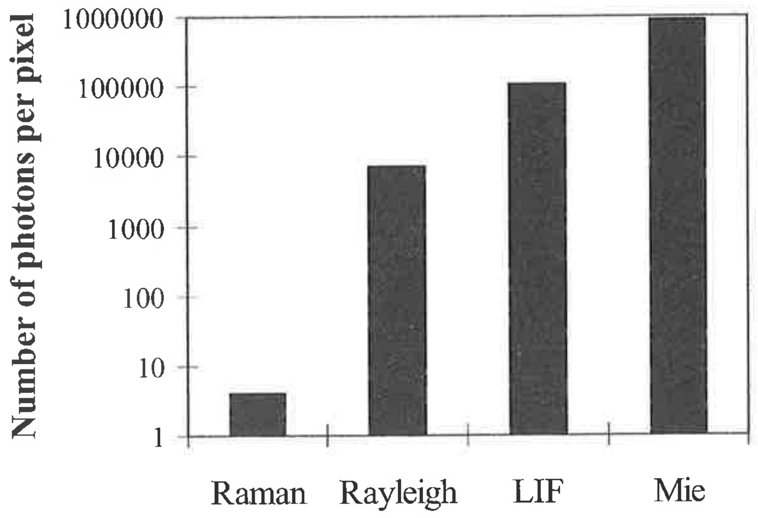

Fig. 2-1. A comparison of signal strength for different laser diagnostic techniques, after Eckbreth (1988).

Techniques suitable for instantaneous mapping of the soot distribution in flames are LIF and Mie scattering. There are many practical benefits of using LIF for soot concentration measurements. With proper calibrations and choice of detection wavelength, detection gating/duration, and laser intensities, the LIF technique is believed to be ideal for use in flames that produce large gradients in soot concentrations and for determining instantaneous soot distributions in turbulent flames. However, LII requires undesirable, very high laser energy outputs, with a typical value of 285 *mJ* per pulse, see Ni *et al.* (1995). This energy is two hundred times larger than the laser output energy required by the Mie scattering technique (typically a magnitude of ~1.30 *mJ*.). Thus, the major advantage of the Mie scattering technique is that it provides strong scattered signal, using relatively low laser output energy, or alternatively, stronger signal allows a larger sheet, and hence imaging of the entire flame, or significant section of it.

2.2. The Mie Scattering Technique

The technique of imaging a flow by scattering light from small particles is generally known as Mie Scattering, Lorenz-Mie Scattering or Marker Nephelometry. This technique is based on the phenomenon first mentioned by Mie (1908) that the scattering of a plane wave by a homogeneous sphere (the size of the sphere must be comparable with the wavelength) leads to the formation of a spherical wave. The Mie scattering technique is of special interest for the present investigation because of its high signal strength, enabling a large flow area to be investigated.

The feasibility of the technique for use in experimental investigations of flows was initially begun by Rosensweig *et al.* (1961) and further explored by Becker *et al.* (1963), (1967a) and (1967b). A detailed description of the theory and experimental application of the technique is reviewed by Becker (1977).

2.2.1. Experimental Methods

There are three basic methods for utilising Mie scattering to image selected regions of flows:

understood, there is a general consensus that soot is formed in the following four-step sequence:

1. Formation of precursor species. In this first step, Polyaromatic Hydrocarbons (PAHs) are formed as the precursor species, acting as an intermediary between the original fuel molecule and a primary soot particle. Chemical kinetics, rather than diffusion, dominate this step.
2. Particle inception. This step involves the formation of small, 3000–10000 atomic mass units (*a.m.u.*), particles by chemical means and from coagulation. It is in this step that the molecules are recognisable as particles.
3. Surface growth and particle agglomeration. This occurs as the small soot particles continue to be exposed to species from the pyrolising fuel as they travel through the flame.
4. Particle oxidation. This occurs when the soot particles pass through the oxidising region of the flame. If all the soot particles are oxidised, the flame is termed nonsooting, while incomplete oxidation gives rise to a sooting flame.

Fialkov (1997), Calcote *et al.* (1988), and Calcote *et al.* (1994) proposed that soot requires an ionic nucleus. On the other hand, Homann *et al.* (1967), Frenklach *et al.* (1987), and Frenklach *et al.* (1991) consider that charged species do not participate in these earliest stages of the production of soot; instead they have formulated reaction mechanisms involving only uncharged radicals and molecules.

Hayhurst *et al.* (1989) accepted that there could be both an ionic route to soot and another involving neutral species. Thus ions, formed in processes like

$$C_{16}H_{10} + C_6H \rightarrow C_{22}H_{11}^+ + e^-$$

some 2–3 *mm* downstream of the reaction zone of a hydrocarbon flame, have been proposed by Hayhurst *et al.* (1989) as nuclei for soot.

Fialkov (1997) proposed the following ionic route. The starting point is an ion such as $C_3H_3^+$, which, in all probability, is produced in the reaction zone of a hydrocarbon flame by

$$CH + C_2H_2 \rightarrow C_3H_3^+ + e^-$$

where one or other of the reactants might be (but is not required to be) electronically excited. Another likely source of $C_3H_3^+$ is proton transfer to the radical C_3H_2 from a flame ion such as CHO^+ (see Graham *et al.* (1984)). Ions such as $C_3H_3^+$, CHO^+, $C_4H_5^+$, $C_6H_5^+$, $C_7H_7^+$ and the polyacetylenic ions $C_xH_3^+$, with x up to ~8, appear very early in the reaction zone of a flame of a hydrocarbon burning in air, especially one rich enough to produce soot (see Hayhurst *et al.* (1982)). The maximum concentrations ($\sim 10^{11}$–10^{12} *ions* ml^{-1}) of these ions add up to almost the same order of magnitude as the concentrations of soot particles appearing downstream in the burnt gas. Thus, these natural flame ions appear to be likely nuclei for the production of soot. Also, Hayhurst *et al.* (1987) found that straight-chain ions could cyclise more rapidly than uncharged hydrocarbon radicals in a flame. After these primary ions have been formed, the ionic mechanism assumes there follows relatively rapid addition of C_2H_2

and C_4H_2 (commonly present in significant amounts in a flame sufficiently fuel-rich to yield soot) to the linear isomer of $C_3H_3^+$ in the following steps, (see Hall-Roberts *et al.* (2000))

$$C_3H_3^+ + C_2H_2 \rightarrow C_5H_3^+ + H_2$$

$$C_3H_3^+ + C_2H_2 \rightarrow C_5H_5^+$$

$$C_3H_3^+ + C_4H_2 \rightarrow C_5H_3^+ + C_2H_2$$

$$C_3H_3^+ + C_4H_2 \rightarrow C_7H_5^+$$

In some flames, other radicals such as C_2H, C_3H_2 and C_6H_2, may be reacting in a similar way with $C_3H_3^+$. Subsequently these positive ions continue to grow by further exothermic addition of C_2H_2, C_4H_2, etc., so that aromatic ions like $C_{13}H_9^+$ and $C_{19}H_{11}^+$ (with three and five rings, respectively) are found by Fialkov (1997) in the complex mass spectra. Eventually, but relatively quickly since ionic reactions can be faster than those of neutral species, ions with a mass of 2000 *a.m.u.* appear (see Bachmann *et al.* (1994)). Contributing to the growth of such large ions are most probably uncharged PAH molecules with masses of ~400 *a.m.u.* (see Hall-Roberts *et al.* (2000)). Inevitably a positive ion of mass ~2000 *a.m.u.* is overheated, because it has acquired the exothermicity of growth reactions and also of coagulation. This large "hot" ion can dissociate to give a small positive ion (possibly $C_3H_3^+$ or the positive ion of a tiny PAH^+). Alternatively, reaction of the large hot ion (~2000 *a.m.u.*) with a small, but neutral PAH can also produce a small PAH ion and thereby remove excess energy from the hot ion. In both these ways, the large hot ions produce tiny ions, which again experience growth up to a mass of ~2000 *a.m.u.*

3. Experimental

The aims of the present investigation are to assess the dependence of the soot formation on important parameters that determine the mixing field (exit velocity and frequency of precession) and thereby assess the relationship between flame strain and soot formation and its role in radiant heat transfer. The experimental equipment and procedures used in the present study are described first. The experimental operating procedures, issues of safety and personal protection requirements are also described concisely.

3.1. Experimental System

A light sheet was formed by focusing the laser beam through a long-focal-length (1 *m*) spherical lens and then diverging the focusing beam in one dimension with a cylindrical lens. The resulting sheet of laser light was directed through the flame. Light, scattered by the soot particles, was collected by an ICCD camera orientated at right angles to the laser sheet. The collected images were processed to provide a concentration map of soot particles in the flame. Use of a sufficiently short pulse of the illuminating sheet (5.4 *ns*) froze the turbulent motion in each image[1]. The instantaneous images, in digitised format, were further processed to provide a range of data.

---

[1] The calculated maximum jet exit velocity, U_0 was 37.08 ms^{-1} (this corresponds to a maximum value of the *Re* number of 11223). Since the duration of the laser output pulse was 5.4 *ns* (see Quantel BrilliantB Instruction Manual (1996)), the relocation of any point of the stream from the beginning until the end of a single image collection, could not exceed 0.2 μm. Thus, the deformation of the images is negligible.

3. Experimental

A schematic diagram of the general arrangement of experimental apparatus is shown in Figure 3-1. The major items of equipment and their performance characteristics follow.

A) Laser

To obtain a relatively strong Mie scattering signal a Q-switched, pulsed Nd:YAG laser model "Brilliant BW" irradiated the flame. The fundamental wavelength of the laser, 1064 *nm*, was frequency doubled to 532 *nm*, which is in the visible green region of the spectrum. The laser has a maximum energy per pulse of 385 *mJ*, a 10 *Hz* repetition rate, and a pulse duration of 5.4 *ns*. To avoid the generation of laser induced incandescence of the soot particles, the actual energy of the output pulse was maintained at 1.30 *mJ*.

The laser provides three modes of operation: manual, automatic and external. The first mode is mainly used to check ① the normal operation of the power supply and of the flashlamps. Laser emission should not be obtained under this mode. ② In the automatic (internal) synchronisation mode, the "fire" command is generated automatically at a rate determined by an internal clock. The timing diagram of this mode is shown in Figure 3.2. ③ The external mode was used in the current work because it allows the laser emission to be synchronised with the experimental system. The accuracy of this mode varies from a few *ns* to about 10 μs. For Q-Switch synchronisation a signal must be set with delay following the external firing in the order of 275 to 330 μs if the maximum output energy is to be obtained. The delay was adjusted to 380 μs here to obtain the required output energy of 1.30 *mJ*. A full description of the laser and operational instructions can be found in Quantel BrilliantB Instruction Manual (1996).

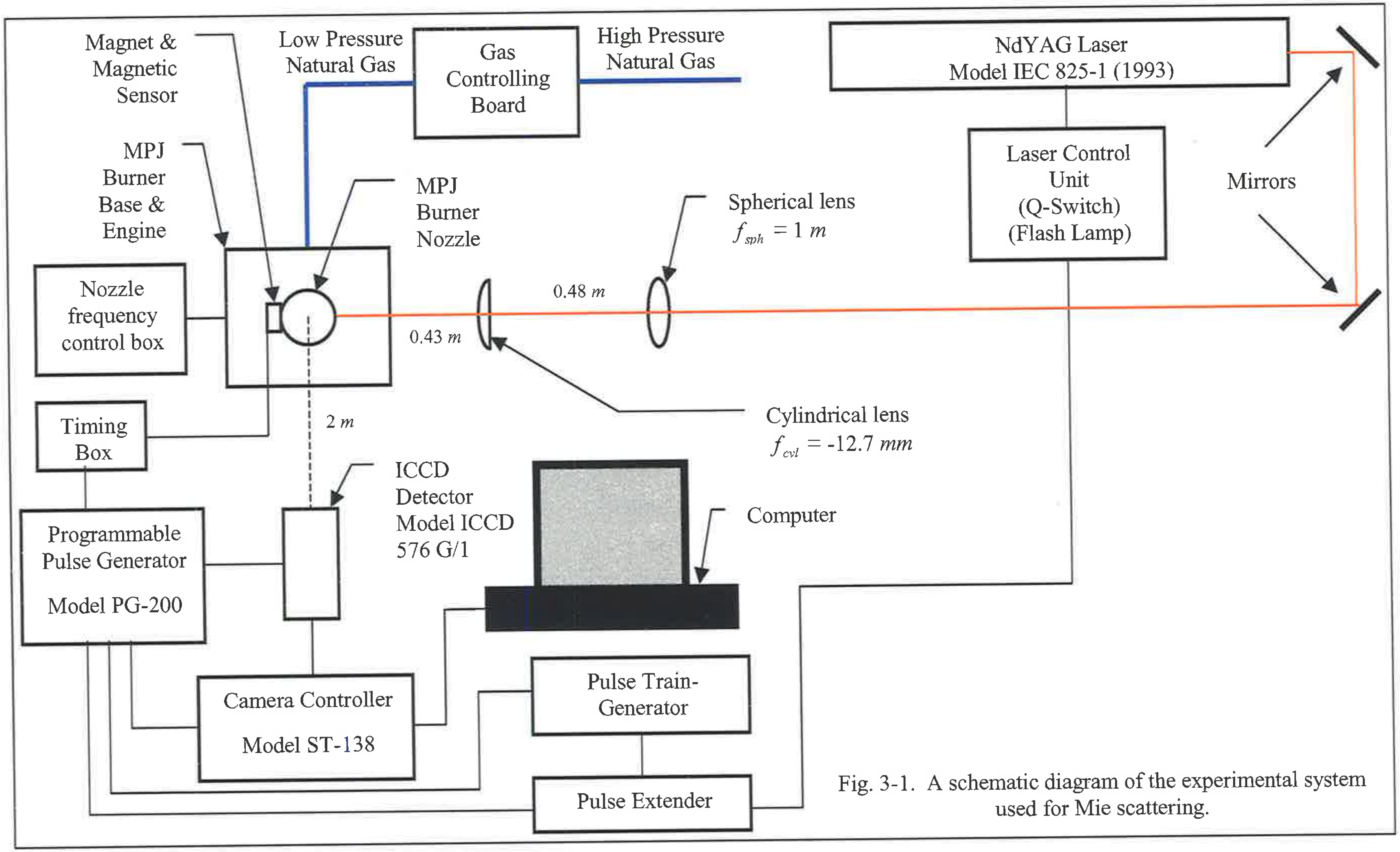

Fig. 3-1. A schematic diagram of the experimental system used for Mie scattering.

The burn pattern of the laser beam at 532 *nm* wavelength and a distance of 30 *cm* from the optical head of the laser, and the far field pattern at 1064 *nm* are shown in Figure 3-3. The average radius of the burn pattern, r_{burn} is ~0.4 *cm*. The properties of the beam are summarised in Table 3-1.

Table 3-1. Properties of the laser beam, after Quantel BrilliantB Instruction Manual (1996).

Elliptical rotation	-21 degrees
Elliptical roundness	0.650
Gaussian major centroid	3.439×10^3 μm
Gaussian minor centroid	3.038×10^3 μm
Divergence major	5.747×10^{-1} *mrad*
Divergence minor	3.735×10^{-1} *mrad*

B) Optical Arrangement

The optical system (Fig. 3-1) included two flat beam steering mirrors aligned at 45°, a spherical lens with a focal length, f_{sph}, of 1 *m* and a cylindrical lens with a focal length, f_{cyl}, of -12.7 *mm*, all situated on adjustable optical mounts. The distance between the cylindrical lens and spherical lens, s', was 0.48 *m*. The distance between the axis of rotation of the nozzle and the cylindrical lens, s'', was 0.43 *m*. The mirrors were coated to maximise reflection of the 532 *nm* beam. The optics transformed the cylindrical pulse into a light sheet by focusing the beam through a spherical lens and diverging the beam in one dimension through a cylindrical lens. For safety reasons the laser beam path was surrounded by non-transparent shields and a beam stop absorbed the transmitted light.

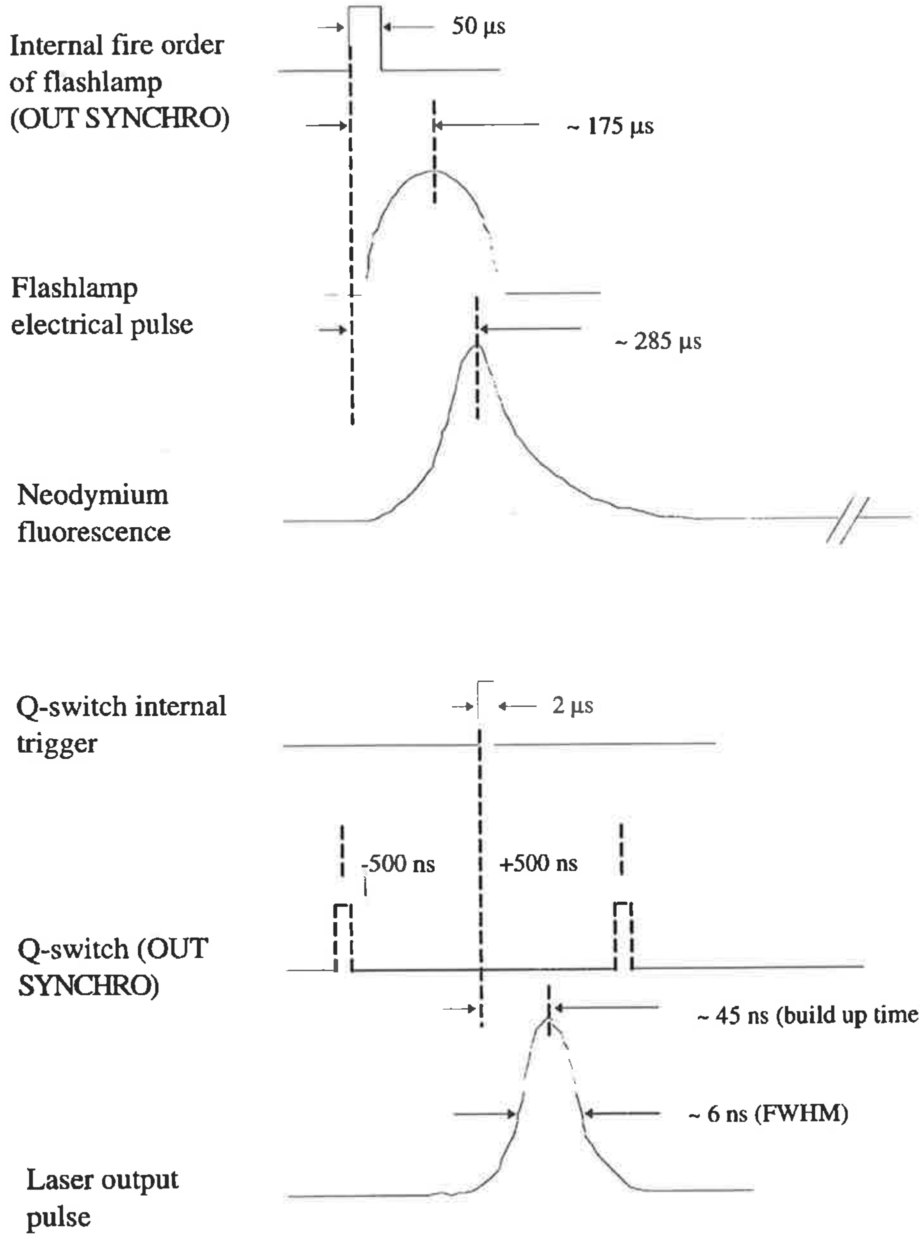

Fig. 3-2. Timing diagram of the automatic (internal) synchronisation laser mode, after Quantel BrilliantB Instruction Manual (1996).

意思就是 FL-点火 285us之后 Q-switch 出 laser

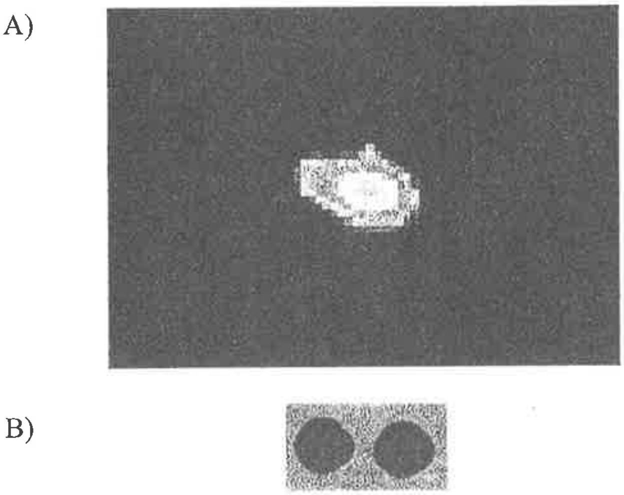

Fig. 3-3:

A) The far field pattern of the laser beam at 1064 *nm* wavelength;
B) The burn pattern of the laser beam at 532 *nm* wavelength and a distance of 30 *cm* from the optical head of the laser. The average radius of the burn pattern, r_{burn} is ~0.4 *cm*.
The patterns are taken from Quantel BrilliantB Instruction Manual (1996).

C) MPJ Burner

The mechanical precessing jet is based on mechanical rotation of an inclined simple jet around the burner axis. It allows independent control of the dominant parameters that determine the jet behaviour: jet exit angle, ϕ, nozzle diameter, d_n, frequency of rotation, f_p, and jet exit velocity, U_0 via the characteristic Reynolds, $Re = d_n U_0 \rho / \mu$, and Strouhal, $St = f_p d_n / U_0$, numbers. Here ρ is the density and μ the dynamic viscosity of the fuel jet. The nozzle diameter, was fixed at 5 *mm*, the nozzle deflection angle at 45°, and the frequency of precession varied from 0 to 75 *Hz* in the current experimental set. A schematic representation of the MPJ nozzle is given in Figure 3-4.

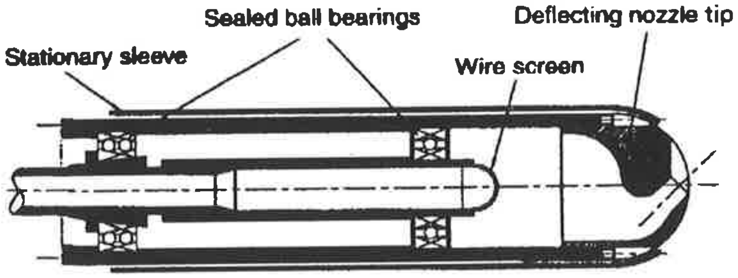

Fig. 3-4. A schematic diagram of the mechanically rotated precessing jet nozzle (MPJ), after Nobes *et al.* (1996).

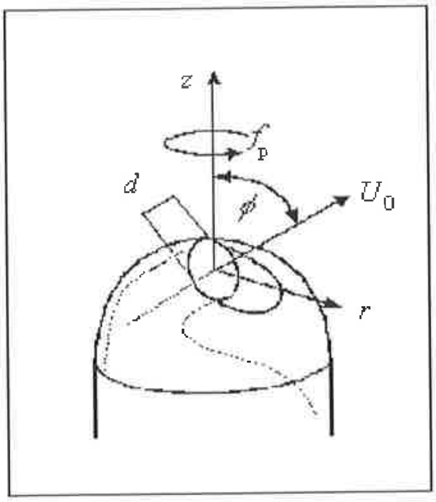

Fig. 3-5. The MPJ coordinate system, after Schneider *et al.* (1997). The nozzle rotates around the nozzle axis, z at a frequency of precession, f_p.

The MPJ coordinate system is shown in Figure 3-5. The nozzle rotates around the nozzle axis, z.

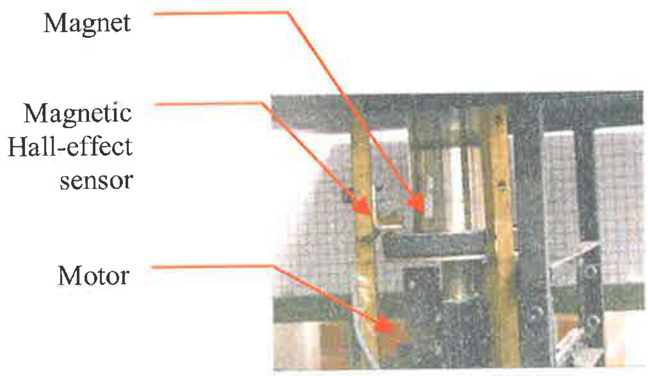

Fig. 3-6. Base of MPJ nozzle.

D) MPJ Burner Base & Motor

The base of the MPJ burner supports the burner, the electrical motor, (ABB 3 Phase CI.Fll IEC34 MT80A19-4 Mk110018-L), a magnet that was located on the axle of the burner and a magnetic Hall-effect sensor. The axle of the MPJ burner was connected to the electrical motor through a transmission. Angular frequency of the motor was controlled by a frequency control unit, Model ABB ACS 2, which allows the nozzle rotational frequency to be set between zero and 100 *Hz*, maintained within 0.01 *Hz*. The burner was balanced to reduce vibrations that occur at high frequencies. This included using a spirit level to ensure the adjustable table was level, and by clamping lead weights to the burner table. The burner was fired upward underneath a $1m \times 1m$ exhaust hood. A schematic diagram of the MPJ burner base and motor is given in Figure 3-6.

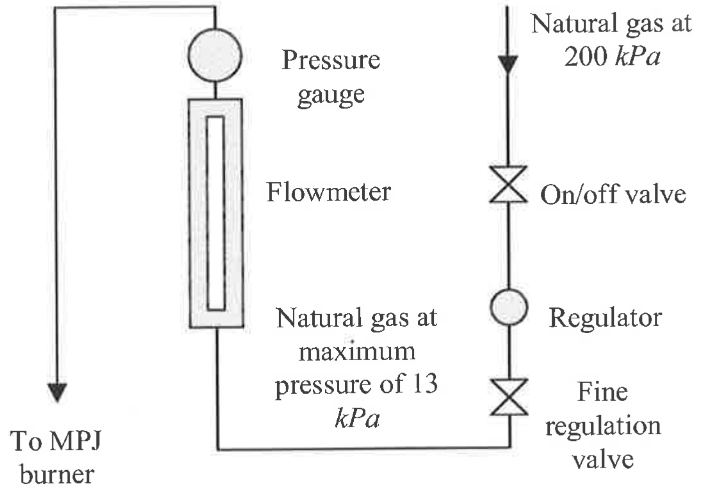

Fig. 3.7. Schematic diagram of gas controlling board.

E) Gas Controlling Board

The fuel used in the experiments was natural gas. The *Re* number was varied from 4329 to 11223, corresponding to inlet pressure of the gas from 2 to 13 *kPa*. The functions of the gas controlling box were firstly, to reduce the pressure of the delivered natural gas from 200 *kPa* to the required pressure, and secondly, to regulate the gas flow rate. The gas controlling board comprised an on/of valve, a regulator, a fine regulation valve, a ABB F&P VA flowmeter (model 10A3500, P/No 10A3565ADT60A), and a pressure gauge. The tube of the flowmeter was FP-1/2-17-G-10/83, P/No 448B557VO1, the float was STD Float ½-GUSVT-413, P/No 603B520T60. A schematic diagram of the board is shown in Figure 3-7.

F) Magnetic Sensor and Timing Box

A magnetic Hall-effect sensor was mounted to the rotating base of the MPJ burner to generate a triggering pulse with each rotation, thus the number of signals was equal to the frequency of rotation of the burner, f_p. The timing box reduced f_p signals per second to one 10 μs signal per second. This signal triggered the laser and the camera at a constant phase of the nozzle relative to the laser beam.

G) Programmable Pulse Generator and Pulse Extender

The programmable pulse generator model PG-200 received the signals from the timing box and generated time delayed signals to the laser flash lamp, Q-switch and ICCD detector. Full details about the pulse generator can be found in the Operation Manual (1997). The delay time was 10 μs to the laser flash lamp, 390 μs to the laser Q-switch, and 394.17 μs to the ICCD detector. The function of the pulse extender was to extend the duration of the 10 μs signal from the timing box to that required by the laser flash lamp and Q-switch triggering signal of 25 μs.

H) ICCD Detector and Camera Controller

The light sheet interacts with the flow field and the resulting signal (scattered light), from the image window is captured by an image intensified (ICCD) detector, Model ICCD 576 G/1. The operating parameters of the detector are listed in Table 3-2. Full details can be found in ICCD Detector Operation Manual, Version 3.B, P/N 4411-0009, Princeton Instruments Inc., Trenton, NJ, USA.

The plane of the incident laser light was aligned to be perpendicular to the viewing window of the detector. [The gate width of the detector was 20 ns. This small gate width prevented interference from the flame luminosity and allowed detection of the relatively strong Mie scattering signal.]

Table 3-2. Operating parameters of the ICCD 576 G/1 detector, after Operation Manual, Princeton Instruments Inc.

CCD Arrays	EEV 576 x 384 full frame or frame transfer, 22.5×22.5 μm pixels
Image Intensifier	18 *mm*
Method of Coupling	1:1 fiber optics
Spatial Resolution	85 μm spot size FWHM
Geometric Distortion	< 1 pixel
Sensitivity	Variable gain adjustment allows sensitivities from 1-70 counts per photoelectron
Gating Speed	Fast Gate Intensifier, 2-7 *ns* FWHM; Slow Gate Intensifier, 50-70 *ns* FWHM
Gating ON/OFF Ratio	5×10^6:1
Response Linearity	Better than 1% for the upper 95% of range in Shutter mode. Slightly non-linear response at lower 5% of range, due to phosphor nonlinearity
Photocathode Dark Charge (EBI)	Red-blue enhanced, < 5 counts/pixel-second; Red-enhanced, < 15 counts/pixel-second
Phosphor Decay	2 *ms* standard, 300 *ns* phosphor is optional
Spectral Range	Red-blue enhanced, 180-800 *nm*; Red enhanced, 360-920 *nm*
Nonuniformity	Typically 12%
Noise	1-1.5 counts in Gate mode
Water Flow	1-3 liters per minute for maximum cooling
Nitrogen Gas	1-2 liters per minute initially, 750-1000 ml per minute during experiment

The camera controller, model ST-138, transformed the analogue signals from the ICCD detector to the digital signals required by the computer video card. Full details of the controller can be found in ST-138 Controller Operational Manual, Version 3, Revision E, Princeton Instruments Inc., Trenton, NJ, USA, 1998.

[I) Data Visualising and Analysing Equipment

A computer, whose video card was connected to the camera controller was used to collect the signals. The images were analysed using Spyglass "Transform" software, Version 3.0 (see Spyglass Transform Quick Tour and Reference (1993)), which converted the images into matrices with a certain number of columns and rows. Every image had 576 × 384 pixels corresponding to a fixed spatial location since the burner, the camera and the optics were not] moved. The data were stored in 8 bit digital format, which means that the value stored in every pixel could vary from 0 to maximum 256 depending on the intensity of the received signal. The data were used in the further statistical calculations.

3.2. Experimental Operating Procedure

The start-up and shut-down procedures of the laser are given in Chapter IV of the Quantel BrilliantB Instruction Manual (1996). An integrated timing diagram is shown in Figure 3-8. Details can be found in the previous section.

Note that a target was positioned on the axis directly above the nozzle prior to the commencement of the experiments. It was used to (i) determine and optimise the field of view of the ICCD detector, (ii) focus the camera, and (iii) it was used as a reference for the spatial resolution of the experiment.

3.2.1. Flame Ignition and Extinction Procedure

The flame ignition and extinction procedure included a sequence of the following steps:

1. Ensure suction fan of exhaust duct is on.
2. Check that fuel on/off valve is closed.
3. Open valve on bottle and set operating pressure using regulator.
4. Open fuel on/off valve.

5. Select suitable low gas flow rate for ignition.
6. Ignite the natural gas.
7. Collect data.
8. Reduce the flow rate to minimum.
9. Turn off the fuel on/off valve.
10. Turn off the valve at the gas cylinder.

3.2.2. Data Collection

1. The MPJ Burner was positioned under the extraction hood with the light sheet passing through the geometric axis of the nozzle. The field of view and the focus of the ICCD were optimised using the target. The size of the instantaneous Mie scattering image area was fixed at 16 *cm* height and 23 *cm* width. The image area was smaller than the flame, so the images were only from a fixed part of the flame, beginning from about 10 *cm* above the nozzle.
2. About 20 images of the light sheet were collected. An average of these was later used in the data correction process. Note that the position of the light sheet and the quality of the light sheet did not vary significantly from experiment to experiment. Also, the camera was not moved until after the end of the set of experiments. This ensured that the field of view of each pixel remains constant.
3. About 20 images of the background with the laser off and the same number of images of the background with the laser on were collected. These data were used in the subtraction of the background subradiation (noise).

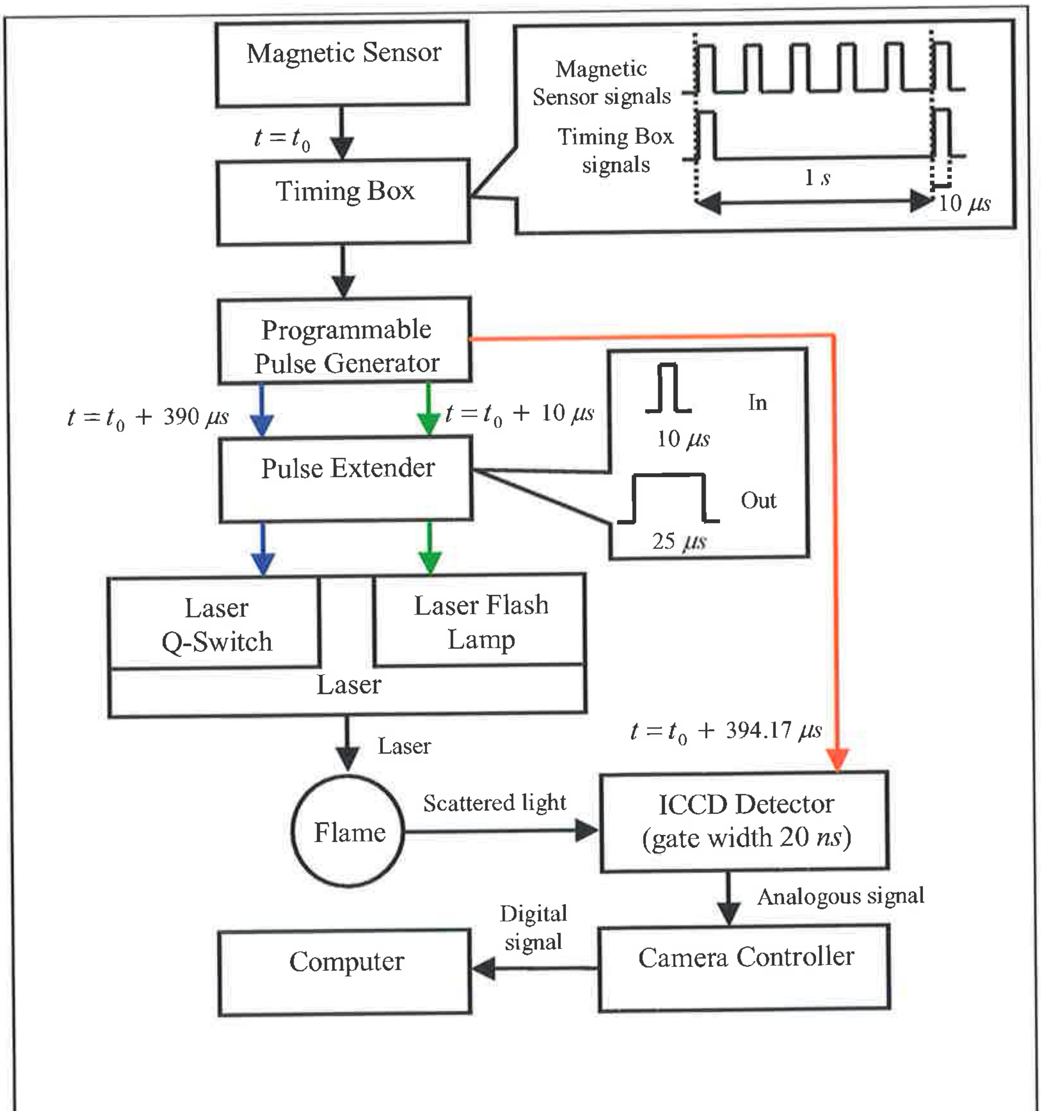

Fig. 3-8. Integrated timing diagram of the experimental system.

4. The fluid flow rate through the nozzle was set and the flame was ignited.
5. A series of images was collected. The number of images varies depending on the type and requirements of the experiment. Between 100-300 images were collected for each experimental condition.
6. Images were downloaded to the computer.

7. The experimental conditions were then changed ready for the next experiment.

3.2.3. Dominant Sources of Error

In general, there are three dominant sources of error that are associated with the Mie scattering technique. These are marker (or particle) inertia[1], marker shot noise[2]. and optical attenuation.

The absorption and scattering of the laser beam by particles along the optical path is a source of error. This occurs both as the laser sheet enters the control volume and as the scattered signal travels towards the detector. For a given path length the beam intensity decreases exponentially with the number of particles in the path. When this number fluctuates in time, a complex modulation is added to the scattered light field and reaches the detector as noise. Attenuation noise can be minimised by optimising the available laser power to produce a signal of appropriately high intensity and, for the cases where this is possible, by minimising the particle concentration to that just necessary to achieve acceptable results.

---

[1] The inertial characteristics of the particles used to mark the fluid determine how well the marker follows the flow. Becker *et al.* (1969a) analysed this problem and calculated the frequencies at which the velocity amplitude response is within a set value can be predicted, however providing further details is beyond the scope of this work.

[2] Concentration measurement using the Mie scattering technique is based on the "counting" of the number of particles in a control volume. It is this number which is assumed to be proportional to the concentration of the marked fluid. When the size of the control volume is large and the seeded density of the marker is high the fluctuation of the number of particles used to represent a given concentration of marked fluid will vary only minimally compared to the total number of particles. As the size of the control volume or the density of the seeded particles decreases, the fluctuation, as a proportion of the total number, becomes significant. This variation in the number of particles introduces an error in the estimate of the concentration of the marked fluid and is termed, marker shot noise. Providing further details is beyond the scope of this work.

Other sources of error, which have been addressed in the literature by others, relate mainly to the influence of specific items of equipment used by those investigators.

3.3. Data Correction

3.3.1. Correction for Variations in the Spatial Intensity

There are two important corrections to the data that must be applied. The first correction is for variations in the spatial intensity of the light sheet. Ideally, a pulsed laser produces a cylinder of light of constant intensity. In reality, the intensity distribution in the cross-section of the laser beam is not uniform but usually approximates a Gaussian function

$$I = I_0 e^{\frac{r_b^2}{r_G^2}} \qquad (1)$$

where I_0 is the axial value of the intensity, r_b is the radial distance from axis and r_G is the Gaussian beam radius. The commonly adopted definition for r_G is that it is equal to the diameter at which the beam irradiance (intensity) has fallen to $1/e^2$ (13.5%) of its peak, or axial value.

The intensity of the beam, which is aligned horizontally, varies radially. It is the variations in the vertical direction which are of concern here, because when the beam is expanded through

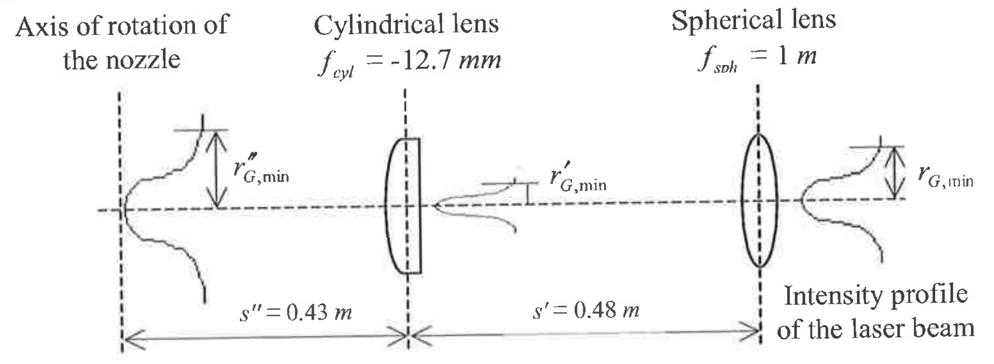

Fig. 3-9. A schematic to the optical system.

the cylindrical lens in one dimension the radial variation will produce a variation of the beam intensity profile across the long axis of the light sheet. A correction for consistent variations in the light sheet can be obtained experimentally by a calibration of the light sheet using, for instance, a planar laser induced florescence technique (the "Fish Tank" method[1]), or numerically. The availability of statistical data about the properties of the laser beam that is used in the current work (see Table 3-2 and the Quantel BrilliantB Instruction Manual (1996)) allowed a numerical correction to be implemented[2]. Although less accurate than an experimental correction, it is sufficient for the present semi-quantitative purpose.

---

[1] The "Fish Tank" is filled with a uniform concentration of Rhodamine B, a fluorescent dye which emits orange light when excited with the green, 532 *nm* of the Nd:YAG to provide intensity maps of the light sheet. Several images are captured by the detector to produce an "average light sheet" profile. A curve is fitted to the profile and then used to generate a light sheet correction image. This correction image, a record of the consistent non-uniformities in the light sheet is used to correct each of the data records. Details about this method can be found in Nobes (1997).

[2] Note that Mie scattering cannot provide absolute measurements of soot intensity anyway.

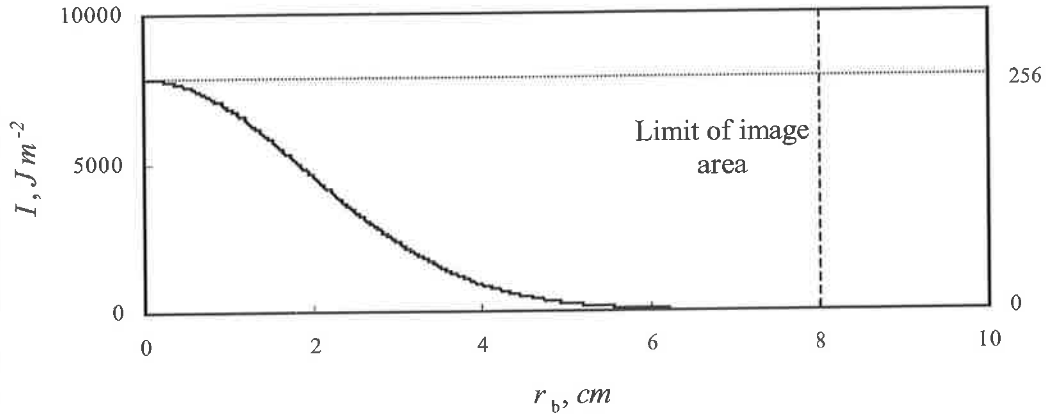

Fig. 3-10. Calculated intensity distribution along the vertical axis of the laser beam. On the right are the re-scaled values of the intensity in 8 bit digital format.

The distances s' and s'' are, respectively, 0.48 and 0.43 *m*, f_{sph} is 1 *m* and f_{cyl} is -12.7 *mm*. Hence[1] $r'_{G,\min}$ becomes -0.08 *cm* (minus indicates an inverted image), and $r''_{G,\min}$ becomes 2.72 *cm*.

Equation (1) is modified to

$$I = I_0 e^{\frac{r_b^2}{(r''_G)^2}} \tag{9}$$

where I_0 is

---

[1] Equations similar to equations (5) and (8) can used to calculate the size of the images of $r_{G,maj}$ and r_{burn}. $r'_{G,maj}$ and $r''_{G,maj}$ are -0.09 *cm*, r'_{burn} is -0.1 *cm* and r''_{burn} is 3.63 *cm*.

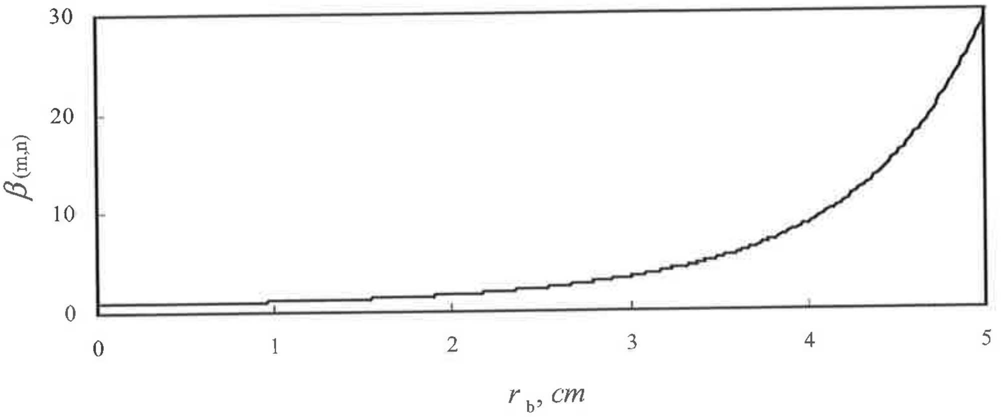

Fig. 3-11. The correction factor, $\beta_{(m,n)}$, distribution along the vertical axis of the laser beam.

$$I_0 = \frac{E_0}{S''_{pix}} \tag{10}$$

The output energy of the laser, E_0, was set on 1.30 *mJ*. The geometrical size of a single pixel from the image, S''_{pix}, can be found by division of the image area of the ICCD detector by the number of pixels per image. Remember that every image has 576 × 384 pixels (or 221184 pixels per image) and the size of the image taken by the detector is fixed at 16 *cm* width and 23 *cm* length (or 0.0368 m^2). That gives for S''_{pix} an area of 1.66×10^{-7} m^2. I_0 then becomes 7.83×10^3 $J\ m^{-2}$. The intensity distribution along the vertical axis of the beam is shown in Figure 3-10. Note that the intensity should be re-scaled so that the maximum value of I corresponding to the maximum value stored by a single cell of the matrix in 8-bit digital format is 256. The minimum value of I should correspond to 0. This re-scaling is also shown in Figure 3-10.

The correction factor that should be applied to every cell of the matrix, $\beta_{(m,n)}$, is

$$\beta_{(m,n)} = \frac{I'_0}{I'_{(m,n)}} \tag{11}$$

where $I'_{(m,n)}$ is the re-scaled value of the intensity (from 0 to 256) of a cell with coordinates (m,n) and I'_0 is the re-scaled maximum intensity (256). The correction factor distribution along the vertical axes of the beam is shown in Figure 3-11.

It is evident from Fig. 3-10 that I tends to zero as r_b reaches 6 *cm*. The required correlation factor increases exponentially with r_b (Fig. 3-11). In order to minimise the error, it is necessary to collect the data from zones where the correlation factor is kept within reasonable limits (ie. from 3 to 4). It was found that $\beta_{(m,n)}$ is about 3.4 at $r_b = 3$ *cm*. Thus, it is reasonable to collect the data for further calculation of soot intensity along the axis of the beam, from a relatively small (6 *cm* width) area of the image from the ICCD detector.

Note that the correction applied to the cells that belong to the same row remains constant. The corrected value of the signal from a cell with coordinates (m,n), $x_{corr,(m,n)}$ becomes[1]

---

[1] The matrix $\left\| x'_{corr,(m,n)} \right\|$ is $\begin{Vmatrix} x'_{corr,(1,1)} & \cdots & x'_{corr,(1,n)} \\ \vdots & & \vdots \\ x'_{corr,(m,1)} & \cdots & x'_{corr,(m,n)} \end{Vmatrix} = \begin{Vmatrix} \beta_{(1)} \\ \vdots \\ \beta_{(m)} \end{Vmatrix} \times \begin{Vmatrix} x_{image,(1,1)} & \cdots & x_{image,(1,n)} \\ \vdots & & \vdots \\ x_{image,(m,1)} & \cdots & x_{image,(m,n)} \end{Vmatrix}$

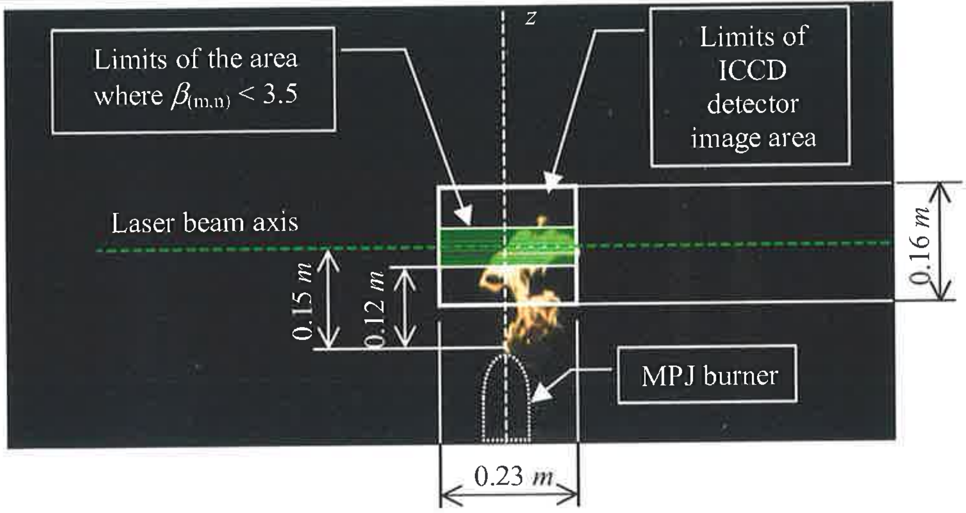

Fig. 3-12. Size and location of object area captured by the ICCD detector, compared with the size and location of the area where $\beta_{(m,n)} < 3.5$.

$$x'_{corr,(m,n)} = \beta_{(m,n)} x_{image,(m,n)} \tag{12}$$

where $x_{image,(m,n)}$ is the signal from the cell with coordinates (m,n) as it is received by the ICCD detector.

The size and location of image area captured by the ICCD detector is compared with the size and location of the area where the correlation factor, $\beta_{(m,n)}$, is kept reasonably low, < 3.5, in Figure 3-12. The distance between the axis of the laser beam and the top of the MPJ burner was 0.15 *m*.

3.3.2. Correction for Pulse-to-Pulse Intensity Variations

A second correction is required to allow an ensemble average of the images to be carried out. The signal in a given individual image is a function of the laser power in the pulse used to generate that image. If the power of the laser pulse varies between pulses, then each image must be corrected for this pulse-to-pulse power variation.

About 20 images of the background with the laser off and the same number of background images with the laser on (using internal triggering) were collected. The subradiation (noise) results from the natural emission of the background at ambient temperature of ~294 *K*, and the laser light reflected by the equipment. Both factors were found to have a negligible effect, because of the relatively low temperature of the background, and also because the experimental area was coated with a black, light absorbing material. Periodical monitoring of output energy showed that the pulse-to-pulse variations of the laser beam could be excluded from further considerations since its intensity and consequently, the intensity of the subradiation (noise), varied slightly (<1 %) from pulse-to-pulse.

3.3.3. Correction for Non-optical Disturbance

It was found that the work of the electric motor used to rotate the burner generates an intensive electro-magnetic field that is detectable by the ICCD camera and leads to the appearance of an additional noise in the form of chaotic white speckles in the images.

The identified hazards was dealt with as follows:

1. The laboratory ventilation system was always turned on.
2. Fuel lines were checked prior to each experiment to ensure that they were not disconnected by a previous operator.
3. The methane bottle fitting, fuel lines and all devices were regularly checked for leaks.
4. The pressure of any device or tube in the fuel line was controlled to not exceed the safe operating levels of 200 *kPa.*
5. Experiments were performed with at least two people present.
6. During operation, a safe distance from the flame was maintained by personnel.
7. Laser safety glasses with side shields and designed to absorb specific wavelengths while allowing a reasonably high level of visible light were worn at all times.
8. The laser beam was terminated by the beam stop.
9. The laser beam was kept below eye level and isolated by special safety screens.

4. Results and Discussion

A range of conditionally sampled experiments was carried out at various combinations of *Re* and *St* numbers from 4329 and 0.0042 to 11223 and 0.0245, respectively. The nozzle diameter was fixed at 5 *mm* and the jet exit angle at 45 degrees. The phase of the jet precession was the same in each image, with the jet emerging in the plane of the light sheet. The vertical distance of the bottom of the images above the jet exit was 14 *d* and the axis of rotation corresponded to the middle of the image. The semi-quantitative measurements of soot intensity are presented. The soot intensity correlation with flame strain is discussed.

4.1. Semi-Quantitative Measurements of Soot Intensity

The calculated relative soot intensity assumes proportionality between the intensity of the scattered signal and the number of soot particles in the flame envelope. It is important to note that the data presented in this section are semi-quantitative since the Mie scattering signal depends on both particle size and number density and the calibration of the signal intensity is not absolute[1]. Nevertheless the data provide important trends of relative amounts of soot formed under different experimental conditions.

---

[1] The Mie scattering technique cannot provide absolute soot volume fraction, since the signal depends on particle size, the wavelength of incident radiation, the refractive index of the particle and the angle made with respect to the incident beam. According to the Mie theory, the light intensity is higher for larger spheres at the same scattering angle. This implies that large particles can be distinguished from small particles by the strength of light reflected off their surfaces at the same angle.

Between 100 and 300 images were collected for each experimental condition. Selected typical images are shown in Appendices from A-1 to A-71. A summary of the experimental conditions and the contents of the appendices are given in Table A.

The average signal per pixel, χ, was calculated from about 50 images on average for each experimental condition, as

$$\chi = \frac{\sum_{i=1}^{i=m_{Mie}\times n_{Mie}} x_{i,corr}}{m_{Mie}\times n_{Mie}} \tag{16}$$

where m_{Mie} and n_{Mie} are the number of columns and rows corresponding to the instantaneous Mie scattering image matrix, $\left\| x_{corr,(m,n)} \right\|$, and $x_{i,corr}$ is the level of signal intensity for individual cells[1]. The results are summarised in Tables 4-1 and 4-2, where the interpolated or extrapolated values are marked with an asterisk, and in Figures 4-1 and 4-2. The surface plot shown in Figure 4-3 demonstrates the dependence of the average signal per pixel, χ, on *Re* and *St* numbers. It reveals that the relative soot intensity increases with increase in both *Re* and *St* numbers, however, the latter is more influential.

The level of signal intensity for individual cells from the instantaneous Mie scattering image matrix, $x_{i,corr}$ can vary from 0 to 256 in 8-bit digital format. Histograms were used to bin the

---

[1] The data correction procedure is given in Chapter 3. Note that the applied mathematical correction is not able to account for the all of the issues related to the actual non-uniformities in the beam profile. Nevertheless it accounts for the major distortion and is therefore reasonable given the inherent limitations in the technique. It allows semi-quantitative information, i.e. useful trends.

cells into 5 equally spaced groups and to return the number of cells in each group. The first group contained the number of cells with a very low level of signal intensity (from 1 to 51), then follow the group with a low level of signal intensity (from 52 to 102), the medium (103-153), the high (154-204) and the very high (205-256) groups.

Table 4-1. Average signal, χ, from the instantaneous Mie scattering images. Constant *Re*, various *St* numbers.

Re	*St*							
	0.0056	0.0061	0.0069	0.0083	0.0091	0.0106	0.0116	0.0139
4329	0.24	1.30	2.24	4.14	4.72	7.62	5.38	21.69
5437	1.17	1.58	3.54*	3.40	6.38	3.53	4.39	13.93
6555	1.67	2.68	7.90	3.39	5.41	4.31	10.35	25.21
7682	1.50	1.98	2.56	3.60	4.50	11.92	10.91	49.36
8840	1.27	2.02	2.59	4.73	12.30	6.67	35.26	46.43*
10012	1.05	3.62	5.90*	5.82	10.87	26.74	29.12*	52.17*
11223	1.89	6.54	8.28	9.85	14.21	18.75*	33.13*	57.43*

Since the total number of cells, $m_{Mie} \times n_{Mie}$ and the geometrical size of a single pixel from the image, S''_{pix} are known[1], the aforementioned separation of the cells into several groups can be used to estimate the proportion of the total area, *K* (%) that contains soot of equal intensity. The results for various *Re* and *St* numbers are summarised in Table 4-3 and Figure 4-4. It is evident that the tendency of the relative soot intensity to increase with increases in both *Re* and *St* numbers remains. For instance, at *Re* = 6555 and St varying from 0.0061 to 0.0162, the proportion of the total image area with a very low soot intensity increases from 1.07 to 13.79 %, that with a low soot intensity increases from 0.17 to 1.79%, that with a medium intensity from 0.06 to 0.20%, and those with a high and very high intensity increase from 0.14

---

[1] See Chapter 3.

to 1.86% and from 0.11 to 1.13%, respectively. The greatest is the increase of the very low soot intensity with an increase of the *St* number (typically more than 10 times). This phenomenon is discussed later in this chapter.

Table 4-2. Average signal, χ, from the instantaneous Mie scattering images. Constant *St*, various *Re* numbers.

Re	*Re*						
	4329	5437	6555	7682	8840	10012	11223
0.0042	-	-	0.60	-	-	-	-
0.0044	-	-	-	0.54	-	-	-
0.0046	-	-	0.58	-	0.48	-	-
0.0048	-	-	-	0.66	-	-	-
0.0049	-	-	-	-	-	-	1.27
0.005	-	0.81	-	-	-	-	-
0.0052	-	-	1.34	-	-	-	-
0.0053	-	-	-	1.09	-	-	-
0.0056	0.24	1.17	1.67	1.50	1.27	1.05	1.89
0.0059	-	-	-	0.37	-	-	-
0.0061	1.30	1.58	2.68	1.98	2.02	3.62	6.54
0.0069	2.24	-	7.90	2.56	2.59	-	8.28
0.0077	-	-	-	-	3.42	-	-
0.0079	-	-	-	2.72	-	-	-
0.0083	4.14	3.40	3.45	3.60	4.73	5.82	9.85
0.0091	4.72	6.70	5.41	4.50	12.30	10.87	14.21
0.0094	-	-	-	-	-	-	22.20
0.0099	-	-	-	4.04	-	-	-
0.0106	7.62	3.53	4.31	11.92	6.67	26.74	-
0.0113	-	-	-	-	20.70	-	-
0.0116	5.38	4.39	10.35	10.91	35.26	-	-
0.0127	6.60	-	-	-	-	-	-
0.0139	21.69	13.93	25.21	49.36	-	-	-
0.0162	-	-	60.37	-	-		-
0.0167	-	22.51	-	-	-	-	-
0.0175	30.74	-	-	-	-	-	-
0.0195	-	49.33	-	-	-	-	-
0.021	24.66	-	-	-	-	-	-
0.0245	53.25	-	-	-	--	-	-

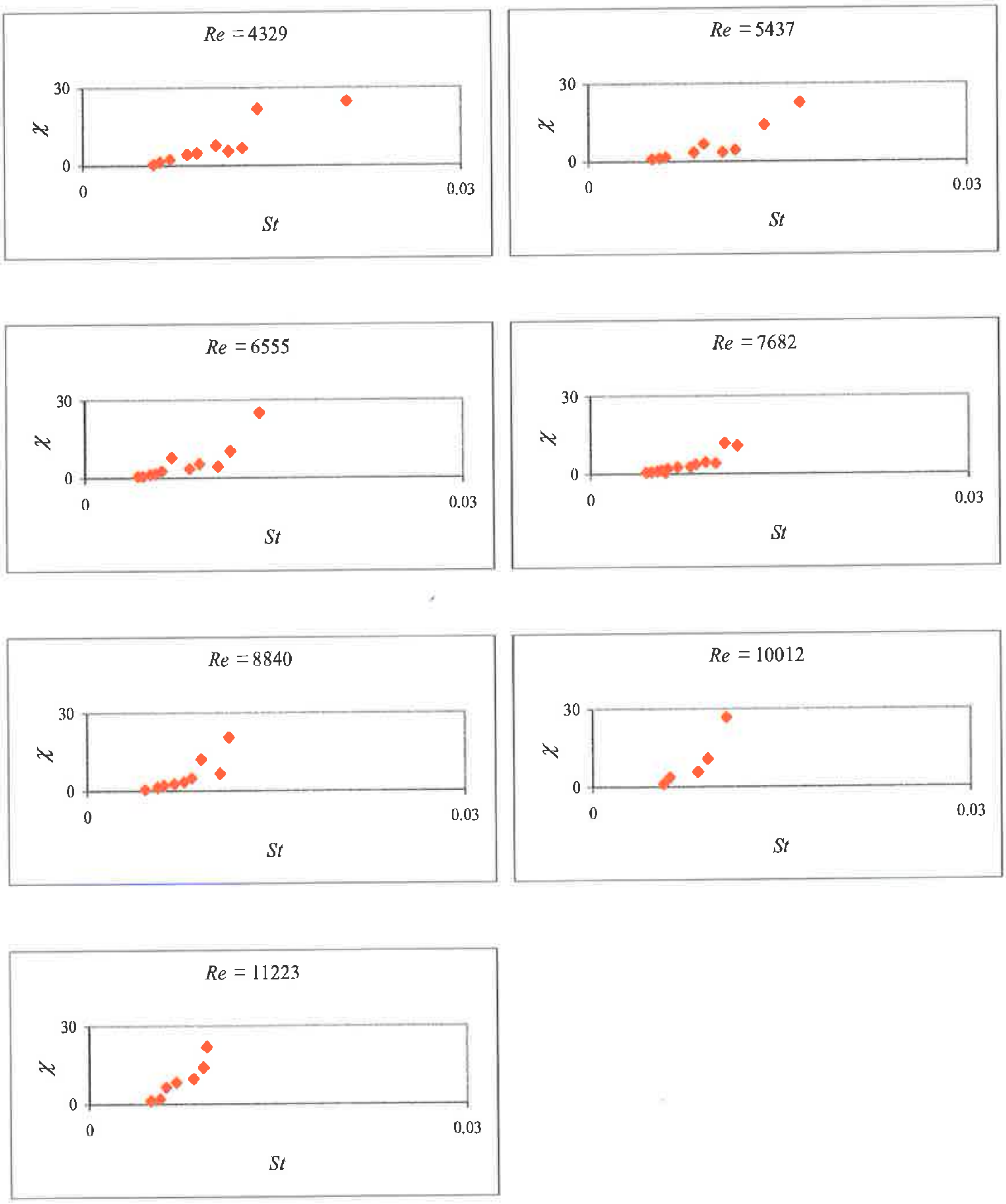

Fig. 4-1. Average signal, χ, from the instantaneous Mie scattering images per pixel in 8-bit digital format (min 0, max 256). Constant *Re*, various *St* numbers.

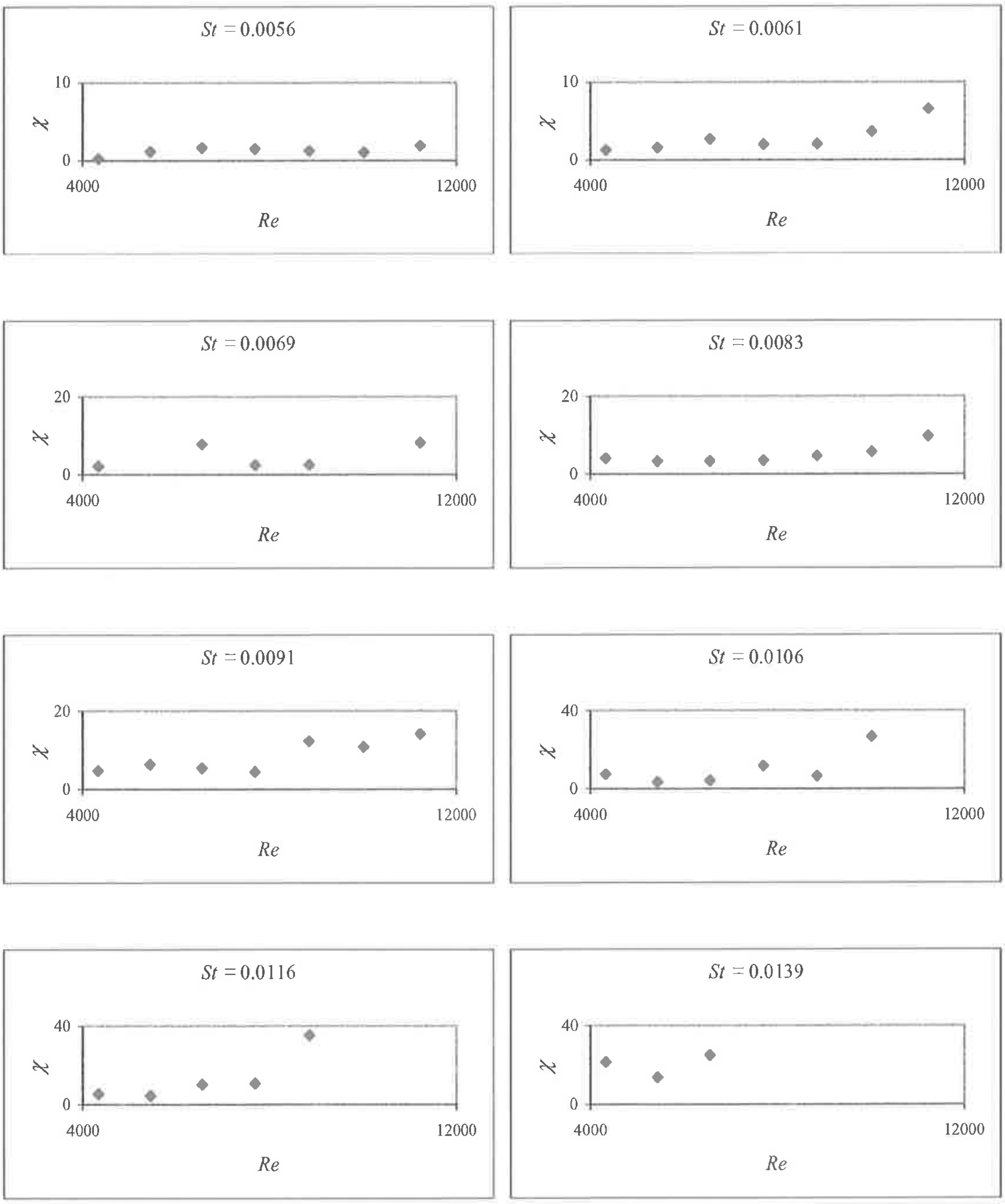

Fig. 4-2. Average signal, χ, from the instantaneous Mie scattering images per pixel in 8-bit digital format (min 0, max 256). Constant *St*, various *Re* numbers.

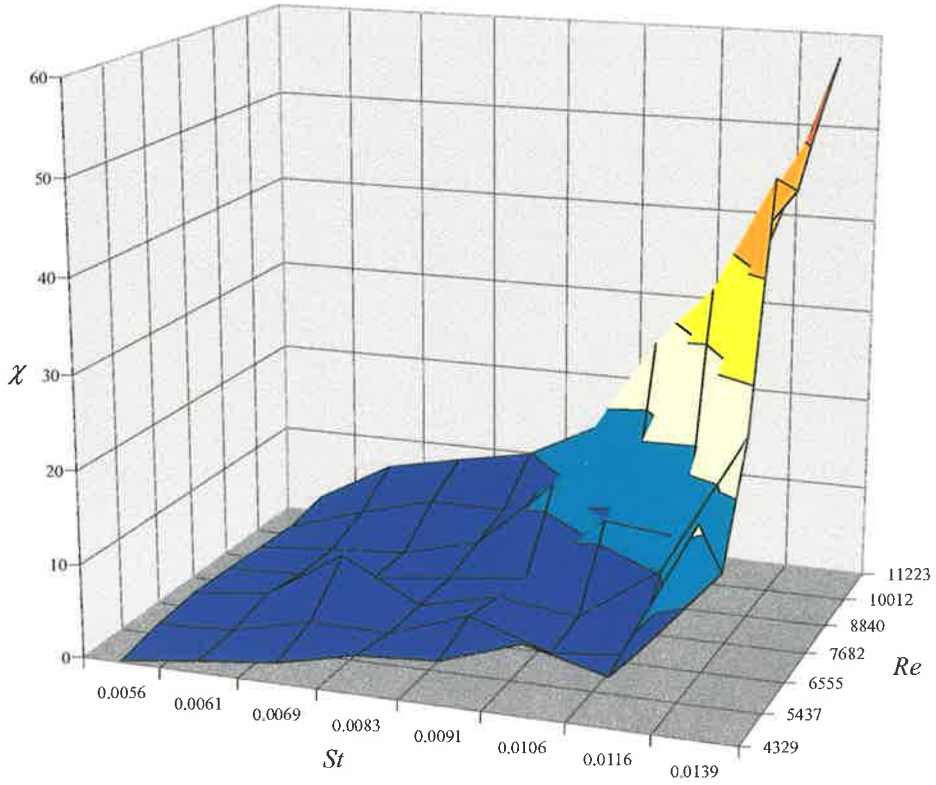

Fig. 4-3. Dependence of the average signal, χ, from the visual images per pixel in 8-bit digital format (min 0, max 256) on *Re* and *St* numbers.

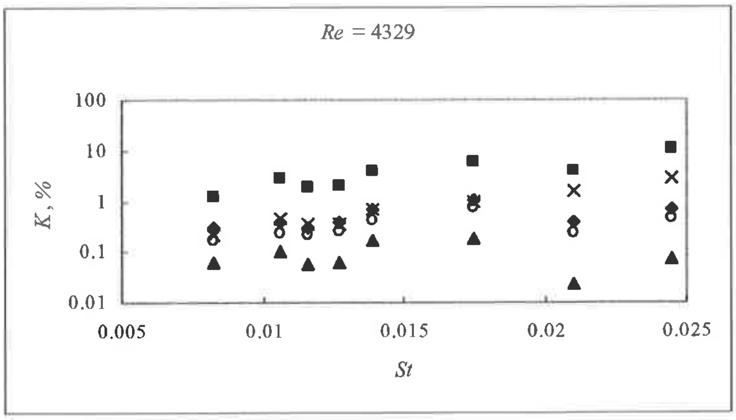
Re = 4329
100
10
1
0.1
0.01
K, %
0.005
0.01
0.015
0.02
0.025
St

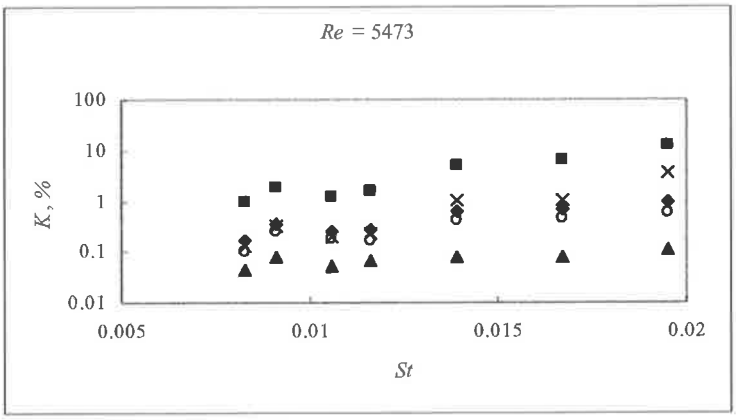
Re = 5473
100
10
1
0.1
0.01
K, %
0.005
0.01
0.015
0.02
St

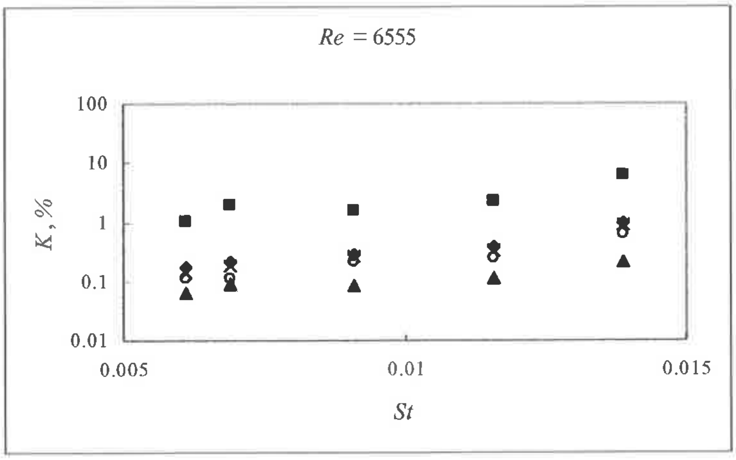
Re = 6555
100
10
1
0.1
0.01
K, %
0.005
0.01
0.015
St

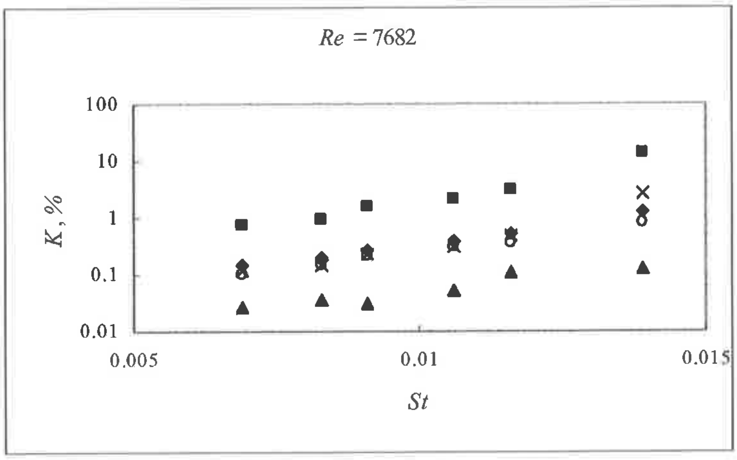

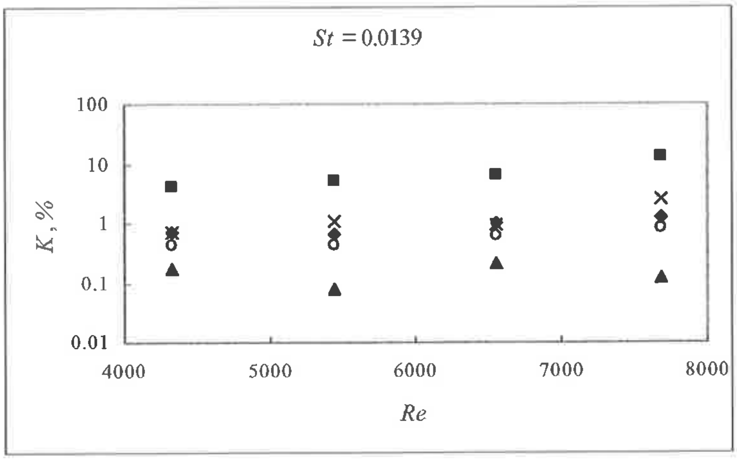

Fig. 4-4. Dependence of the proportion of the total area, *K* (%), that contains soot with equal intensity, on *Re* and *St* numbers.

Levels of signal intensity: very low (1-51), low (52-102), medium (103-153), high (154-204) and very high (205-256).

Legend:

■ Very low ◆ Low ▲ Medium × High ○ Very high

Table 4-3. Dependence of the size of the fractions from the total area, *K* (%) that contain soot with equal intensity, on *Re* and *St* numbers.

		Level of signal intensity	↓ saturation (?)				
Re	*St*	No signal	Very low (1-51)	Low (52-102)	Medium (103-153)	High (154-204)	Very high (205-256)
4329	0.0083	98.01	1.26	0.29	0.06	0.21	0.17
	0.0106	96.04	2.79	0.38	0.10	0.46	0.23
	0.0116	97.22	1.86	0.31	0.06	0.34	0.21
	0.0139	94.02	4.02	0.68	0.17	0.68	0.43
	0.0127	96.88	2.05	0.39	0.06	0.36	0.26
	0.0175	90.90	6.19	1.05	0.18	0.93	0.75
	0.021	93.71	4.07	0.39	0.02	1.58	0.23
	0.0245	85.01	11.01	0.69	0.07	2.78	0.44
5437	0.0083	98.57	1.00	0.17	0.04	0.13	0.10
	0.0091	97.12	1.87	0.37	0.08	0.31	0.25
	0.0106	98.11	1.20	0.26	0.05	0.20	0.18
	0.0116	97.69	1.54	0.28	0.07	0.24	0.17
	0.0139	92.74	5.07	0.64	0.08	1.04	0.44
	0.0167	91.23	6.53	0.68	0.08	1.04	0.45
	0.0195	82.38	12.31	0.94	0.11	3.66	0.59
6555	0.0061	98.44	1.07	0.17	0.06	0.14	0.11
	0.0069	97.43	1.96	0.22	0.09	0.18	0.12
	0.0091	97.52	1.61	0.30	0.08	0.27	0.21
	0.0116	96.69	2.23	0.39	0.11	0.34	0.24
	0.0139	90.88	6.39	0.98	0.21	0.92	0.61
	0.0162	81.23	13.79	1.79	0.20	1.86	1.13
7682	0.0069	98.87	0.74	0.15	0.03	0.11	0.10
	0.0083	98.57	0.91	0.20	0.04	0.15	0.14
	0.0091	97.67	1.58	0.27	0.03	0.23	0.22
	0.0106	96.89	2.08	0.38	0.05	0.30	0.30
	0.0116	95.51	3.02	0.52	0.11	0.49	0.35
	0.0139	82.14	13.08	1.28	0.12	2.59	0.78

Typical distribution of the zones of soot formation at various *Re* numbers and constant *St* number of 0.0116 are shown in Figure 4-4. Figure 4-5 presents typical distributions of the zones of soot formation at various *St* numbers and constant *Re* number of 7682.

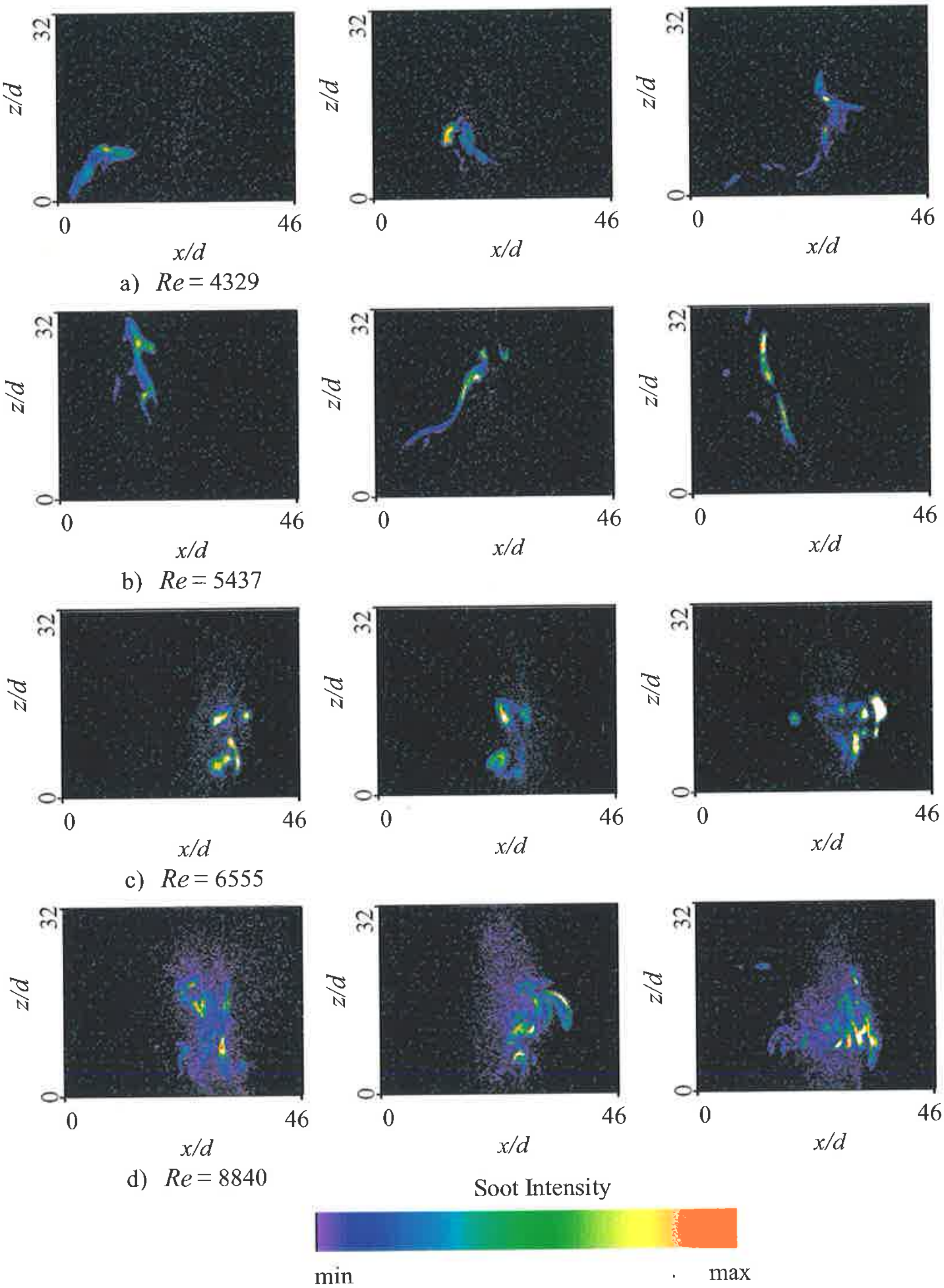

a) *Re* = 4329

b) *Re* = 5437

c) *Re* = 6555

d) *Re* = 8840

Fig. 4-5. Typical distribution of the zones of soot formation at various *Re* numbers and constant *St* number of 0.0116. The phase of the jet precession is the same in each image, with the jet emerging in the plane of the light sheet. The vertical distance of the bottom of the images above the jet exit is 14 *d* and the axis of rotation corresponds to the middle of the image.

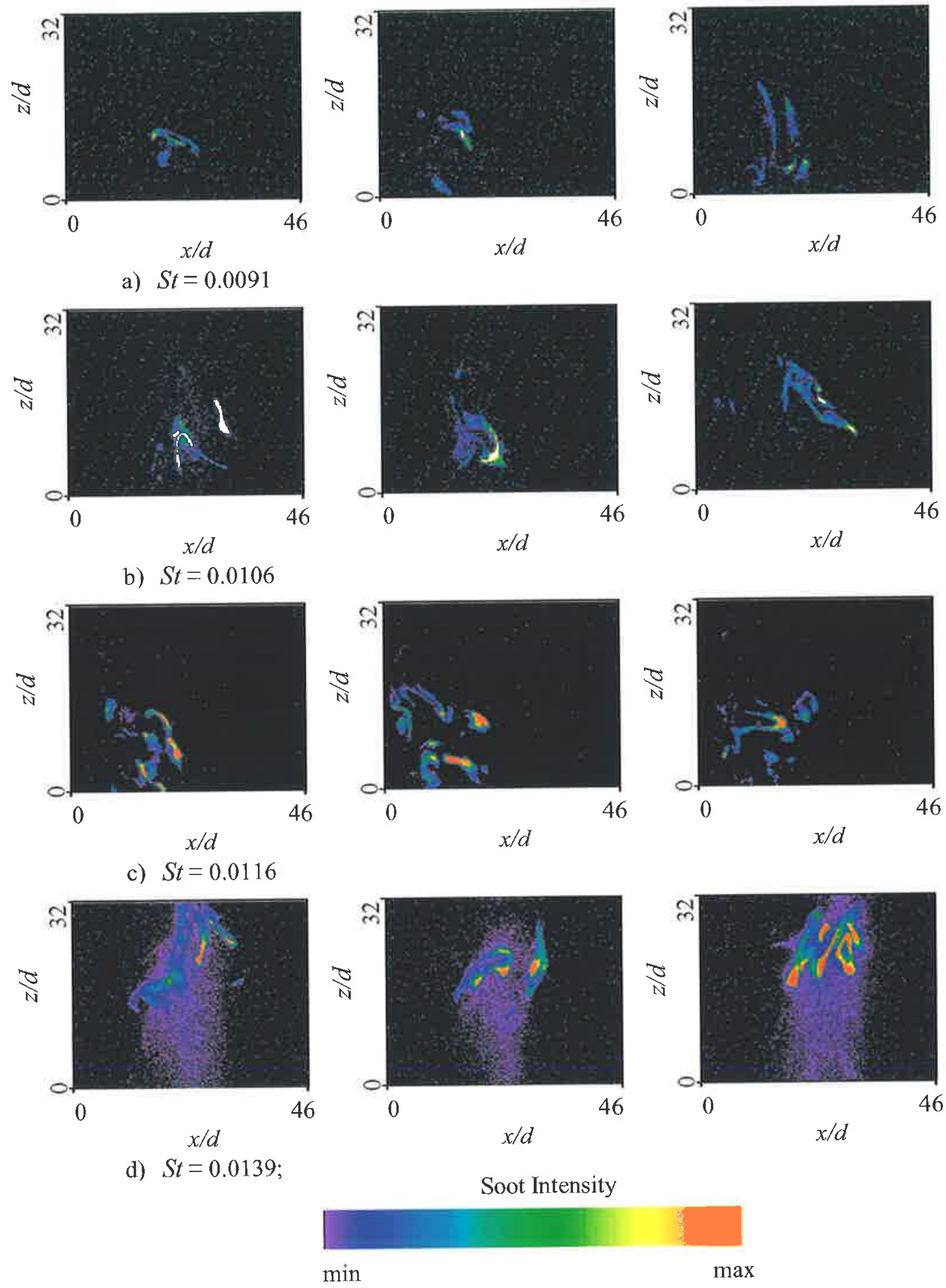

a) $St = 0.0091$

b) $St = 0.0106$

c) $St = 0.0116$

d) $St = 0.0139$;

Fig. 4-6. Typical distribution of the zones of soot formation at various *St* numbers and constant *Re* number of 7682. The phase of the jet precession is the same in each image, with the jet emerging in the plane of the light sheet. The vertical distance of the bottom of the images above the jet exit is 14 *d* and the axis of rotation corresponds to the middle of the image.

4.2. Discussion

The instantaneous images (see Figure 4-4,5) reveal that soot is predominantly formed in sheets of varying thickness. As expected, very little soot is observed in the near nozzle region, consistent with the idea that the formation of soot in appreciable quantities is kinetically limited (see Turns *et al.*, (1989)). Also readily observable is a wide variety of soot zone structure types in the flames. As mentioned in the previous section, there are very broad regions of low signal spanning much of the flame (eg. Figures 4-5d and 4-6d). These broad regions are more prevalent in the high *St* number flames where strain rates are lower and residence times are longer (Newbold *et al.*, 1996, 2000).

The low signal from these zones could potentially result either from Rayleigh scattering from molecules[1] or from Mie scattering from soot particles with a low concentration. The probability that these low signals results from Mie scattering from soot is high since the strength of such signals exceeds by more than 100 times the signal strength from the Rayleigh scattering (see Eckbreth (1988)). Thus, the signal strength from the Rayleigh scattering is comparable with the noise level in the current experiments and could not be distinguished from the noise.

If the hypothesis that these very broad regions of low signal result from the light scattered by low concentration soot is true, it suggests that pyrolysis may be occurring in broad regions on the fuel rich side of the dominant reaction zones. This has not been observed in these flames before and is worthy of further investigation. However the areas of low intensity signal may not be necessarily due to pyrolysis. It is also possible that these soot particles have been transported from the flame-front by circulation of hot gases (vortex motions). To resolve this question requires further, more detailed investigation.

Note that the broad low intensity zones that were observed in the current experiments may not, in fact, be uniform but layered. Turns *et al.*, (1989) observed a wide variety of soot zone structure types in the flames at Reynolds number of the jet (based on the cold fuel properties and exit diameter) of 10000 and 20000, but no such broad zones of low intensity. They used a film camera that provides much more detailed spatial resolution than the CCD array that was used in the current experiments. Use of data collection equipment that could provide better spatial resolution is something that could be recommended for future investigations.

A common concern in all two dimensional imaging of three dimensional turbulent structures is that the edges of three–dimensional soot bearing structures are impinging on the two dimensional plane at an oblique out-of-plane angle. This out-of-plane fringing could also be one of the causes for the existence of the broad low soot intensity zones. The large scale precessing nature of the flame makes this kind of out-of-plane behaviour more probable than in a simple axisymmetric jet.

Turns *et al.*, (1989) found that, in general, the largest structures have a more-or-less vertical orientation, while the smaller-scale streaks and swirls appear to be of more random orientation. The vortical structures in the present flames appear to be more prevalent for the higher Reynolds number flames and, in the upper region of the flames, soot zones are

---

[1] The Rayleigh scattering is usually associated with dispersion of electromagnetic radiation by particles that have a radius less than approximately 1/10 the wavelength of the radiation.

frequently disconnected. This is consistent with increased three-dimensionality in the structure with increased Reynolds number. In the current study, it was found that the thickness of the high concentration sheets of soot is substantial, often reaching 30-40 *mm*. The sheets are found to be gently curved, and not highly strained, also consistent with the global measurements of Newbold *et al.* (1997), who found that these unconfined PJ flames are dominated by buoyancy and low strain. This supports the hypothesis that low strain in a diffusion flame promotes soot formation and high emissivity (ie. soot formation correlates inversely with flame strain). There is also a trend of less soot being present at the lower Strouhal numbers. The observation that soot formation is favoured by reduced low strain rates is consistent with the pioneering work of Kent and Bastin (1984).

It is still questionable whether the thin soot-bearing structures observed in many images can be associated with laminar flamelets[1]. Laminar flamelets can only exist where the smallest characteristic scales of turbulent motion are larger than the characteristic width of the entire flame zone for all species. However, no data are available on the Kolmogorov scale of turbulent motion, and no information is available on the characteristic flame width in terms of the major participants, i.e. the gaseous species. Note that soot has an effective molecular scale (laminar) diffusivity that is in orders of magnitude less than that of the gaseous species. Thus, even vigorous turbulent stirring will retain thin layer-like soot strata in the flow, which makes soot strata to be not good markers of characteristic flame width anyhow.

---

[1] A description of the phenomenological model of a turbulent flame as a ensemble of laminar flamelets can be found in Williams (1974), Carrier *et al.* (1975), Liew *et al.* (1984) and Miake-Lye and Toner (1987).

5. Conclusions

The Mie diagnostic technique was successfully implemented to provide qualitative visualisation of the zones of soot formation in MPJ burner flames. A range of conditionally sampled experiments was carried out. The characteristic Reynolds number based on the nozzle diameter, was varied from 4329 to 11223 and the Strouhal number based on the nozzle diameter, was varied from 0.0042 to 0.0245. The nozzle diameter was fixed at 5 *mm* and the jet exit angle at 45 degrees. The phase of the jet precession was kept the same in each image

[Experimental data were collected and used to perform semi-quantitative soot intensity calculations, using the proportionality between the intensity of the scattered signal and the number of soot particles in the flame envelope, and to estimate the soot intensity correlation with flame strain.]

The instantaneous images reveal that soot is predominantly formed in sheets of varying thickness, often reaching 30-40 *mm*. Very little soot is observed in the near nozzle region, which is consistent with the idea that the formation of soot in appreciable quantities is kinetically limited. Readily observable are very broad regions of low signal spanning much of the flame. These broad regions are more prevalent in the high *St* number flames where strain rates are lower and residence times are longer. It is most likely that these zones of low signal result from the light scattered by low concentrations of soot.

5. Conclusions

The semi-quantitative measurements of soot intensity reveal that the it increases with increase in both *Re* and *St* numbers. However, the latter is more influential.

The current observations that soot formation is favoured by reduced low strain rates (i.e. soot formation correlates inversely with flame strain) is consistent with the work of other investigators.

Recommendations for future work:

It was found that the work of the electric motor used to rotate the burner generates an intensive electro-magnetic field that leads to the appearance of an additional noise in the form of chaotic white spots in the images. The appearance of such a non-optical noise could be reduced in future work by an installation of a metal shield to surround the engine.

There are very broad regions of low signal spanning much of the flame that could result from the light scattered by low concentrations of soot. If this hypothesis is true, then it is necessary to determine whether this soot results from pyrolysis on the fuel-rich sides of the reaction zones, or if it is recirculated soot that has been transported from the flame-front by circulation of hot gases (vortex motions).

The broad low intensity zones that were observed in the current experiments may not be uniform but layered. To reveal this, it would be necessary to use in future experiments a data acquisition system that allows better spatial resolution.

5. Conclusions

Full modelling and experimental studies of soot formation in a highly turbulent diffusion flame is a formidable task. Nevertheless, the aim of the current work, to provide further insight into the relationship between flame strain and soot formation, was successfully fulfilled. More detailed studies in which parameters such as the nozzle exit angle and diameter are varied would provide significant additional information.

6. References

Bachmann M, Wiese S, Homann KH (1994) *Proc. Combustion Institute*, 25, pp. 635–643.

Becker HA (1977) Mixing, Concentration Fluctuations, and Marker Nephelometry. *Studies in Convection,* 12, edited by BE Launder, Academic Press, New York, pp. 45-139.

Becker HA, Hottal HC, Williams GC (1967a) On the Light-scattering Technique for the Study of Turbulence and Mixing. *J. Fluid Mech.*, 30, pp. 259-284.

Becker HA, Hottal HC, Williams GC (1967b) The Nozzle-fluid Concentration Field of the Round, Turbulent, Free Jet. *J. Fluid Mech.*, 30, pp. 285-303.

Becker HA, Hottal HC, Williams GC (1963) Mixing and Flow in Ducted Turbulent Jets. *Proc. Combustion Institute*, 9, pp. 7-20.

Calcote HF, Gill RJ (1994) *Soot Formation in Combustion* (H. Bockhorn, Ed.) Springer, Berlin, pp. 471–482.

Calcote HF, Olson DB, Keil DG (1988) *Energy Fuels*, 2, pp. 494 –504.

Carrier GF, Fendell FW, Marble FE ()1975) *SIAM J. Appl. Math.*, 28, pp. 463-500.

Chao YC, Ham JM, Jeng MS (1990) A quantitative laser sheet image processing method for the study of the coherent structure of a circulate jet flow. *Experiments in Fluids,* 6, pp. 323-332.

Clemens NT, Mungal MG (1991) A planer Mie scattering technique for visualizing supersonic mixning flows. *Experiments in Fluids*, 11, pp. 175-185.

Dimotakis PE, Miake-Lye RC, Parantoniou DA (1983) Structure and dynamice of round turbulent jets. *Phys. Fluids*, 26, pp. 3185-3192.

Du J, Axelbaum RL (1995) The Effect of Flame Structure on Soot-Particle Inception in Diffusion Flames. *Combustion and Flame*, 100, pp. 367-375.

6. References

Du J, Axelbaum RL, Law CK (1988) Experiments on the Sooting Limits of Aerodynamically-Strained Diffusion Flames. *Proc. Combustion Institute*, 22, pp. 387-394.

Eckbreth AC (1977) Effects of laser modulated particulate incandescence on Raman scattering diagnostics. *J.Appl. Phys.,*48, pp. 4473-4479.

Eckbreth AC (1988) *Laser Diagnostics for Combustion Temperature and Species.* Abacus Press, UK.

Everest DA, Driscoll JF, Feikema DA (1995) Images of the Two-Dimentional Field and Temperature Gradients to Quantify Mixing Rates within a Non-Premixed Turbulent Jet Flame. *Combustion and Flame*, 101, pp. 58-68.

Fialkov AB *Prog.* (1997) *Energy Combust. Sci,.* 23, pp. 399 –528.

Frenklach M, Wang H (1991) *Proc. Combustion Institute,* 23, pp. 1559–1566.

Frenklach M, Warnatz J (1987) *Combust. Sci. Technol.*, 51, pp. 265–283.

Gaydon AG, Wolfhard HG (1979) Flames, Their Structure, Radiation and Temperature, 4th ed. *Chapman & Hall,* London, pp. 232.

Graham SM, Goodings JM (1984) *Int. J. Mass Spectrom. Ion Proc.*, 56, pp. 205-222.

Hall-Roberts VJ, Hayhurst AN, Knight DE, Taylor SG (2000) *Combustion and Flame,* 120, pp.578 –584.

Hanson RK (1986) Combustion diagnostics: Planer imaging techniques. *Proc. Combustion Institute*, 21, pp. 1677-1691.

Hayhurst A N, Jones HRN (1989) *Combustion and Flame*, 78, pp. 339 –356.

Hayhurst AN, Jones HRN (1982) *Nature,* 296, pp. 61 63.

Hayhurst AN, Jones HRN (1987) *J. Chem. Soc. Faraday Trans,.* 83, pp. 1–27.

Homann KH, Wagner HG (1967) *Proc. Combustion Institute*, 11, pp. 371–378.

6. References

Hussman AW, Maybach GW (1961)The Film Vaporizer Combustor. *SAE Transactions*, 69, pp. 563-574.

ICCD Detector Operation Manual, Version 3.B, P/N 4411-0009, Princeton Instruments Inc., Trenton, NJ, USA.

Kent JH, Bastin SJ (1984) Parametric Effects on Sooting in Turbulent Acetylene Diffusion Flames. *Combustion and Flame*, 56, pp. 29-42.

Liew SK, Bray KNC, Moss JB (1984) *Combustion and Flame*, 56, pp. 199-213.

Lin K-C, Faeth GM (1996a) Effects of Hydrodynamics on Soot Formation in Laminar Opposed-Jet Diffusion Flames. *Propulsion and Power*, 12, pp. 691-698.

Lin K-C, Faeth GM (1996b) Hydrodynamic Suppression of Soot Emissions in Laminar Diffusion Flames. *Propulsion and Power*, pp. 10-17.

Melton LA (1984) Soot diagnostics based on laser heating, *Appl. Opt.*23, pp. 2201-2208.

Miake-Lye RC, Toner SJ (1987), *Combustion and Flame*, 67, pp. 9-26.

Mie G (1908) Contributions to the Optics of Turbid Media, Especially Colloidal Suspensions of Metals, *Ann. Phys.* 25, pp. 377-445.

Nathan GJ, Turns SR, Bandaru RV (1996) The Influence of Jet Precession on NO_x Emissions and Radiation from Turbulent Flames. *Combustion Science and Technology*, 112, pp. 211-230.

Newbold GJR, Nathan GJ, Luxton RE (1997) Large-Scale Dynamics of an Unconfined Precessing Jet Flame. *Combustion Science and Technology*, 126, pp. 71-95.

Newbold GJR, Nathan GJ, Nobes DS, Turns SR (2000) Measurement and Prediction of NO_x Emissions from Unconfined Propane Flames from Turbulent-Jet, Bluff-body, Swirl and Precessing Jet Burners. *Proc. Combustion Institute*, 28, pp. 481-487.

6. References

Ni T, Pinson JA, Gupta S, Santoro RJ (1995) Two-dimensional imaging of soot volume fraction by the use of laser-induced incandescence. *Appl. Opt.*, 30, pp. 7083-7091.

Nobes DS, Newbold GJR, Nathan GJ, Luxton RE, Alwahabi ZT, King KD (1996) Phase Average Planar Imaging of Concentration of a Precessing Jet Flow. *First Australian Conference on Laser Diagnostics in Fluid Mechanics and Combustion, The University of Sydney, Australia,* pp. 154-159.

Nobes DS, Newbold GJR, Nathan GJ, Luxton RE, Alwahabi ZT, King KD (1997) The Mixing Field of a Simple Round Turbulent Jet and a Fluidic Precessing Jet. *The First Asia-Pacific Conference on Combustion, Osaka, Japan*, pp. 334-337.

Programmable Pulse Generator Model PG-200 Operation Manual (1997).

Quantel BrilliantB Instruction Manual (1996).

Rosensweig RE, Hoyt HC, Williams GC (1961) *Chem. Eng. Sci*, 15, 11.

Schefer RW, Kerstein AR, Namazian M, Kelly J (1994) Role of large-scale structure in a nonreacting turbulent CH_4 jet. *Phys. Fluids,* 16, pp. 652-661.

Schneider GM, Froud D, Syred N, Nathan GJ, Luxton RE (1997) Velocity measurements in a precessing jet flow using a three dimensional LDA. *Experiments in Fluids*, pp. 89-98.

Shaddix CR, Smyth KC (1996) *Combustion and Flame*, 107, pp. 418-452.

Sony Corporation (1998) Digital Video Camera Recorder Model DCR-TRV900E, Operating Instructions.

Spyglass Transform Quick Tour and Reference (1993), Fourth Edition, Spyglass Inc. Orbana-Champaign, Ilinois.

ST-138 Controller Operational Manual (1998), Version 3, Revision E, Princeton Instruments Inc., Trenton, NJ, USA.

6. References

Stamatova LI, King KD, Alwahabi ZT, Nathan GJ (2002) A Mie Scattering Investigation of the Zones of Soot Formation in Precessing Jet Flames, *Third Australian Conference on Laser Diagnostics in Fluid Mechanics and Combustion*, The University of Queensland, Brisbane, CD-ROM, Paper # 2 (7 pp.).

Sugiyama G (1994) Nonluminous Diffusion Flame of Diluted Acetylene in Oxygen Enriched Air. *Proc. Combustion Institute*, 25, pp. 601-608.

Sunderland PB, Mortazavi S, Faeth GM, Urban DL (1994) Laminar Smoke Points of Nonbuoyant Jet Diffusion Flames. *Combustion and Flame*, 96, pp. 97-103.

Turns SR, Lovett JA, Sommer HJ III (1989) Visualization of Soot Zones in Turbulent Diffusion Flames. *Combustion and Flame*, 77, pp. 405-409.

Williams FA (1974) in *Turbulent Mixing in Nonreactive and Reactive Flows* (Murthy SNB, Ed.), Plenum Press, New York, p. 189.

Williams FA (1985) *Combustion Theory.* Benjamin/Cummings. Menlo Pak, CA, USA.

Wu KT, Essenhigh RH (1984) Mapping and Structure of Inverse Diffusion Flames of Methane. *Proc. Combustion Institute*, 20, pp. 1925-1932.

Appendix A

Contents of Appendices and a Summary of the Experimental Conditions

Table A. Experimental conditions and index of the images location.

No.	*Re*	*St*	f_p (*Hz*)	*P* (*kPa*)	U_0 ($m\,s^{-1}$)	Appendix No.
1	4329	0.0056	16.0	5.0	14.30	A-1
2	5437	0.0056	20.0	6.0	17.96	A-2
3	6555	0.0056	24.2	7.0	21.65	A-3
4	7682	0.0056	28.2	8.0	25.38	A-4
5	8840	0.0056	32.3	9.5	29.20	A-5
6	10012	0.0056	36.3	11.0	33.08	A-6
7	11223	0.0056	40.3	13.0	37.08	A-7
8	4329	0.0061	17.6	5.0	14.30	A-8
9	5437	0.0061	22.0	6.0	17.96	A-9
10	6555	0.0061	27.0	7.0	21.65	A-10
11	7682	0.0061	31.5	8.0	25.39	A-11
12	8840	0.0061	36.0	9.5	29.20	A-12
13	11223	0.0061	45.0	13.0	37.08	A-13
14	4329	0.0069	20.0	5.0	14.30	A-14
15	6555	0.0069	30.0	7.0	21.66	A-15
16	7682	0.0069	35.0	8.0	25.39	A-16
17	8840	0.0069	40.0	9.5	29.20	A-17
18	11223	0.0069	51.8	13.0	37.08	A-18
19	4329	0.0083	24.0	5.0	14.30	A-19
20	5437	0.0083	30.0	6.0	17.96	A-20
21	6555	0.0083	36.3	7.0	21.65	A-21
22	7682	0.0083	42.3	8.0	25.38	A-22
23	8840	0.0083	48.4	9.5	29.20	A-23
24	10012	0.0083	54.4	11.0	33.08	A-24
25	11223	0.0083	60.5	13.0	37.08	A-25
26	4329	0.0091	26.4	5.0	14.30	A-26
27	5437	0.0091	33.0	6.0	17.96	A-27
28	6555	0.0091	40.0	7.0	21.65	A-28
29	7682	0.0091	46.6	8.0	25.38	A-29
30	8840	0.0091	53.3	9.5	29.20	A-30
31	10012	0.0091	60.0	11.0	33.08	A-31
32	11223	0.0091	66.0	13.0	37.08	A-32
33	4329	0.0106	30.5	5.0	14.30	A-33
34	5437	0.0106	38.0	6.0	17.96	A-34
35	6555	0.0106	46.0	7.0	21.65	A-35

36	7682	0.0106	54.0	8.0	25.38	A-36
37	8840	0.0106	61.7	9.5	29.20	A-37
38	10012	0.0106	70.0	11.0	33.08	A-38
39	4329	0.0116	33.3	5.0	14.30	A-39
40	5437	0.0116	41.5	6.0	17.96	A-40
41	6555	0.0116	50.0	7.0	21.65	A-41
42	7682	0.0116	59.1	8.0	25.38	A-42
43	8840	0.0116	68.0	9.5	29.20	A-43
44	4329	0.0139	40.0	5.0	14.30	A44
45	5437	0.0139	50.0	6.0	17.96	A-45
46	6555	0.0139	60.0	7.0	21.65	A-46
47	7682	0.0139	70.0	8.0	25.38	A-47
48	4329	0.0127	36.3	5.0	14.30	A-48
49	4329	0.0175	50.0	5.0	14.30	A-49
50	4329	0.0210	60.0	5.0	14.30	A-50
51	4329	0.0245	70.0	5.0	14.30	A-51
52	5437	0.0050	18.0	6.0	17.96	A-52
53	5437	0.0167	60.0	6.0	17.96	A-53
54	5437	0.0195	70.0	6.0	17.96	A-54
55	6555	0.0042	18.0	7.0	21.65	A-55
56	6555	0.0046	20.0	7.0	21.65	A-56
57	6555	0.0052	22.4	7.0	21.65	A-57
58	6555	0.0083	36.2	7.0	21.65	A-58
59	6555	0.0162	70.0	7.0	21.65	A-59
60	7682	0.0044	22.4	8.0	25.40	A-60
61	7682	0.0048	24.2	8.0	25.40	A-61
62	7682	0.0053	27.0	8.0	25.40	A-62
63	7682	0.0059	30.0	8.0	25.40	A-63
64	7682	0.0079	40.0	8.0	25.40	A-64
65	7682	0.0099	50.0	8.0	25.40	A-65
66	8840	0.0046	26.6	9.5	29.20	A-66
67	8840	0.0077	45.0	9.5	29.20	A-67
68	8840	0.0113	66.0	9.5	29.20	A-68
69	10012	0.0061	40.0	11.0	33.08	A-69
70	11223	0.0049	36.0	13.0	37.08	A-70
71	11223	0.0094	70.0	13.0	37.08	A-71

Remark: Noise in a form of the chaotic white speckles can be seen on the some of the images. This is a result of the interaction between the ICCD camera and the intensive electro-magnetic field, which was generated by the electric motor used to rotate the burner.

Legend:

Soot intensity

Appendix A-1

1. Experimental Conditions

$Re = 4329$; $St = 0.0056$; $f = 16\ Hz$; $P = 5\ kPa$; $U_0 = 14.30\ m\ s^{-1}$

2. Typical Images from the Zones of Soot Formation

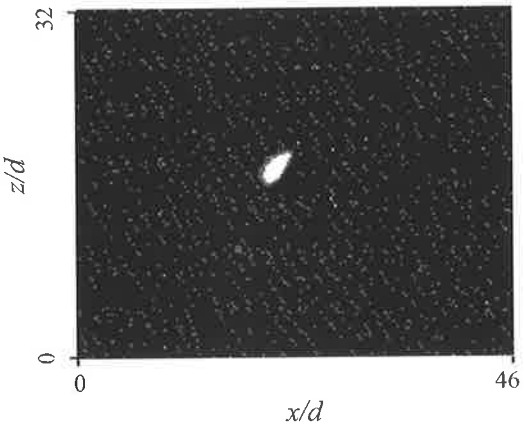

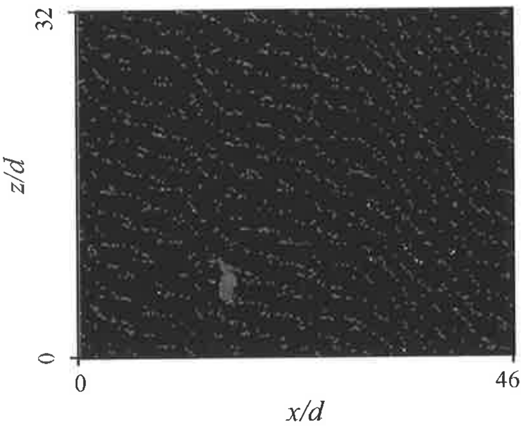

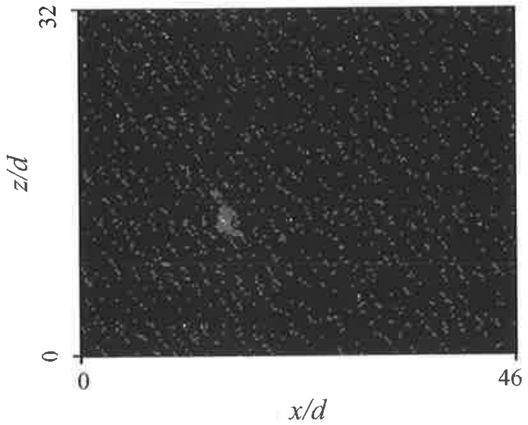

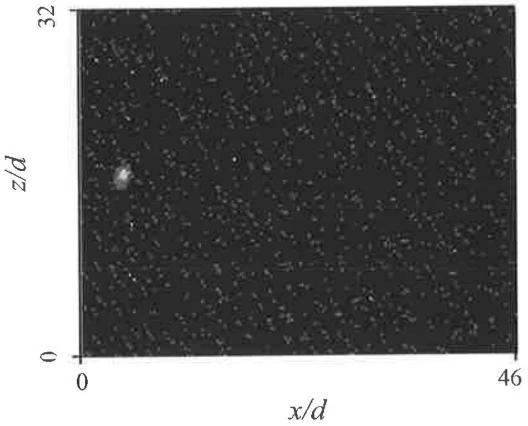

Appendix A-2

1. Experimental Conditions

$Re = 5437$; $St = 0.0056$; $f = 20\ Hz$; $P = 6\ kPa$; $U_0 = 17.96\ m\ s^{-1}$

2. Typical Images from the Zones of Soot Formation

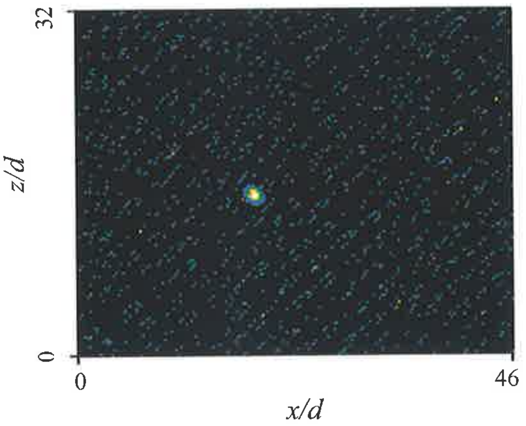

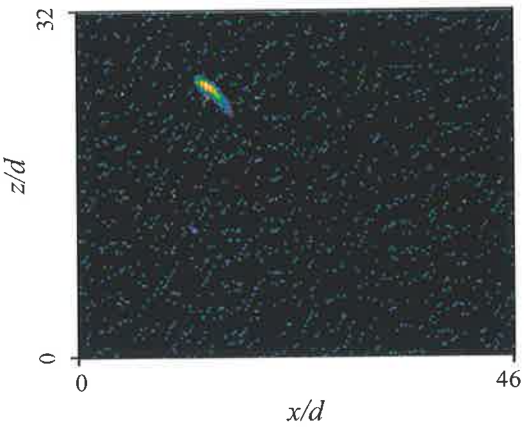

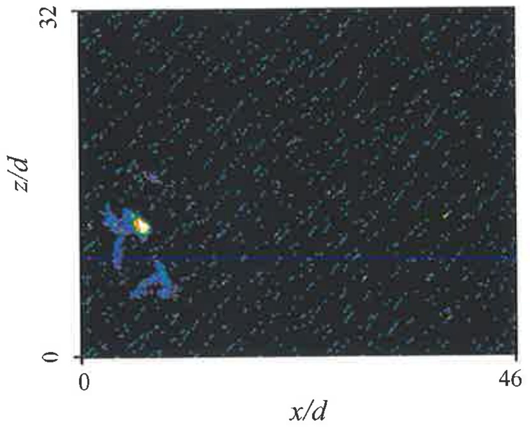

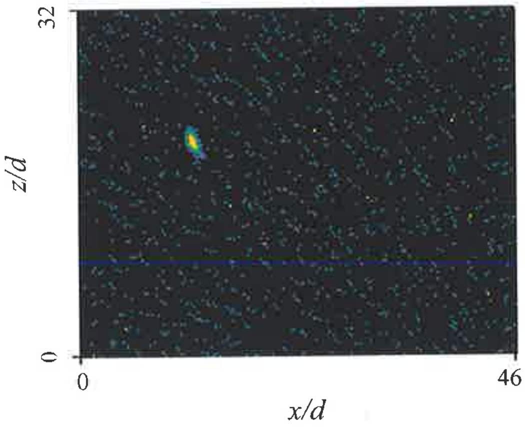

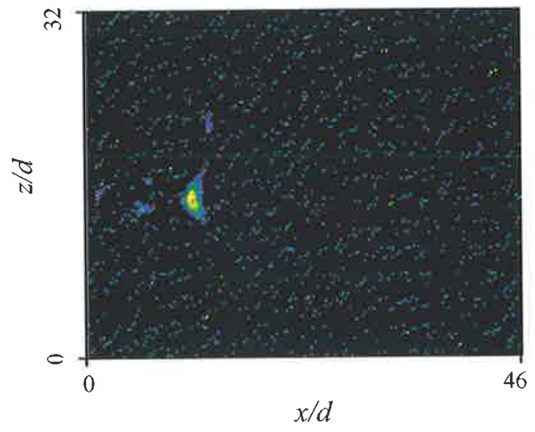

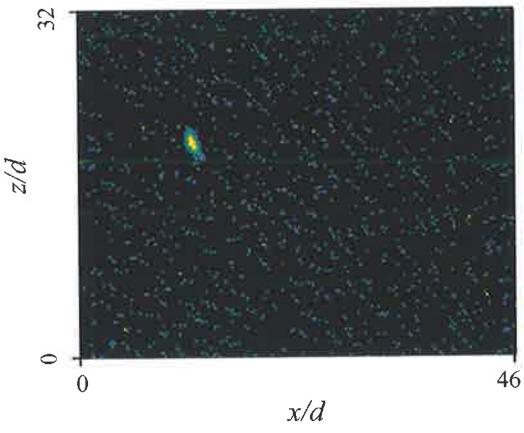

Appendix A-3

1. Experimental Conditions

$Re = 6555$; $St = 0.0056$; $f = 24.2\ Hz$; $P = 7\ kPa$; $U_0 = 21.65\ m\ s^{-1}$

2. Typical Images from the Zones of Soot Formation

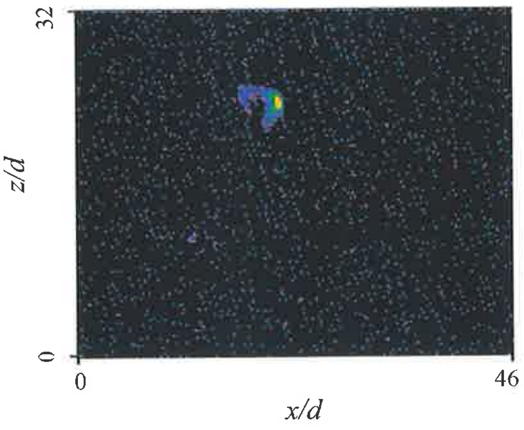

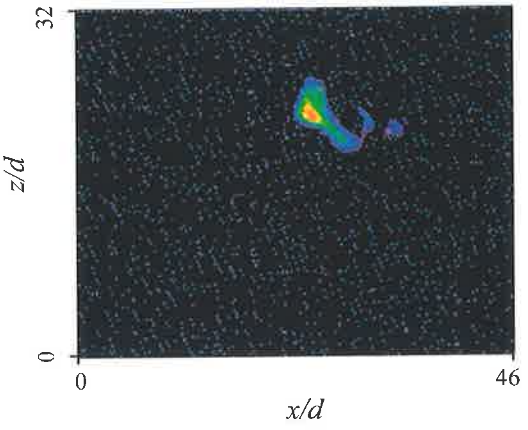

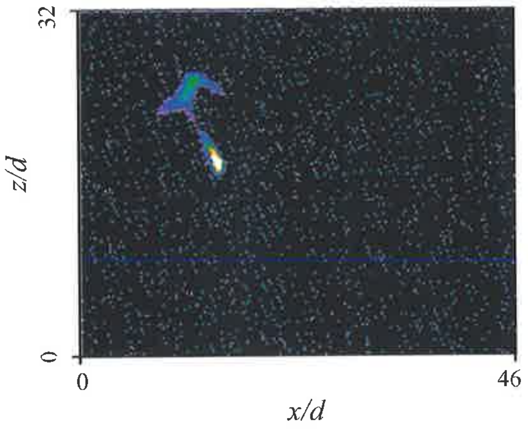

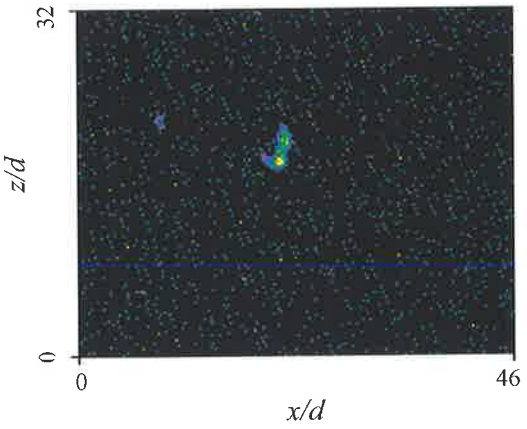

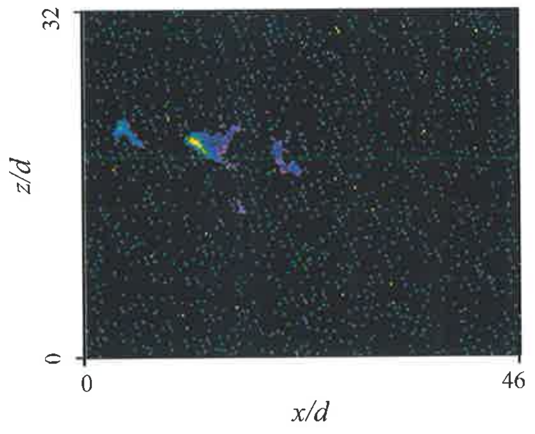

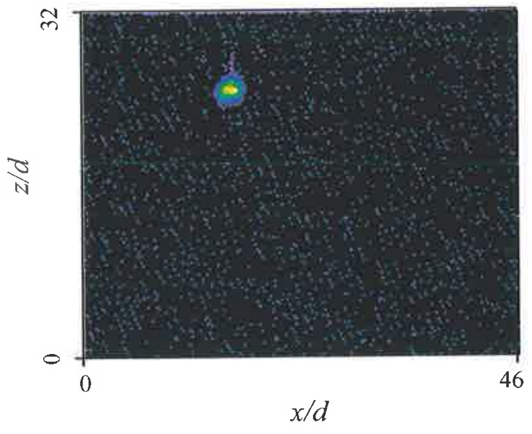

Appendix A-4

1. Experimental Conditions

$Re = 7682$; $St = 0.0056$; $f = 28.2\ Hz$; $P = 8\ kPa$; $U_0 = 25.39\ m\ s^{-1}$

2. Typical Images from the Zones of Soot Formation

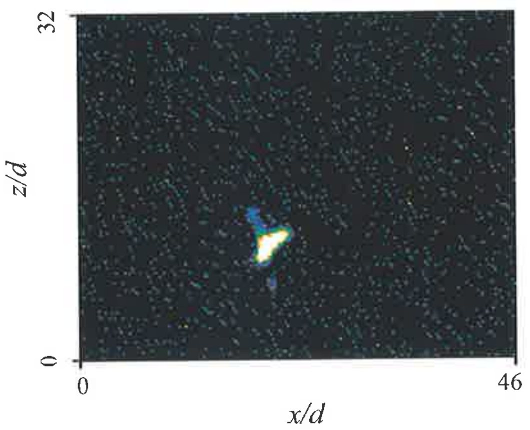

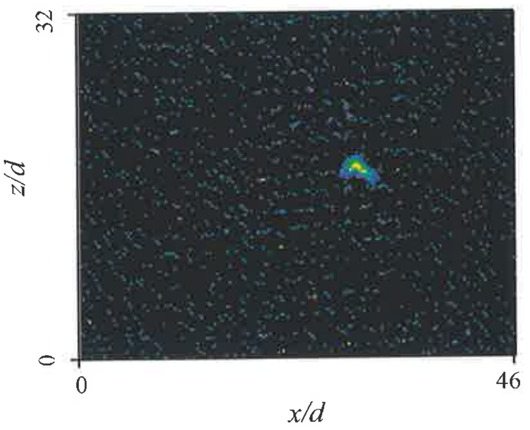

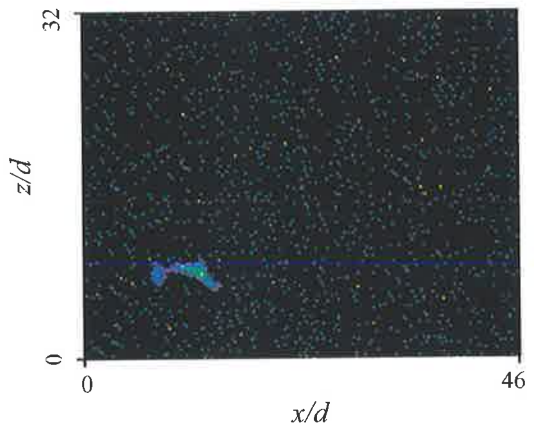

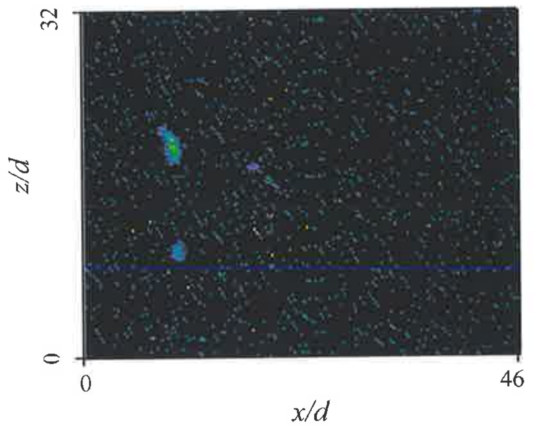

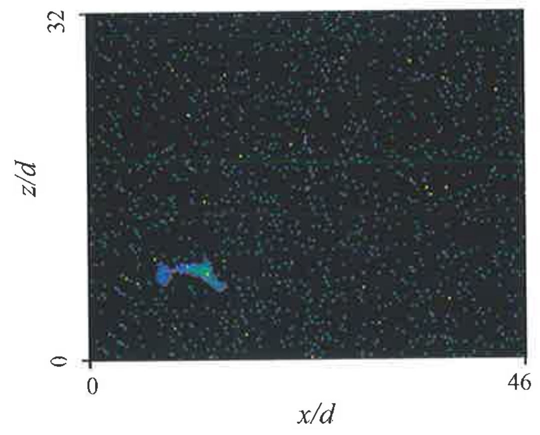

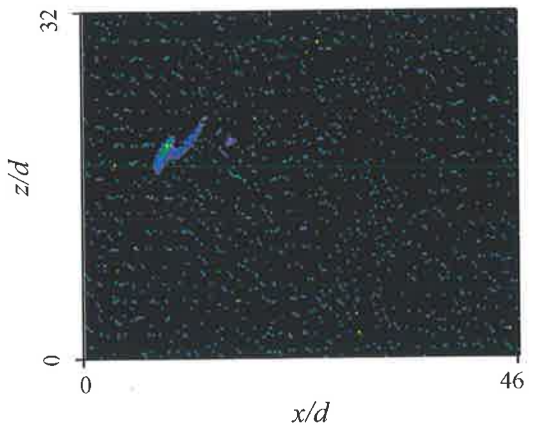

Appendix A-5

1. Experimental Conditions

$Re = 8840$; $St = 0.0056$; $f = 32.3\ Hz$; $P = 9.5\ kPa$; $U_0 = 29.20\ m\,s^{-1}$

2. Typical Images from the Zones of Soot Formation

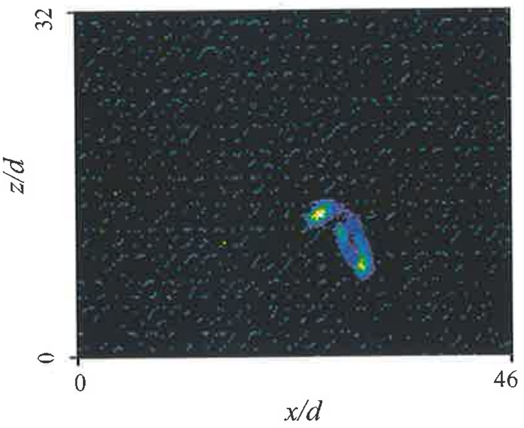

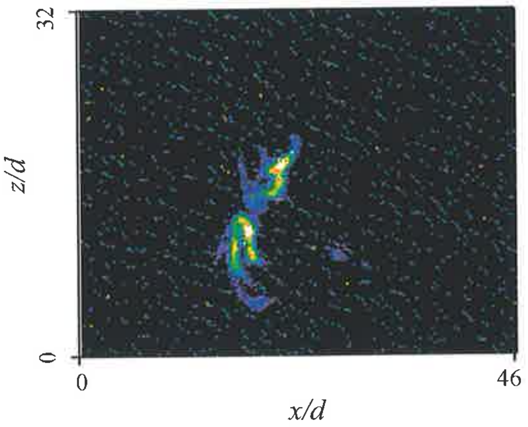

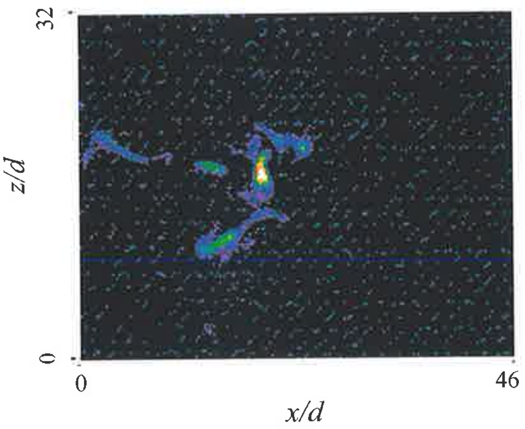

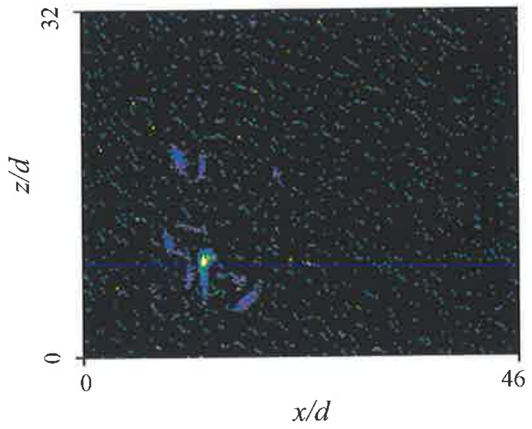

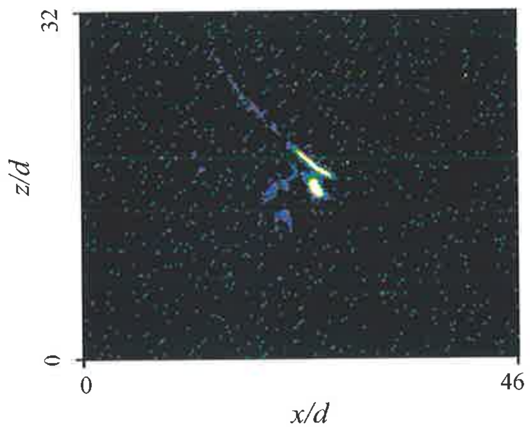

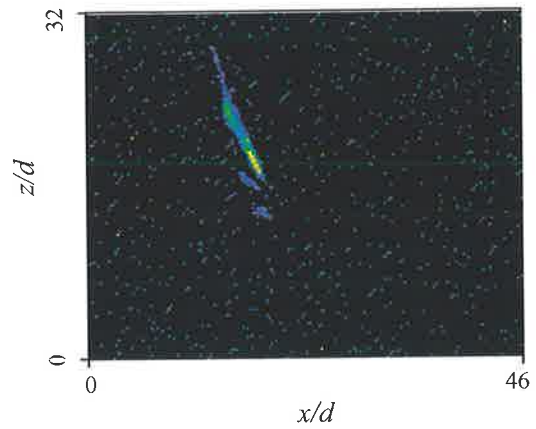

Appendix A-6

1. Experimental Conditions

$Re = 10012$; $St = 0.0056$; $f = 36.3\ Hz$; $P = 11\ kPa$; $U_0 = 38.08\ m\,s^{-1}$

2. Typical Images from the Zones of Soot Formation

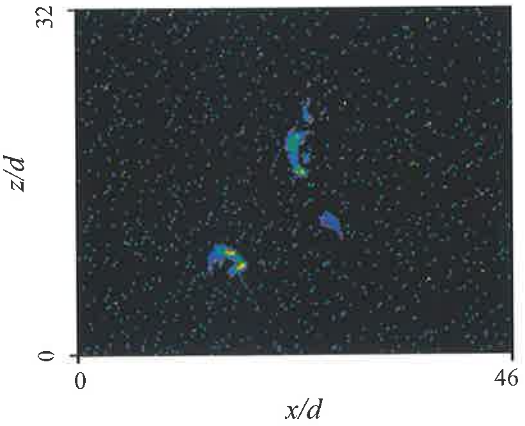

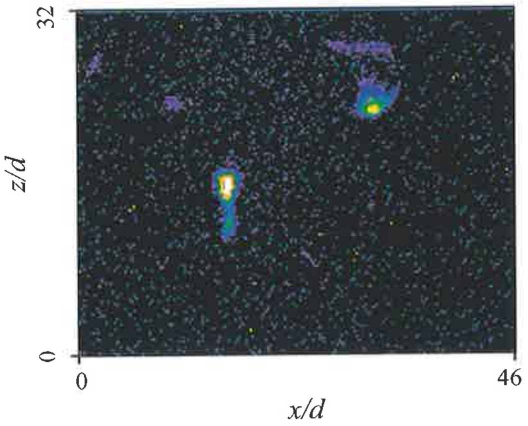

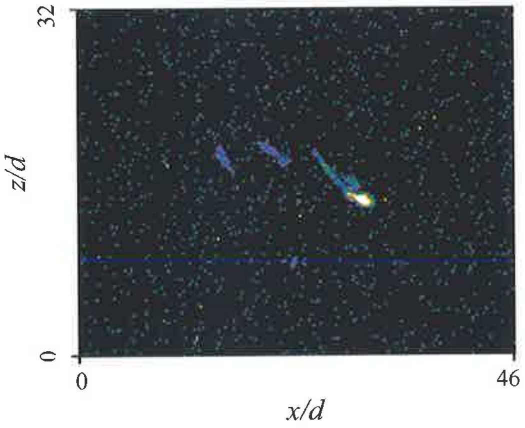

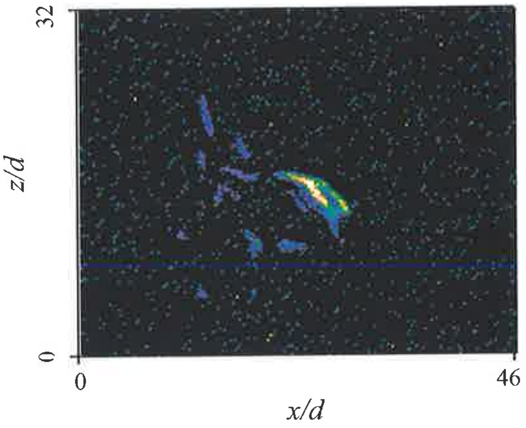

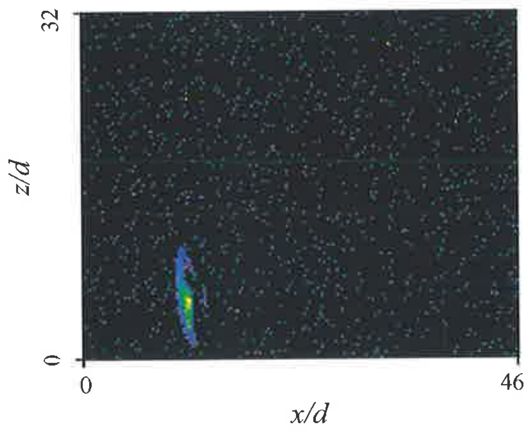

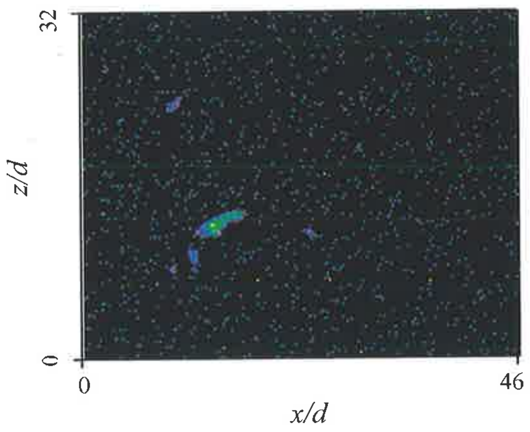

Appendix A-7

1. Experimental Conditions

$Re = 11223$; $St = 0.0056$; $f = 40.3\ Hz$; $P = 13\ kPa$; $U_0 = 37.08\ m\ s^{-1}$

2. Typical Images from the Zones of Soot Formation

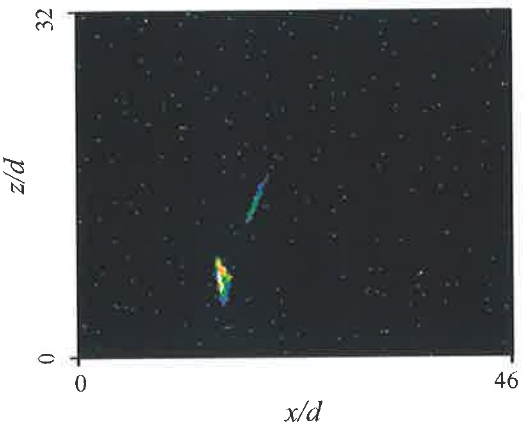

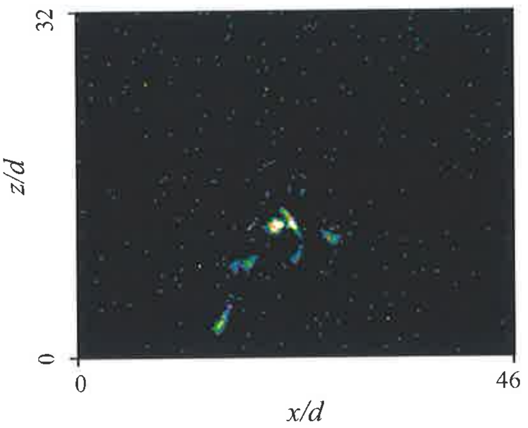

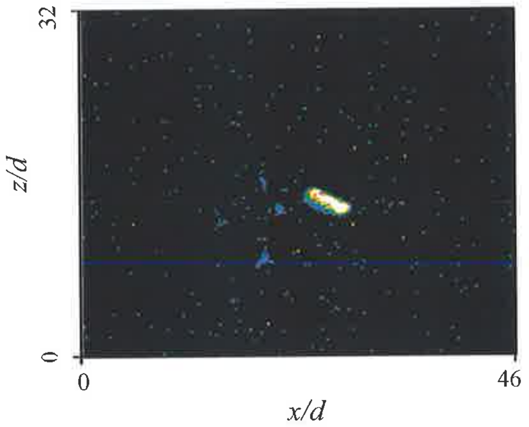

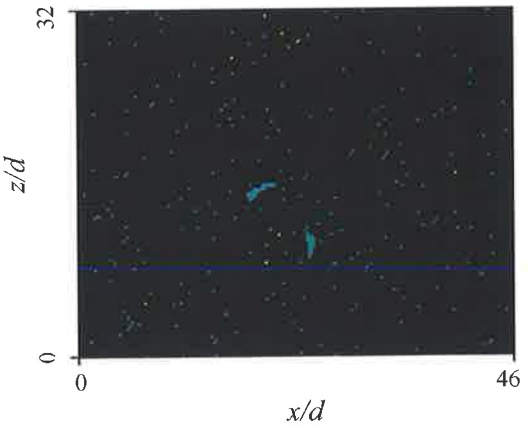

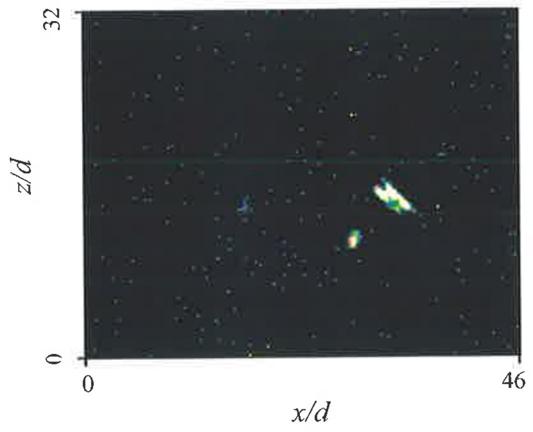

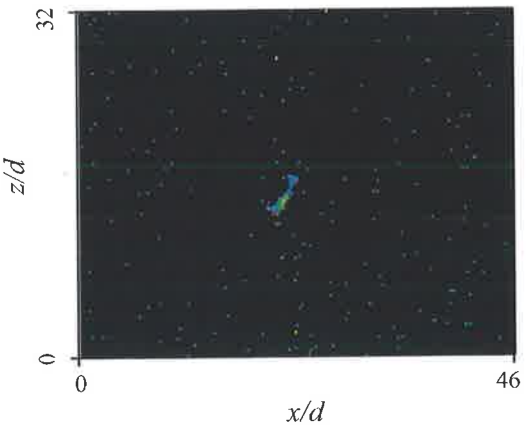

Appendix A-8

1. Experimental Conditions

$Re = 4329$; $St = 0.0061$; $f = 17.6\ Hz$; $P = 5\ kPa$; $U_0 = 14.30\ m\ s^{-1}$

2. Typical Images from the Zones of Soot Formation

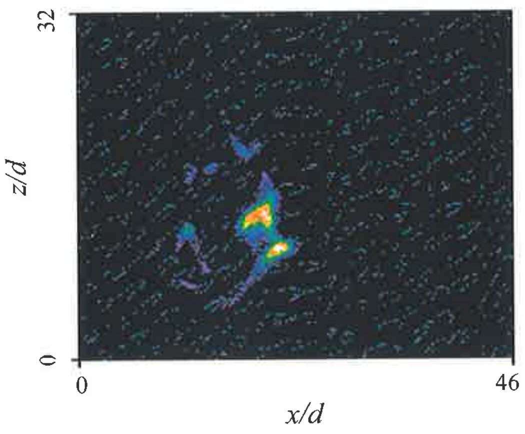

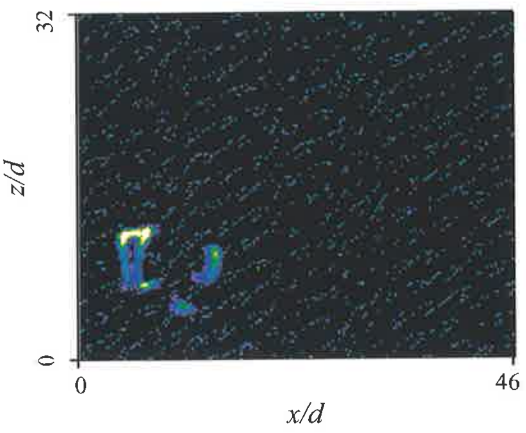

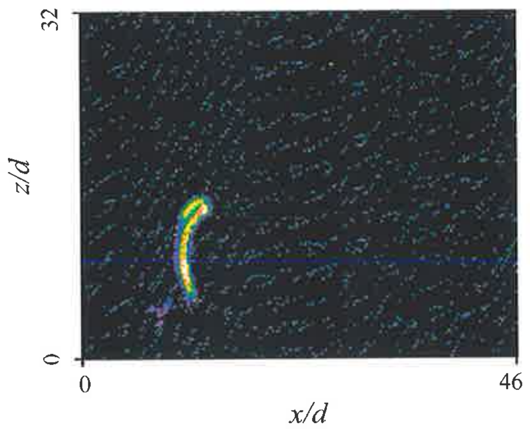

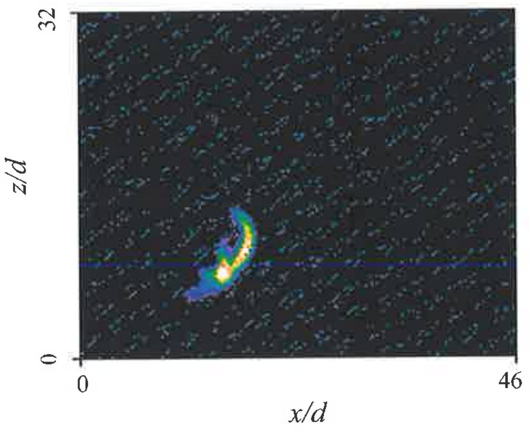

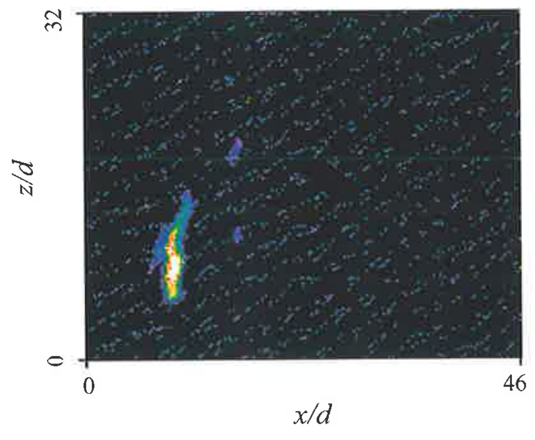

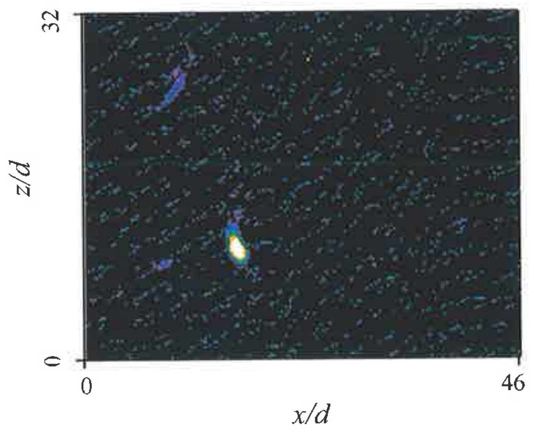

Appendix A-9

1. Experimental Conditions

$Re = 5437$; $St = 0.0061$; $f = 22\ Hz$; $P = 6\ kPa$; $U_0 = 17.96\ m\ s^{-1}$

2. Typical Images from the Zones of Soot Formation

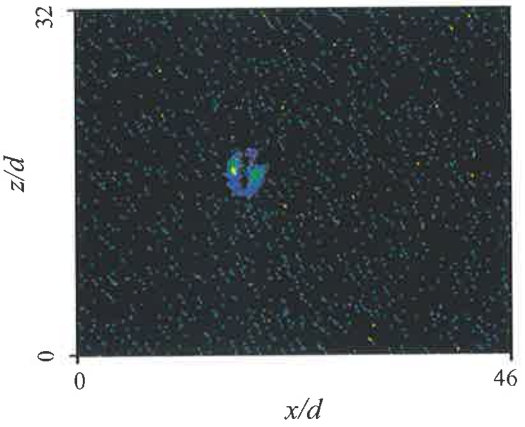

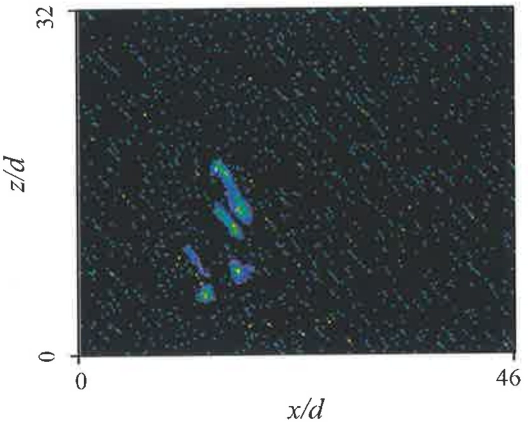

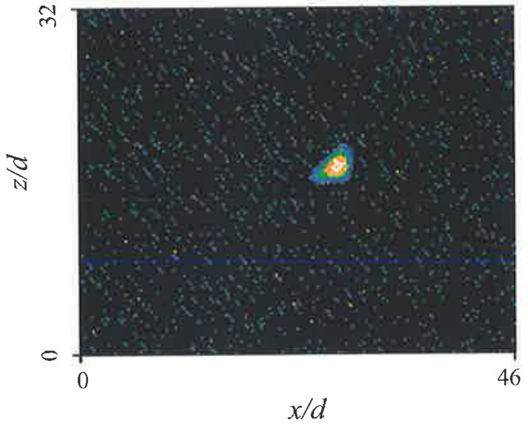

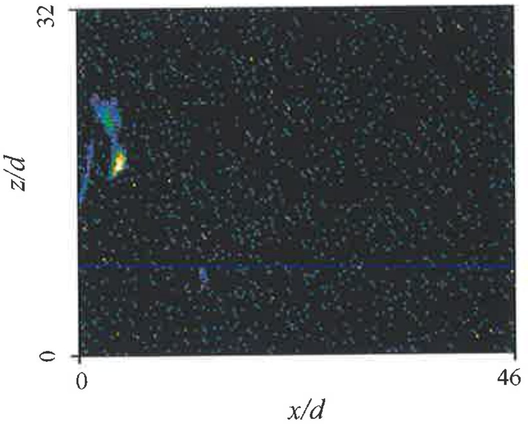

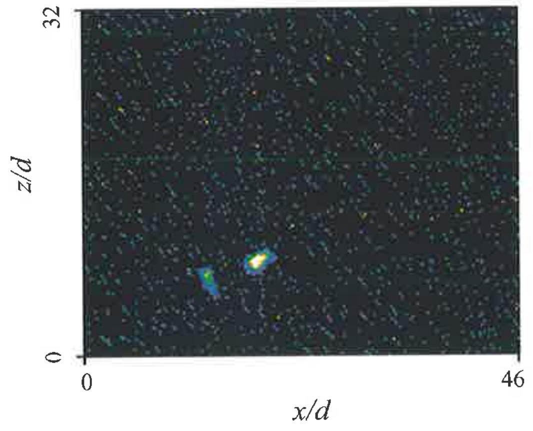

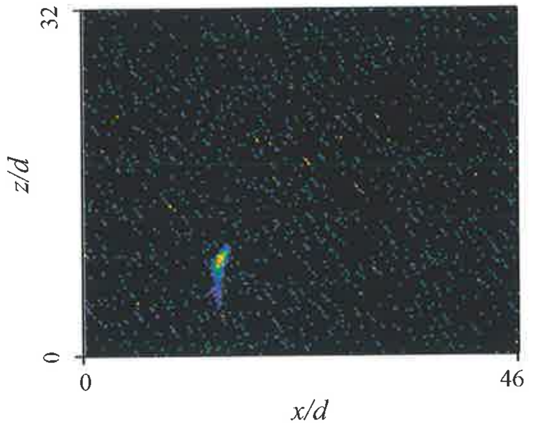

Appendix A-10

1. Experimental Conditions

$Re = 6555$; $St = 0.0061$; $f = 27\ Hz$; $P = 7\ kPa$; $U_0 = 21.65\ m\ s^{-1}$

2. Typical Images from the Zones of Soot Formation

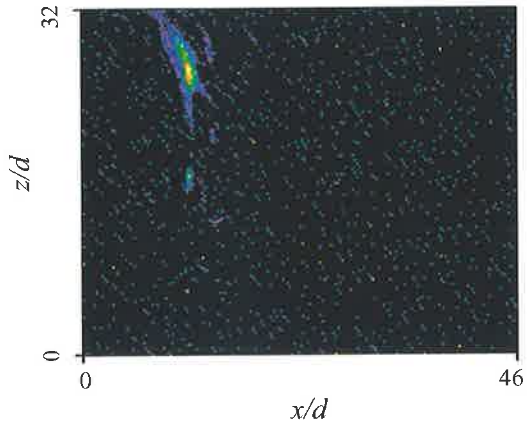

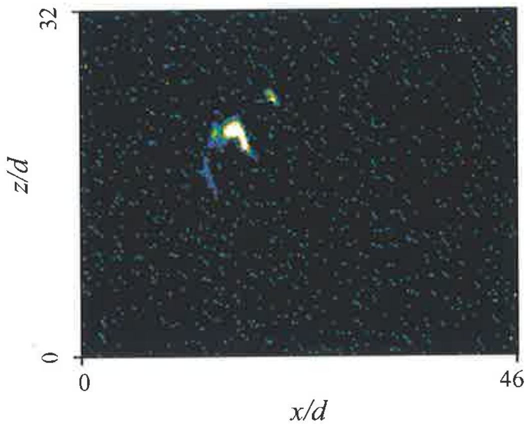

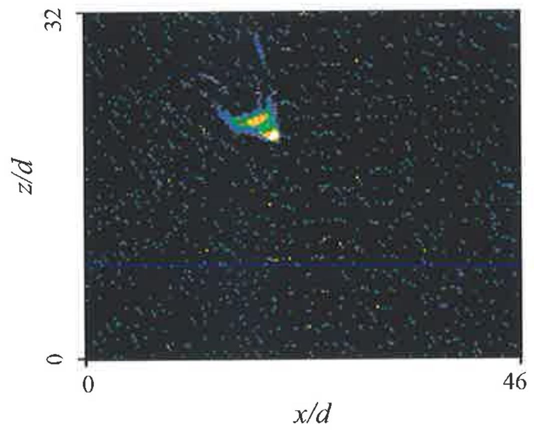

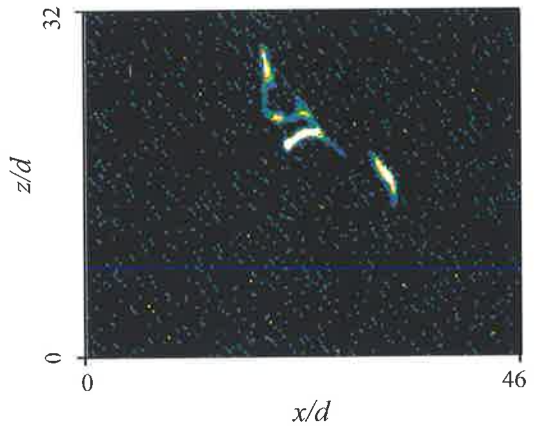

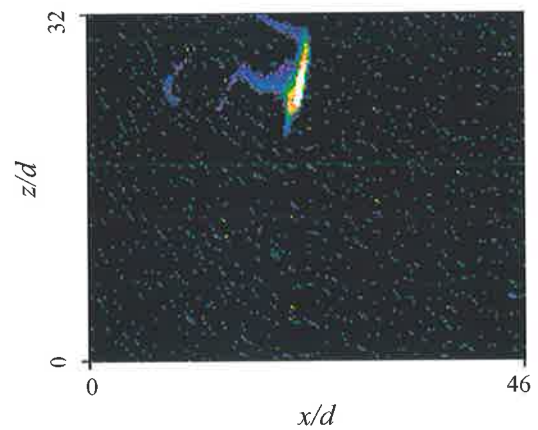

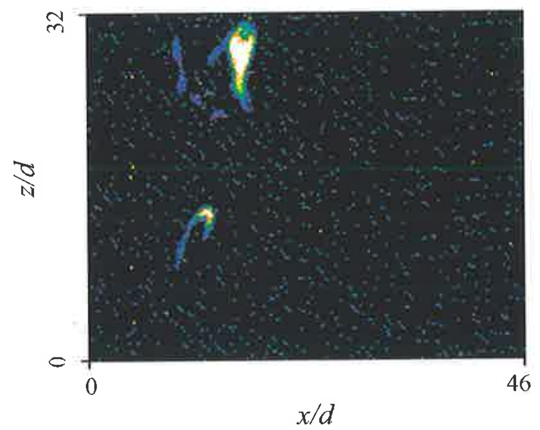

Appendix A-11

1. Experimental Conditions

$Re = 7682$; $St = 0.0061$; $f = 31.5\ Hz$; $P = 8\ kPa$; $U_0 = 25.39\ m\ s^{-1}$

2. Typical Images from the Zones of Soot Formation

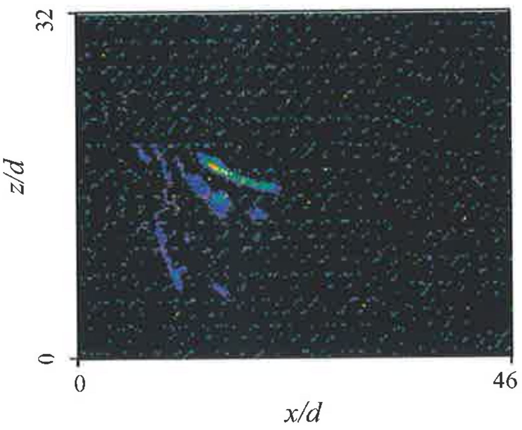

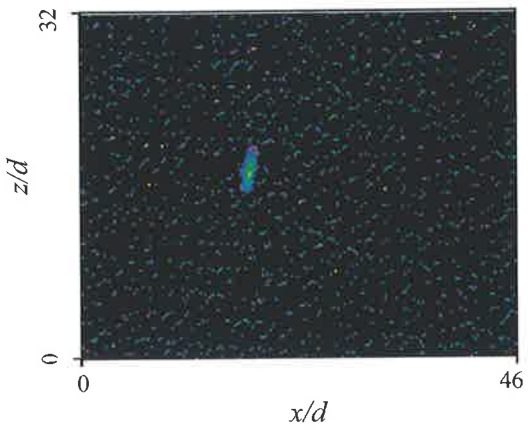

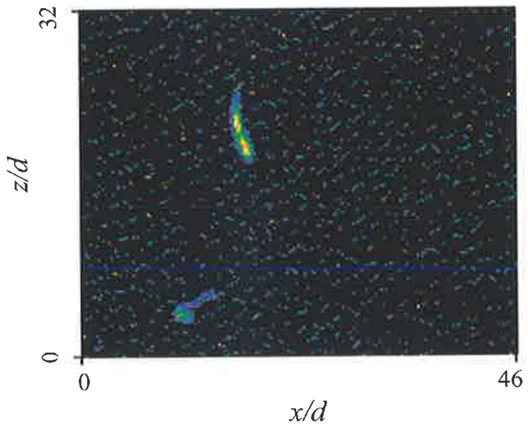

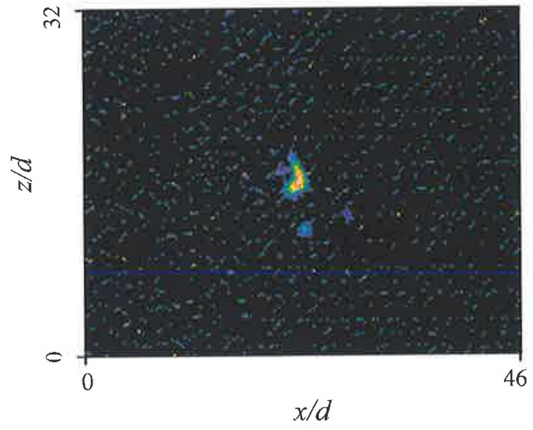

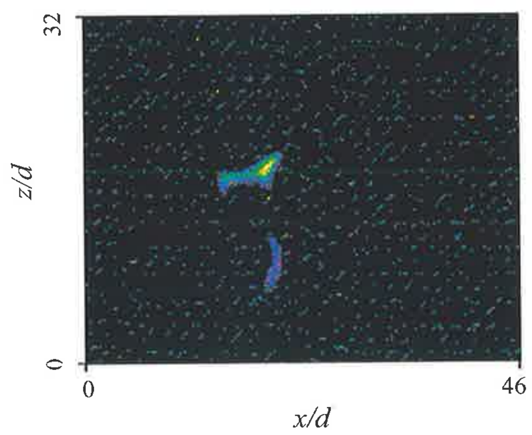

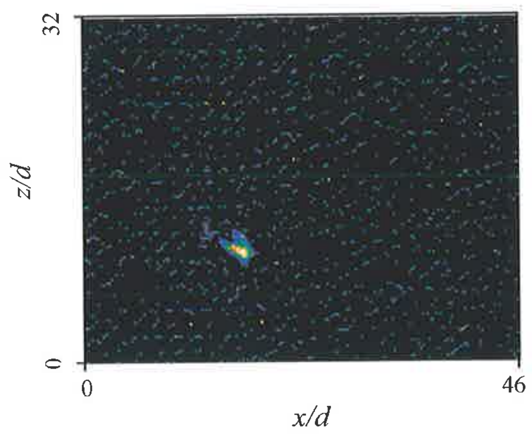

Appendix A-12

1. Experimental Conditions

$Re = 8840$; $St = 0.0061$; $f = 36\ Hz$; $P = 9.5\ kPa$; $U_0 = 29.20\ m\ s^{-1}$

2. Typical Images from the Zones of Soot Formation

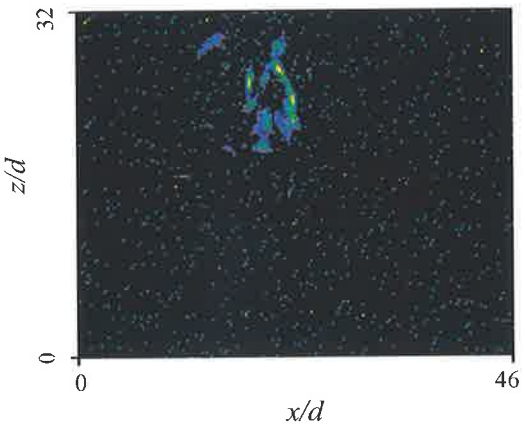

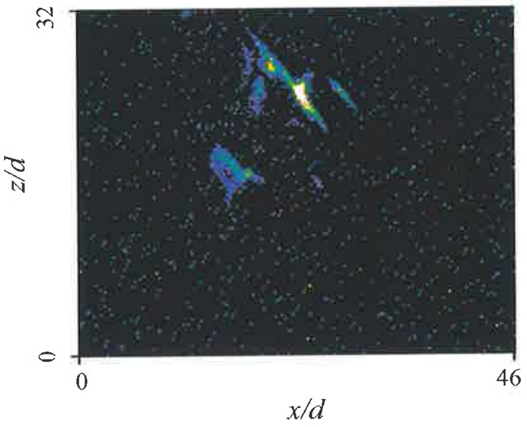

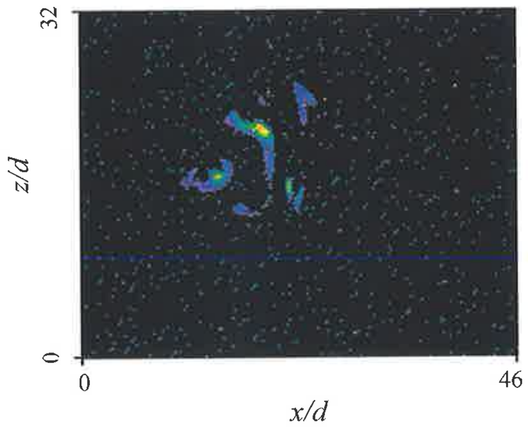

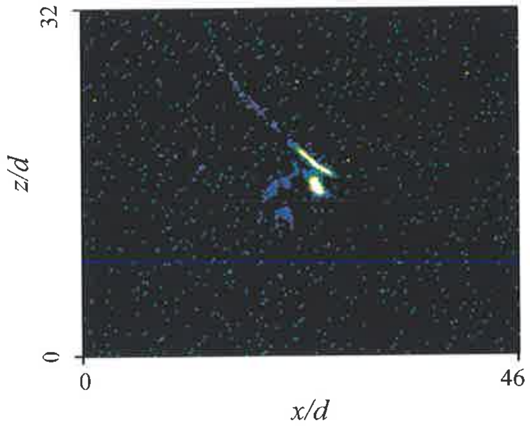

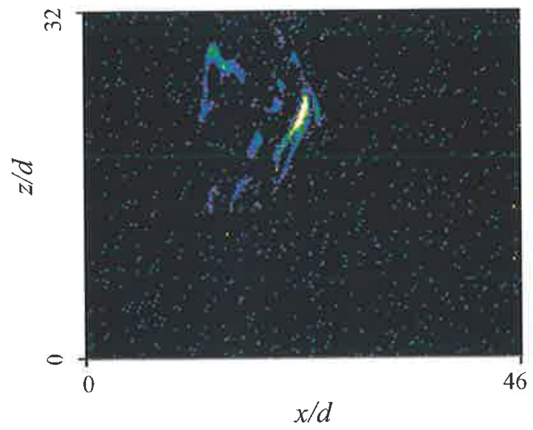

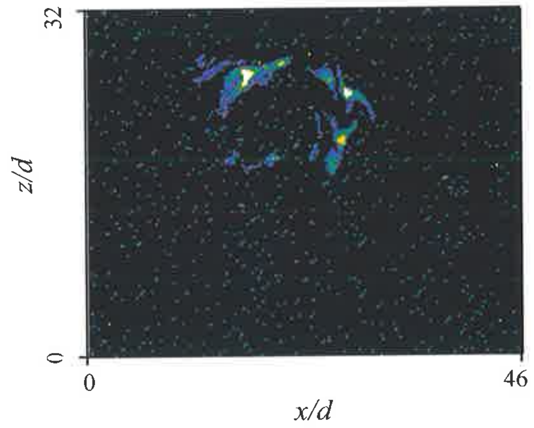

Appendix A-13

1. Experimental Conditions

$Re = 11223$; $St = 0.0061$; $f = 45\ Hz$; $P = 13\ kPa$; $U_0 = 37.08\ m\ s^{-1}$

2. Typical Images from the Zones of Soot Formation

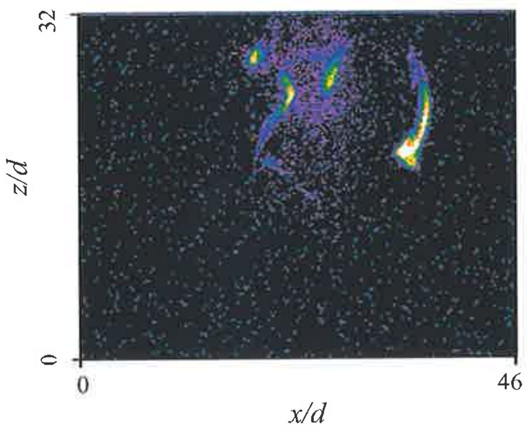

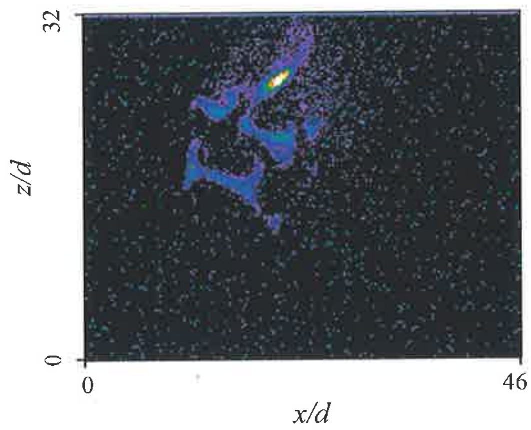

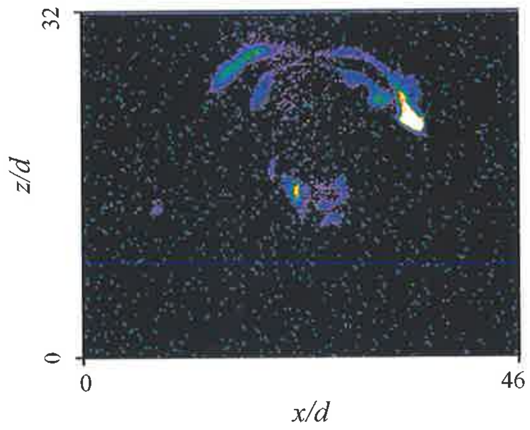

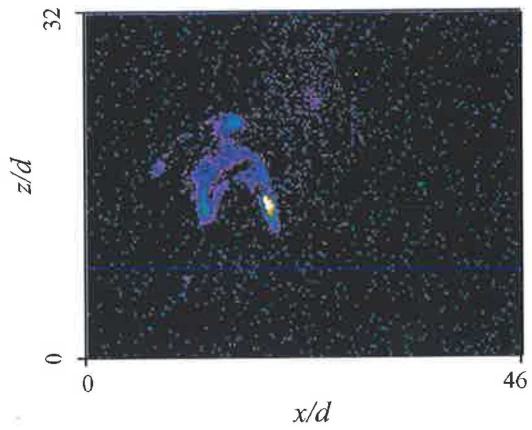

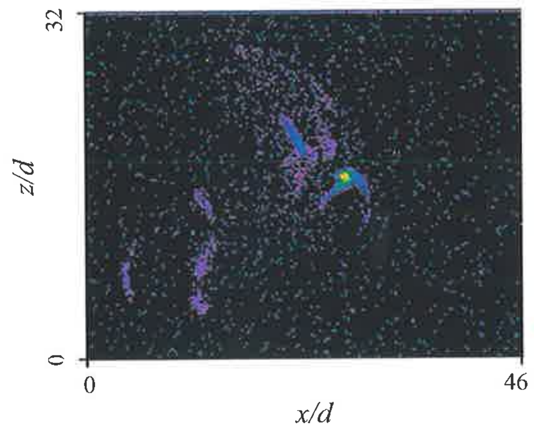

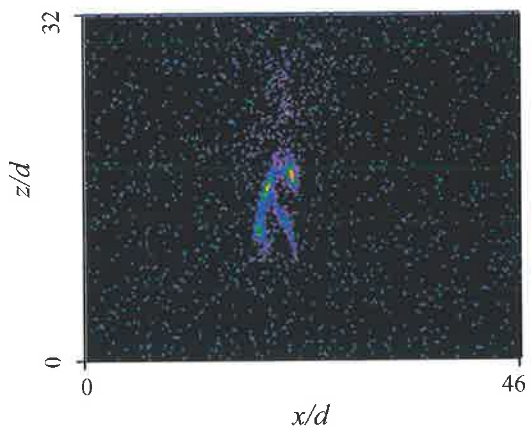

Appendix A-14

1. Experimental Conditions

$Re = 4329$; $St = 0.0069$; $f = 20\ Hz$; $P = 5\ kPa$; $U_0 = 14.30\ m\ s^{-1}$

2. Typical Images from the Zones of Soot Formation

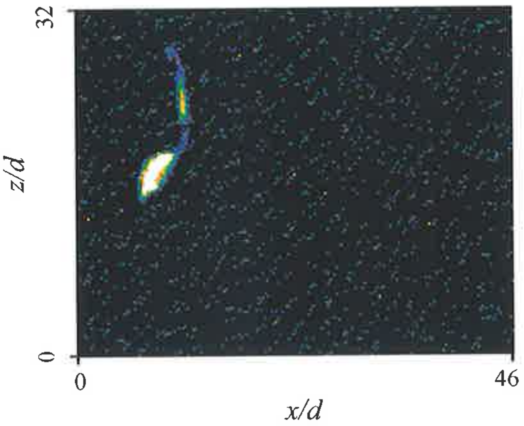

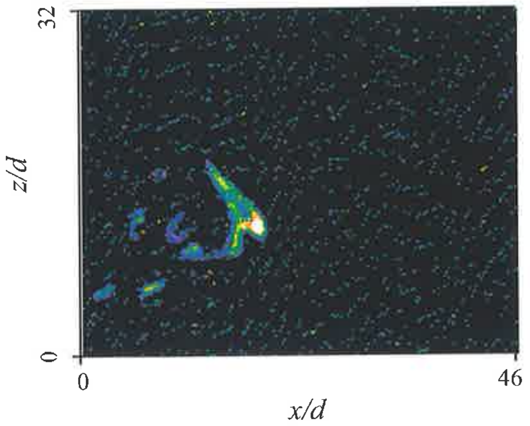

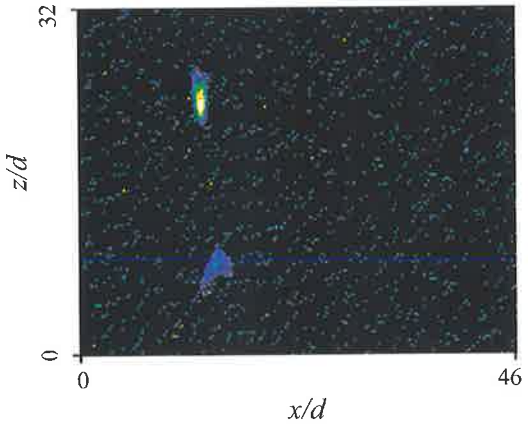

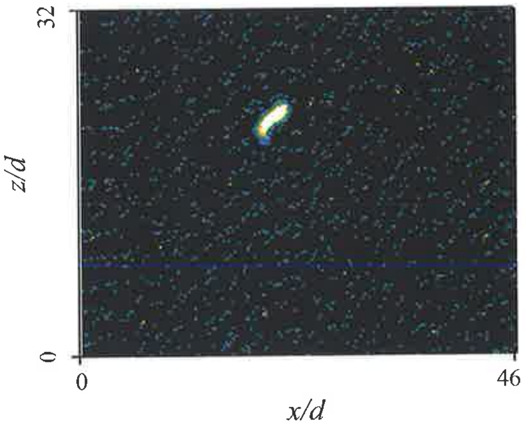

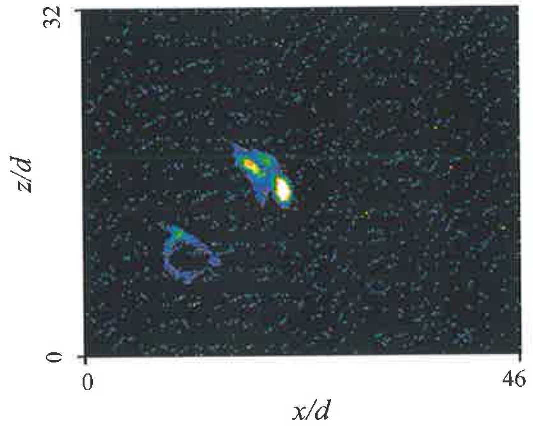

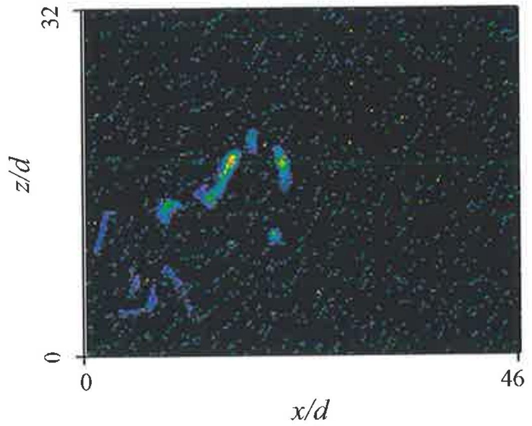

Appendix A-15

1. Experimental Conditions

$Re = 6555$; $St = 0.0069$; $f = 30\ Hz$; $P = 7\ kPa$; $U_0 = 21.66\ m\ s^{-1}$

2. Typical Images from the Zones of Soot Formation

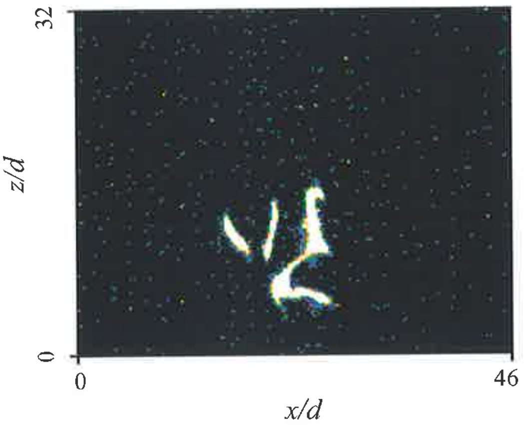

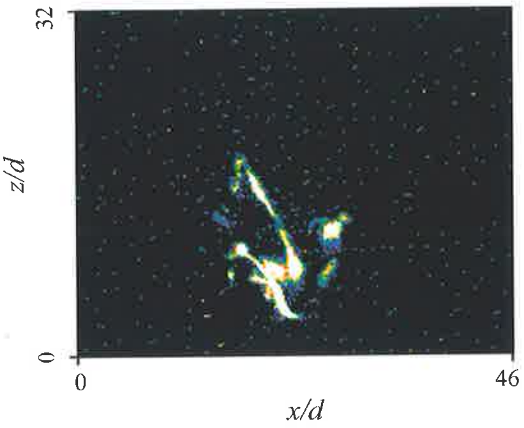

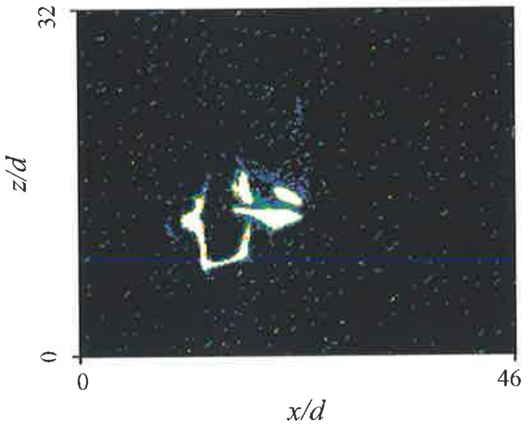

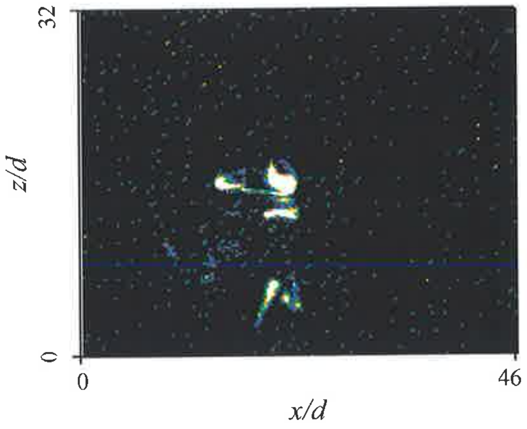

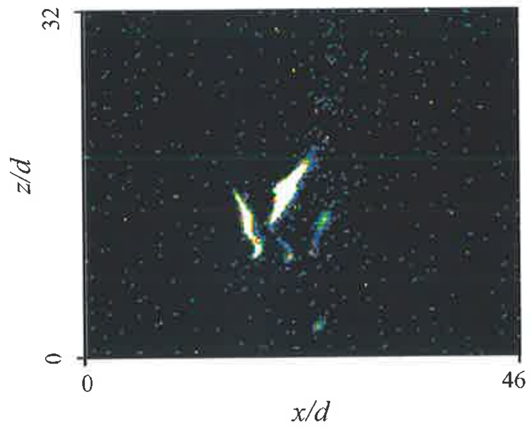

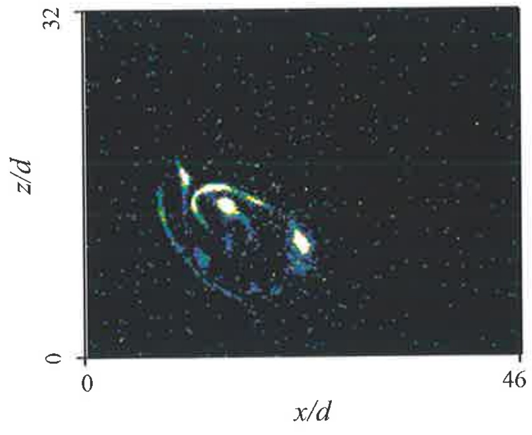

Appendix A-16

1. Experimental Conditions

$Re = 7682$; $St = 0.0069$; $f = 35\ Hz$; $P = 8\ kPa$; $U_0 = 25.39\ m\ s^{-1}$

2. Typical Images from the Zones of Soot Formation

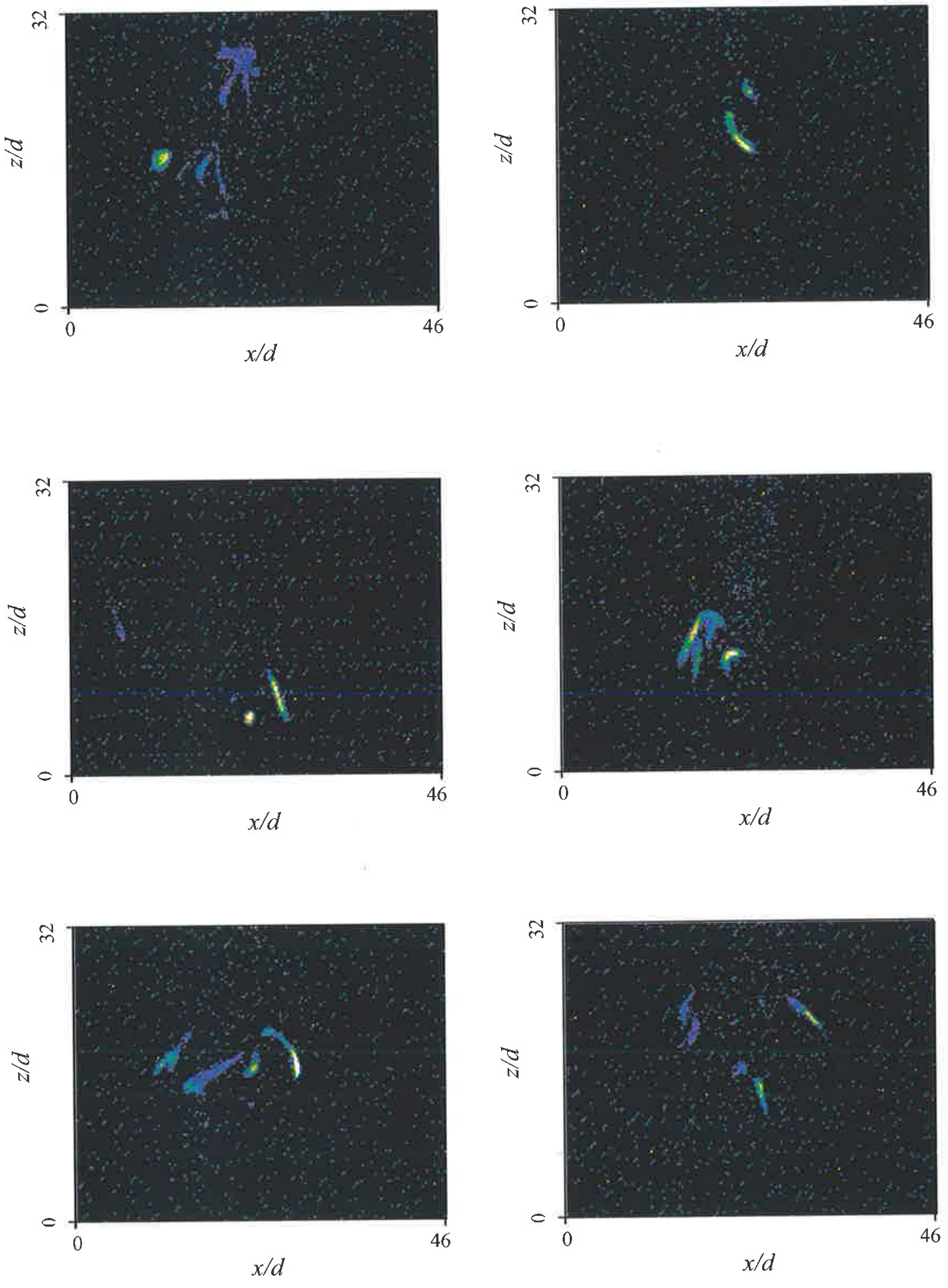

Appendix A-17

1. Experimental Conditions

$Re = 8840$; $St = 0.0069$; $f = 40\ Hz$; $P = 9.5\ kPa$; $U_0 = 29.20\ m\ s^{-1}$

2. Typical Images from the Zones of Soot Formation

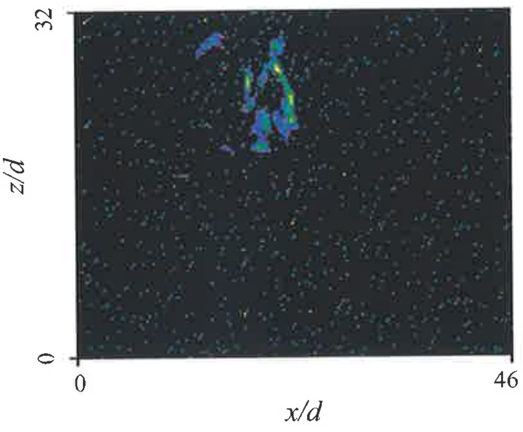

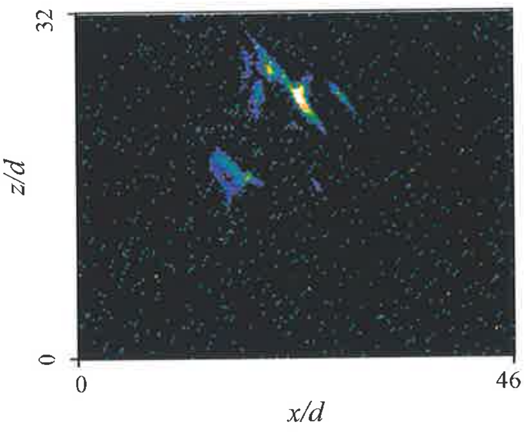

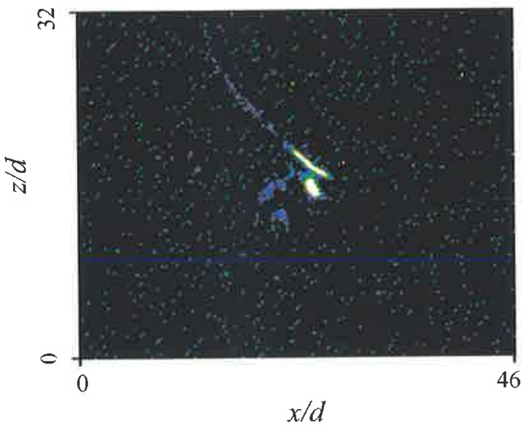

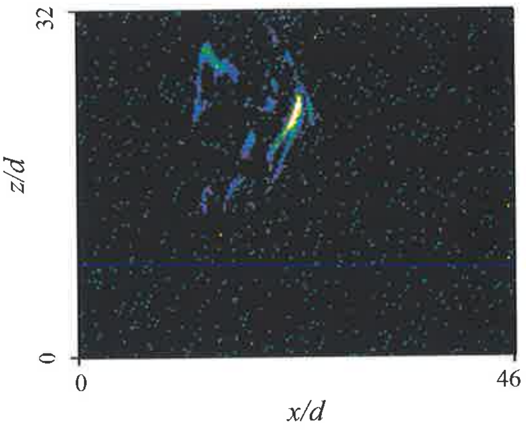

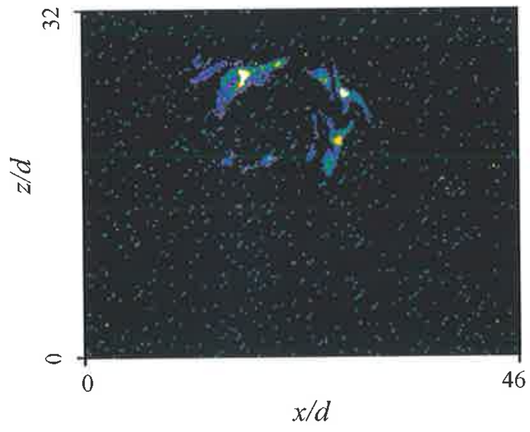

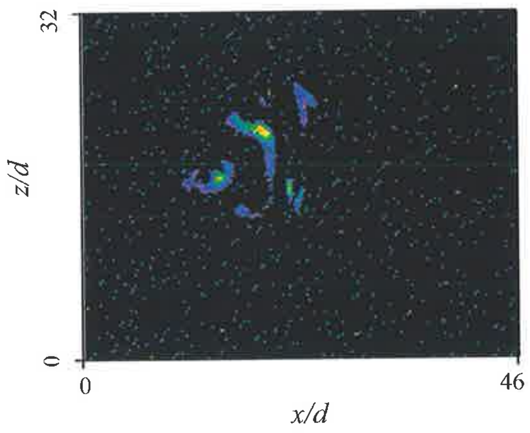

Appendix A-18

1. Experimental Conditions

$Re = 11223$; $St = 0.0069$; $f = 51.8.2\ Hz$; $P = 13\ kPa$; $U_0 = 37.08\ m\ s^{-1}$

2. Typical Images from the Zones of Soot Formation

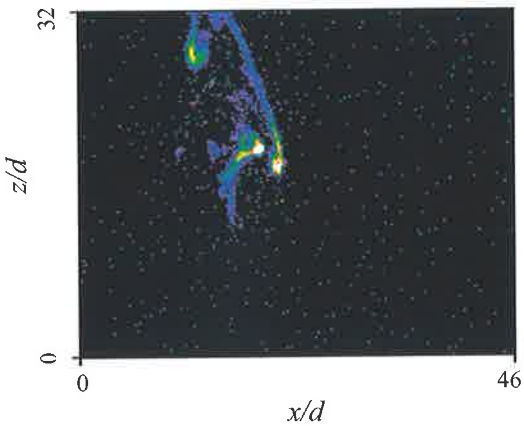

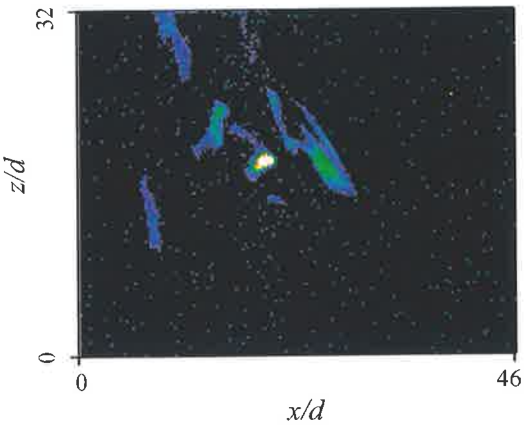

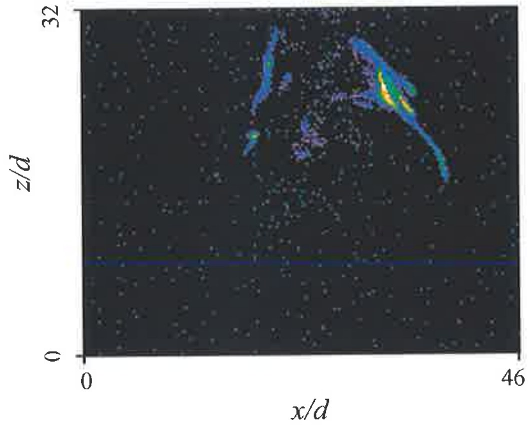

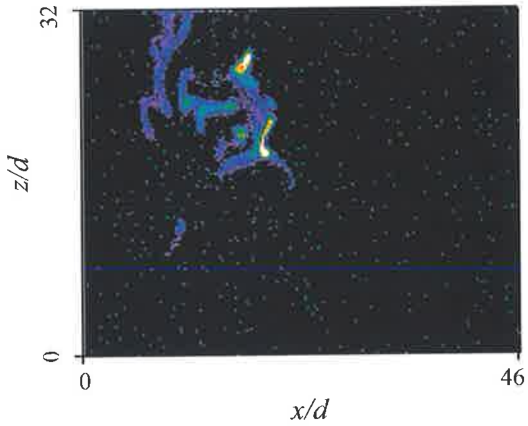

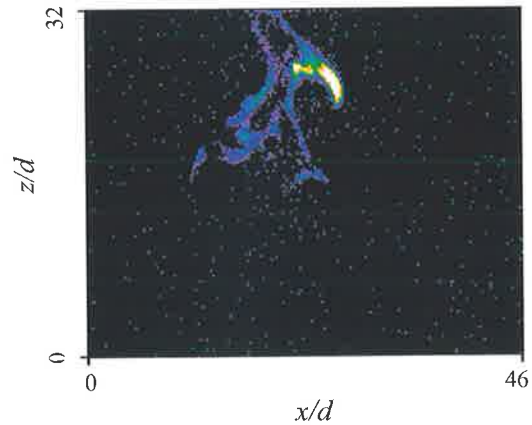

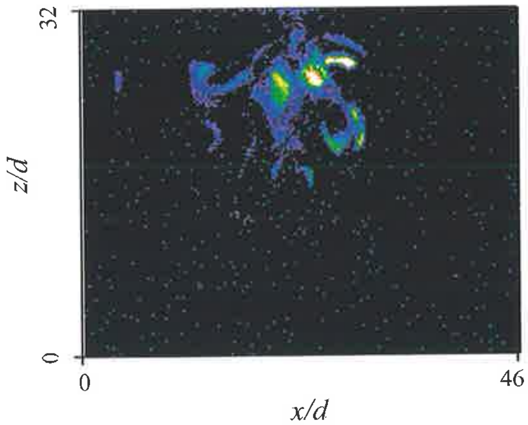

Appendix A-19

1. Experimental Conditions

$Re = 4329$; $St = 0.0083$; $f = 24.2\ Hz$; $P = 5\ kPa$; $U_0 = 14.30\ m\ s^{-1}$

2. Typical Images from the Zones of Soot Formation

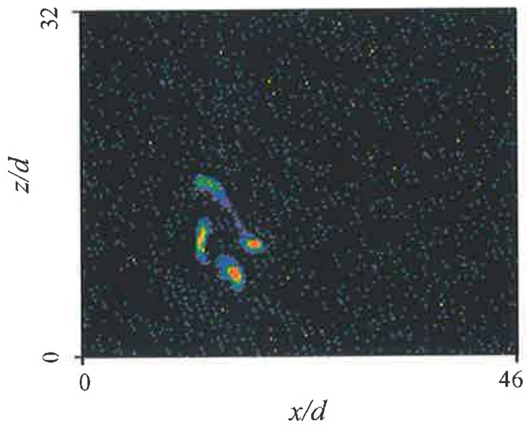

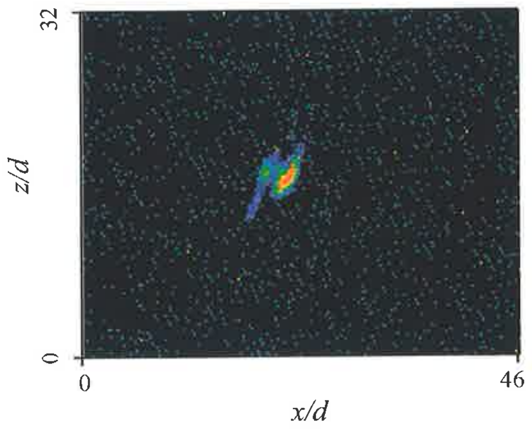

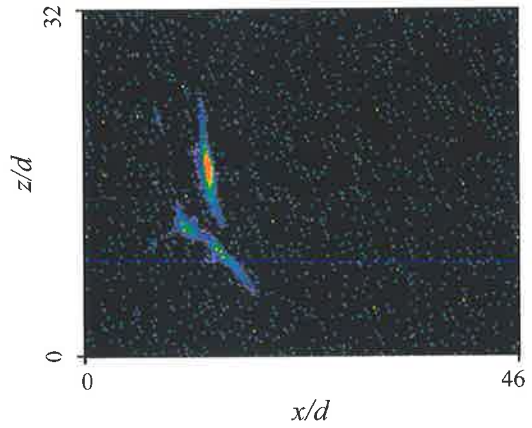

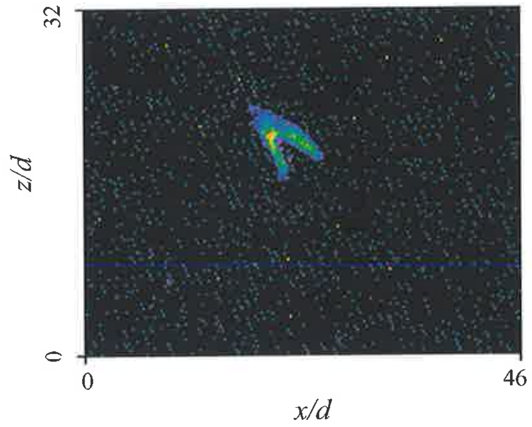

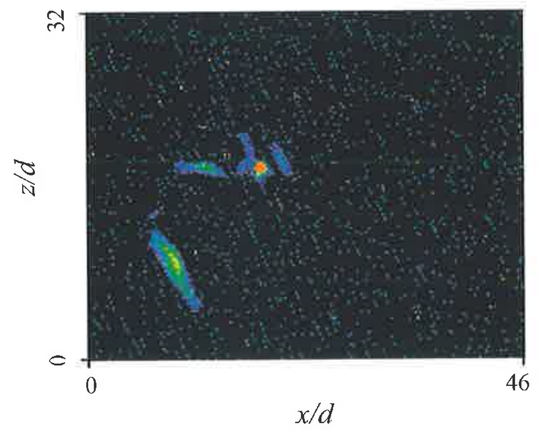

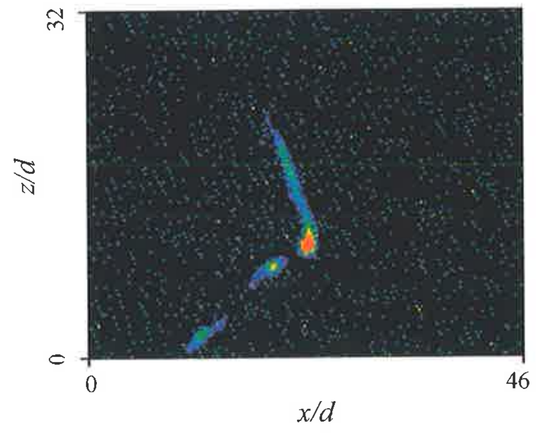

Appendix A-20

1. Experimental Conditions

$Re = 5437$; $St = 0.0083$; $f = 30\ Hz$; $P = 6\ kPa$; $U_0 = 17.96\ m\ s^{-1}$

2. Typical Images from the Zones of Soot Formation

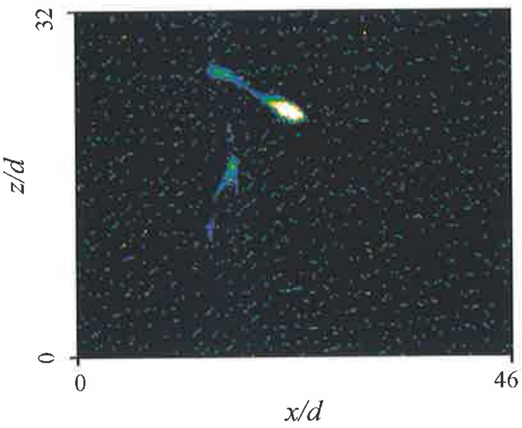

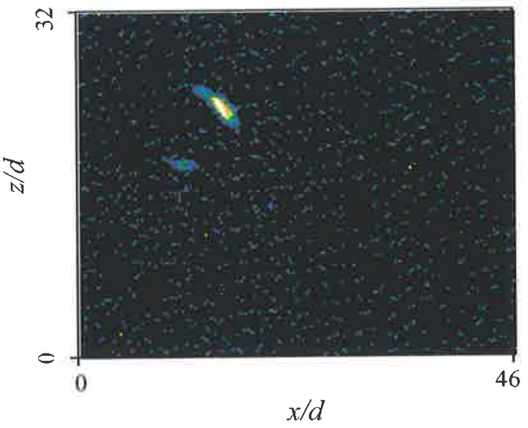

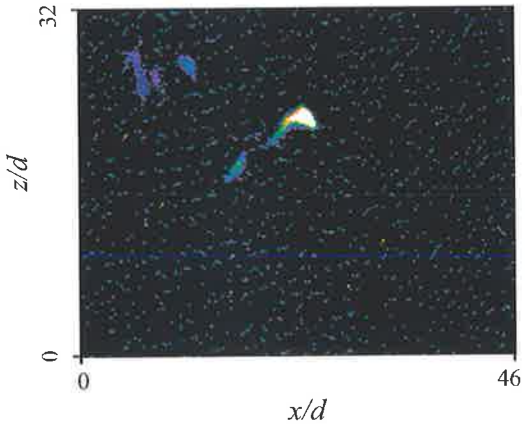

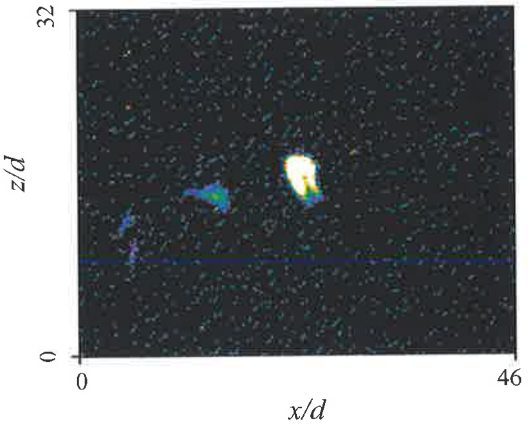

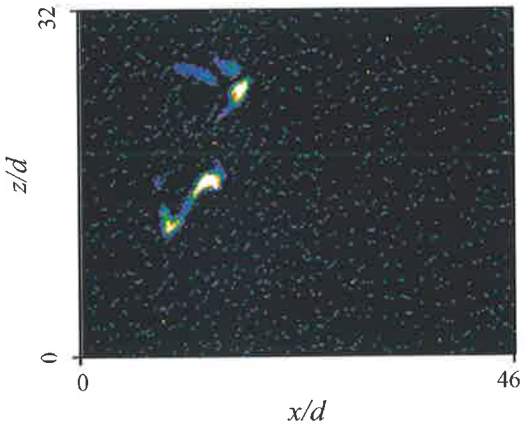

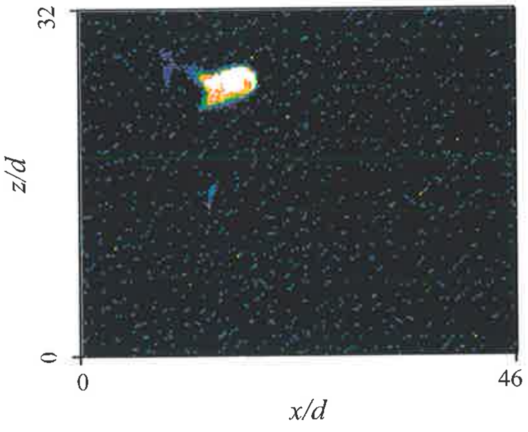

Appendix A-21

1. Experimental Conditions

$Re = 6555$; $St = 0.0083$; $f = 36.3\ Hz$; $P = 7\ kPa$; $U_0 = 21.65\ m\,s^{-1}$

2. Typical Images from the Zones of Soot Formation

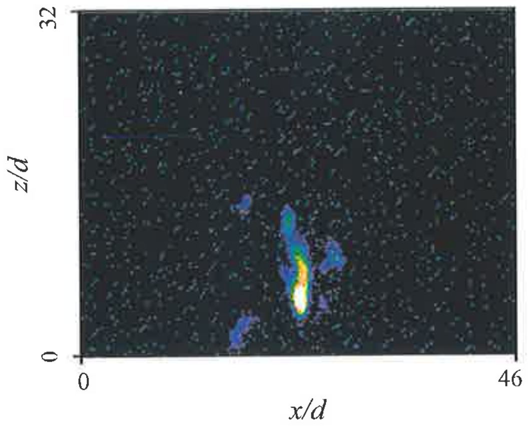

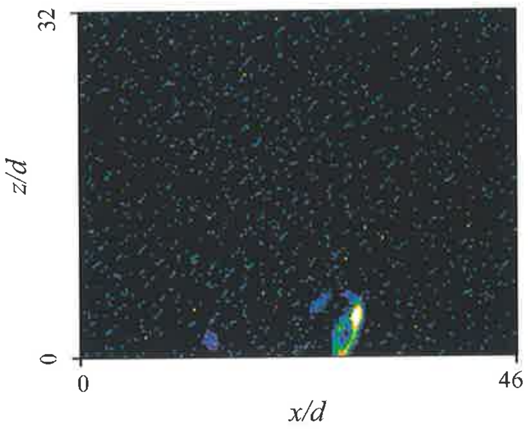

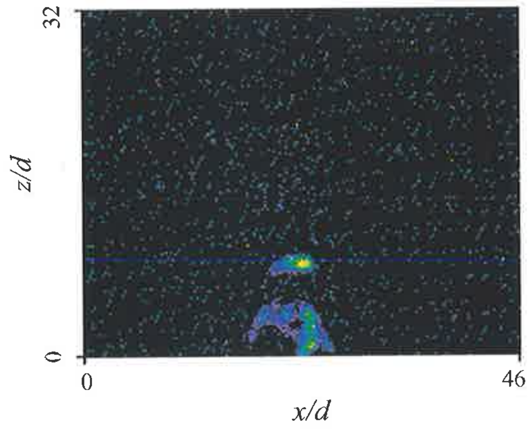

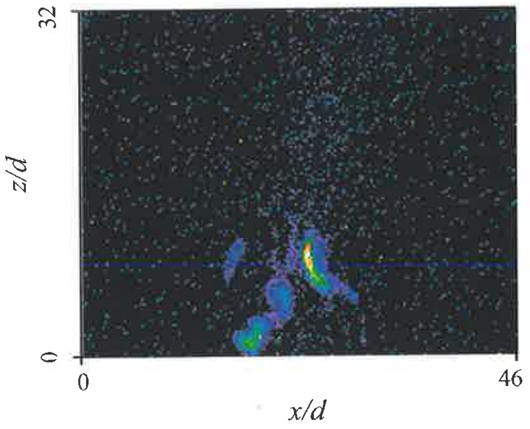

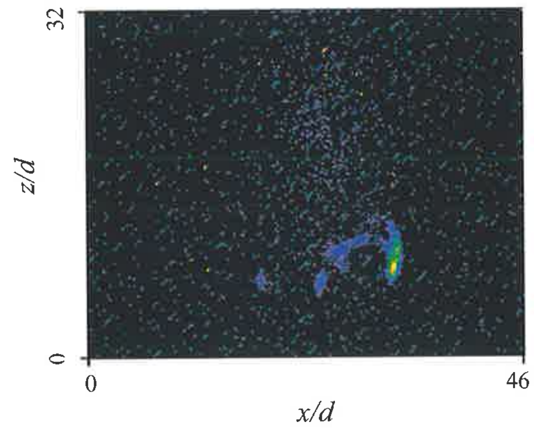

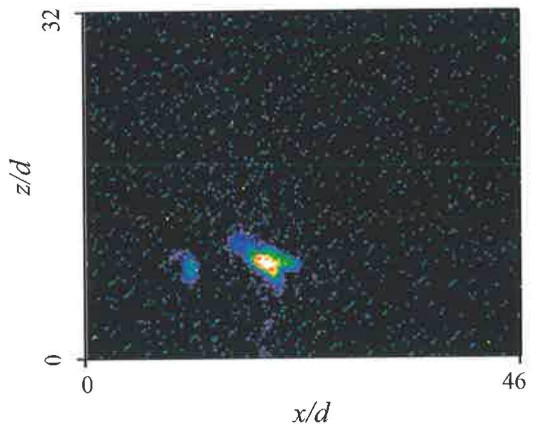

Appendix A-22

1. Experimental Conditions

$Re = 7682$; $St = 0.0083$; $f = 42.3\ Hz$; $P = 8\ kPa$; $U_0 = 25.38\ m\ s^{-1}$

2. Typical Images from the Zones of Soot Formation

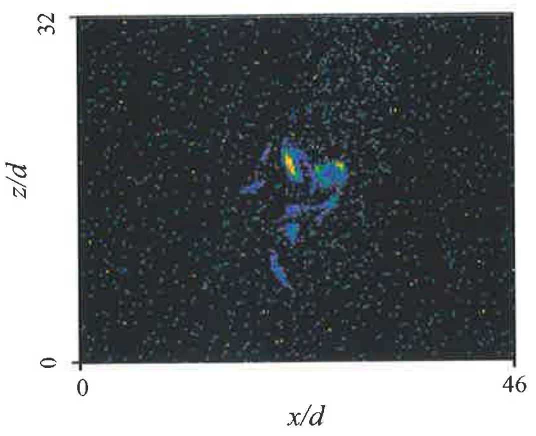

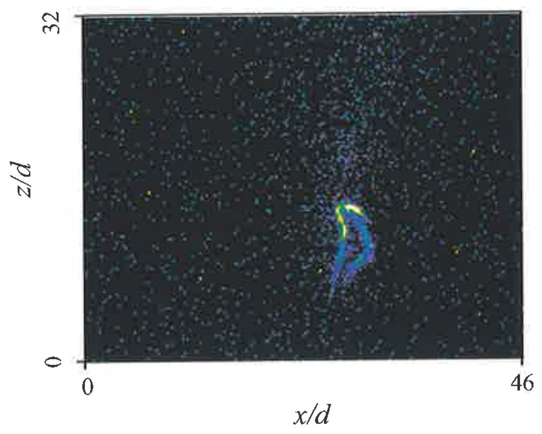

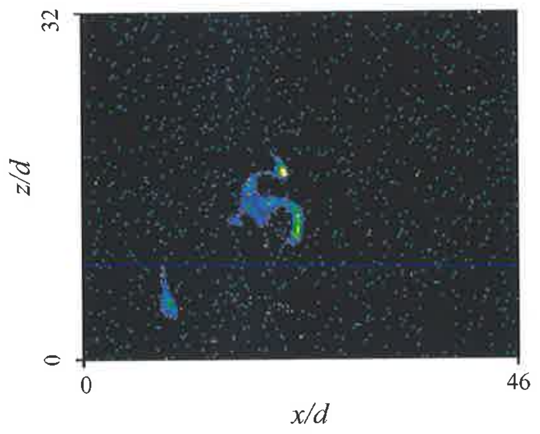

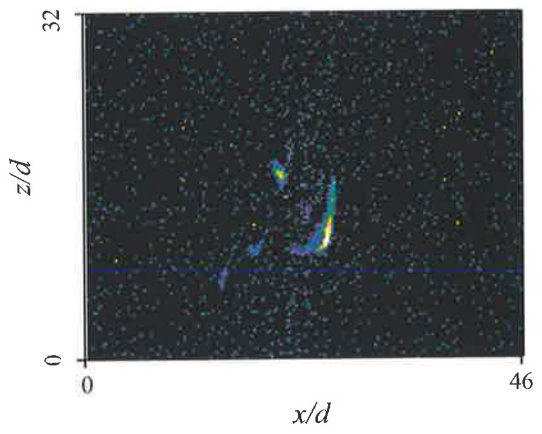

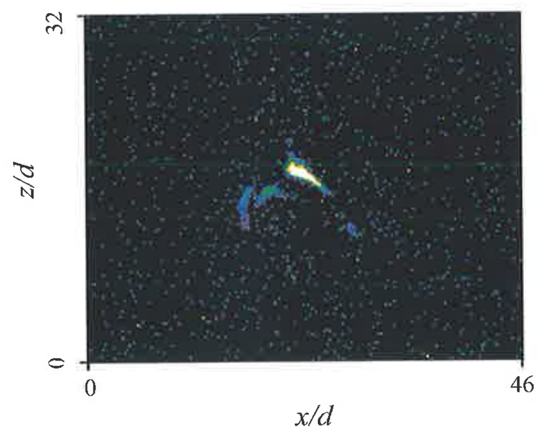

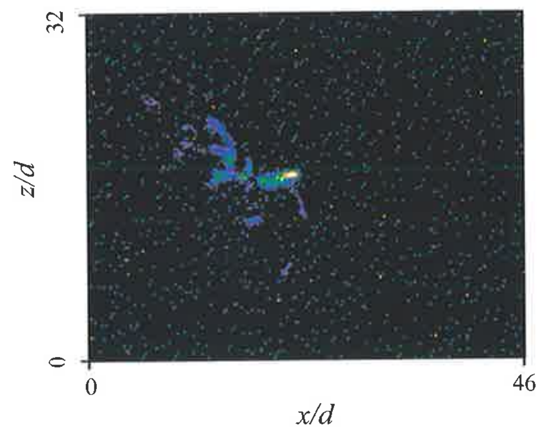

Appendix A-23

1. Experimental Conditions

$Re = 8840$; $St = 0.0083$; $f = 48.4\ Hz$; $P = 8\ kPa$; $U_0 = 29.20\ m\ s^{-1}$

2. Typical Images from the Zones of Soot Formation

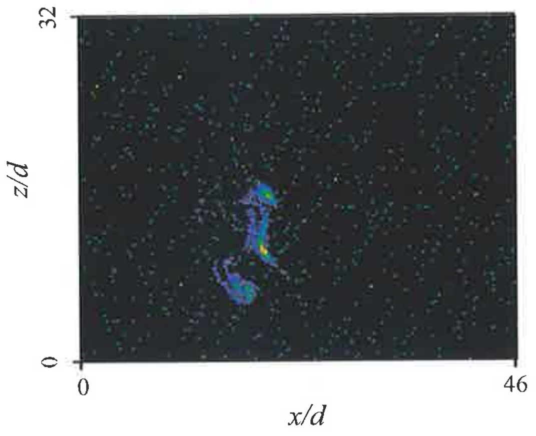

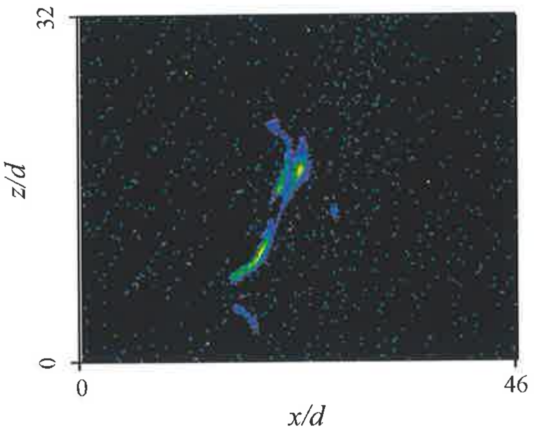

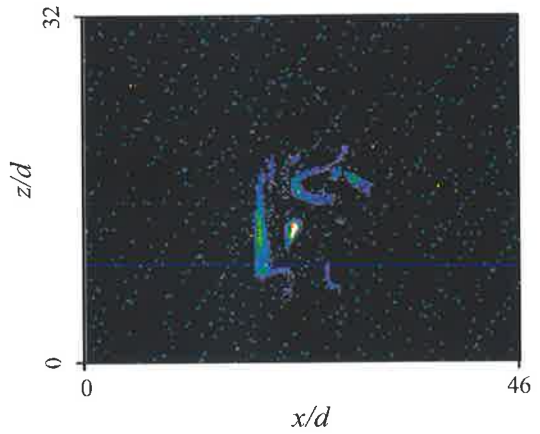

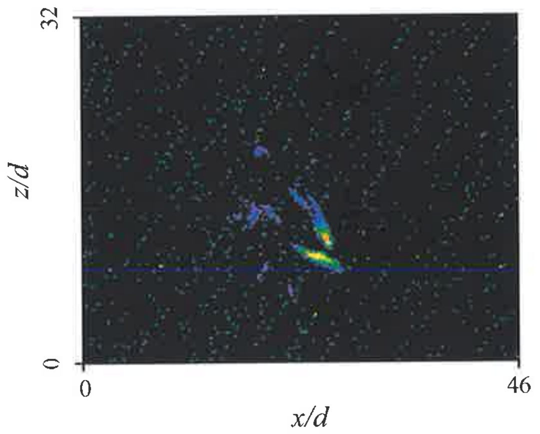

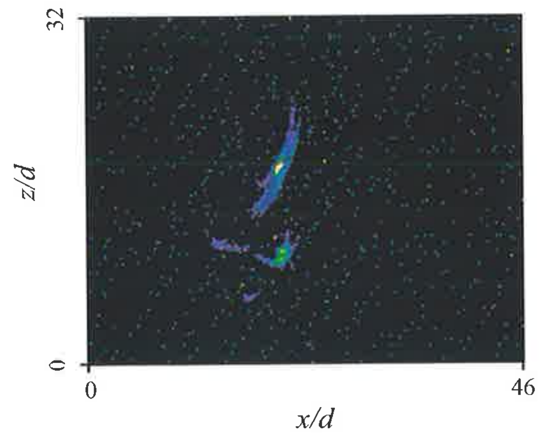

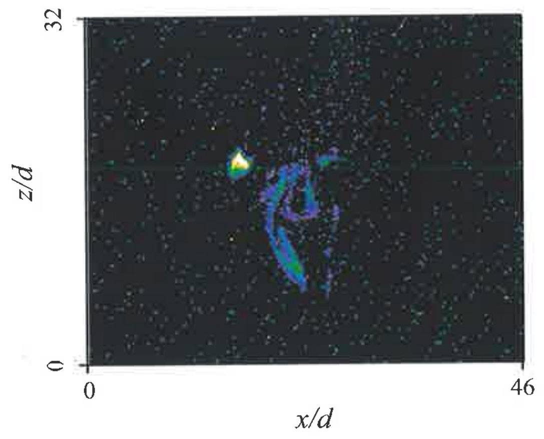

Appendix A-24

1. Experimental Conditions

$Re = 10012$; $St = 0.0083$; $f = 54.4.3\ Hz$; $P = 11\ kPa$; $U_0 = 33.08\ m\ s^{-1}$

2. Typical Images from the Zones of Soot Formation

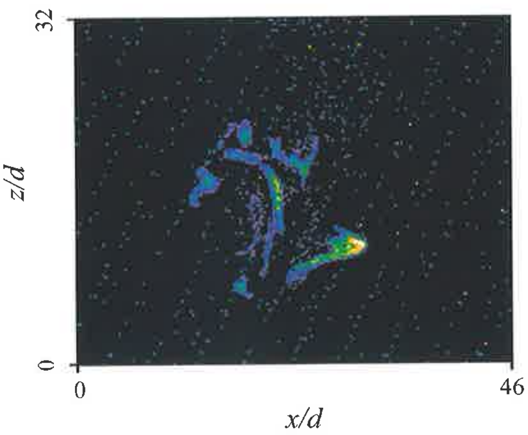

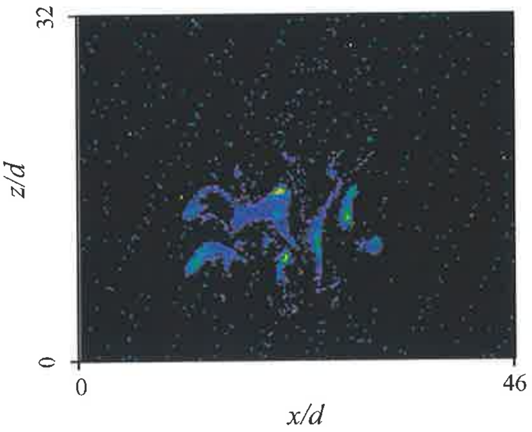

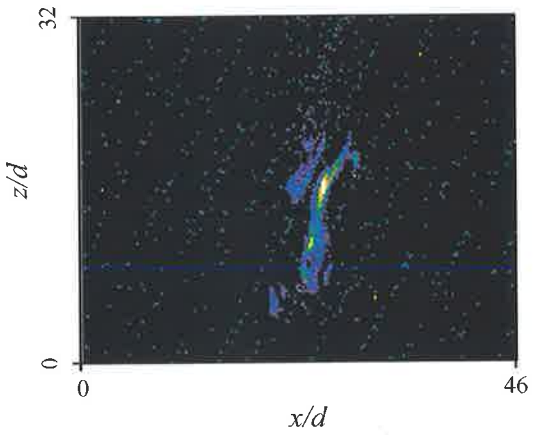

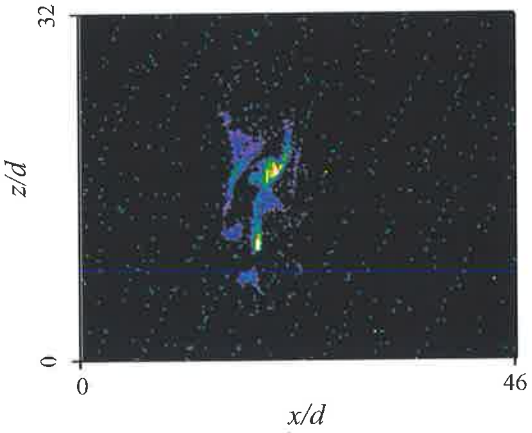

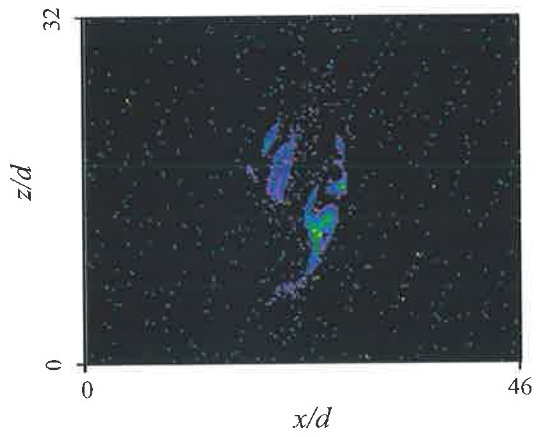

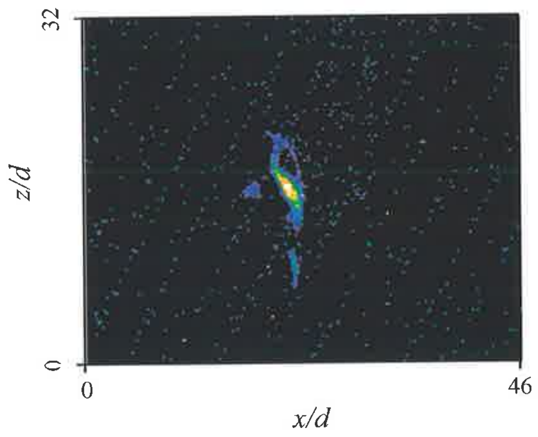

Appendix A-25

1. Experimental Conditions

$Re = 11223$; $St = 0.0083$; $f = 60.5\ Hz$; $P = 13\ kPa$; $U_0 = 37.08\ m\ s^{-1}$

2. Typical Images from the Zones of Soot Formation

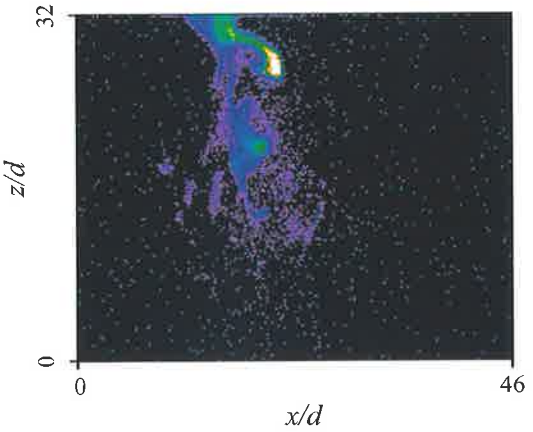

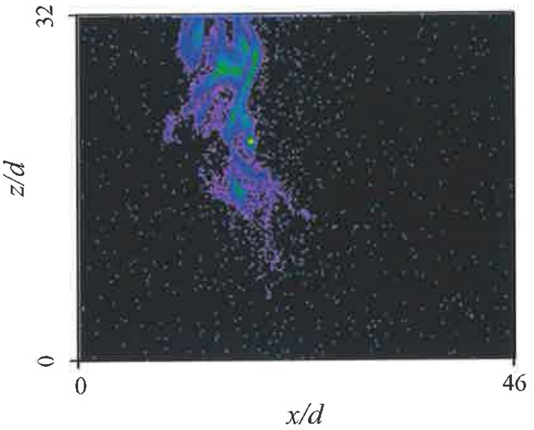

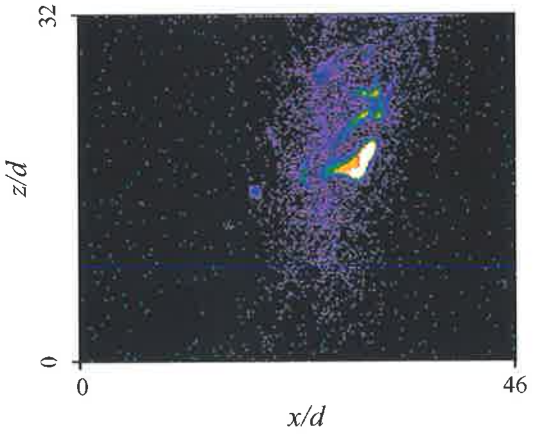

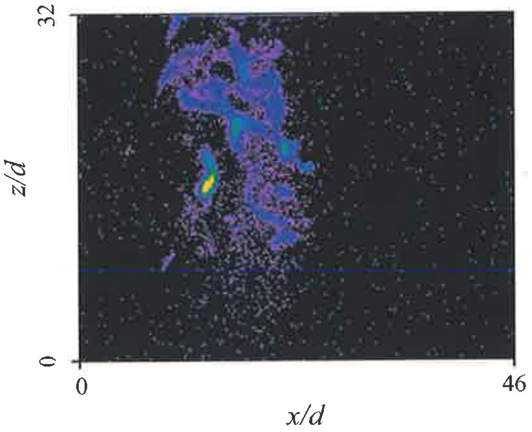

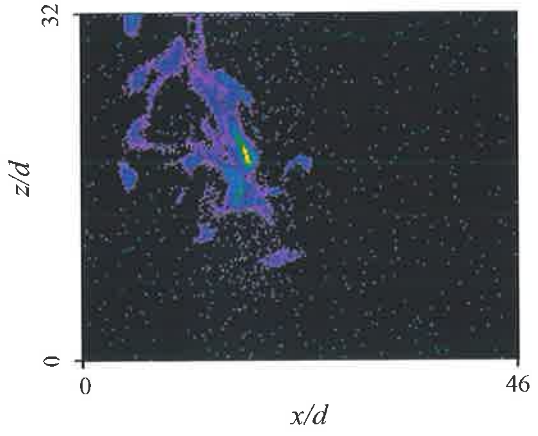

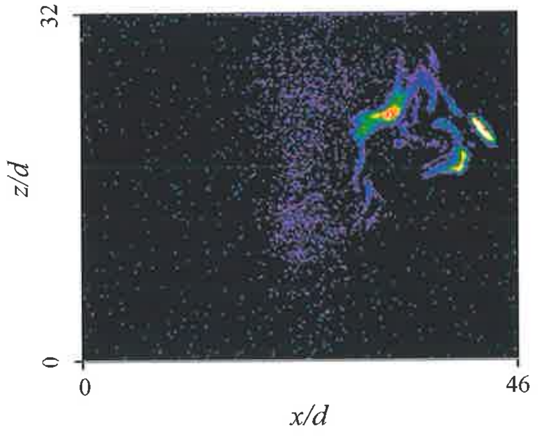

Appendix A-26

1. Experimental Conditions

$Re = 4329$; $St = 0.0091$; $f = 26.4\ Hz$; $P = 5\ kPa$; $U_0 = 14.30\ m\,s^{-1}$

2. Typical Images from the Zones of Soot Formation

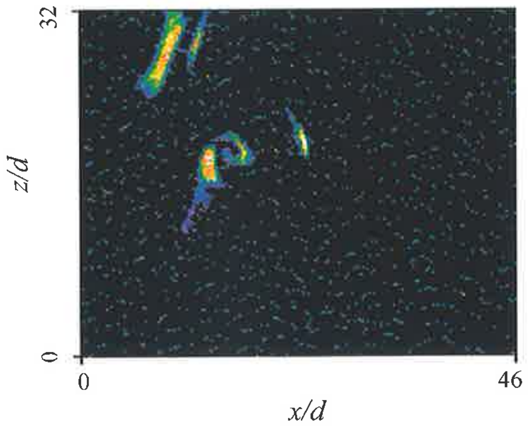

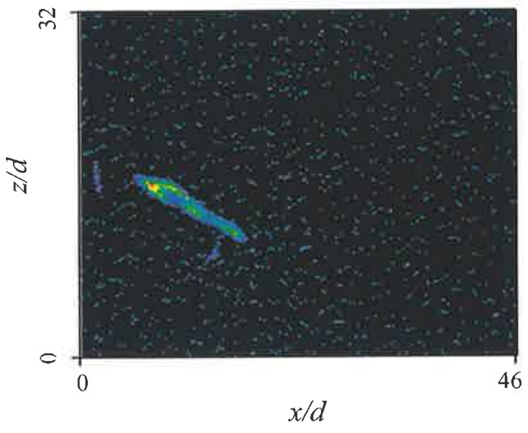

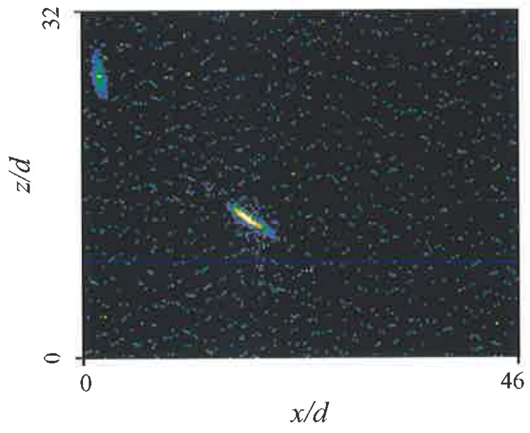

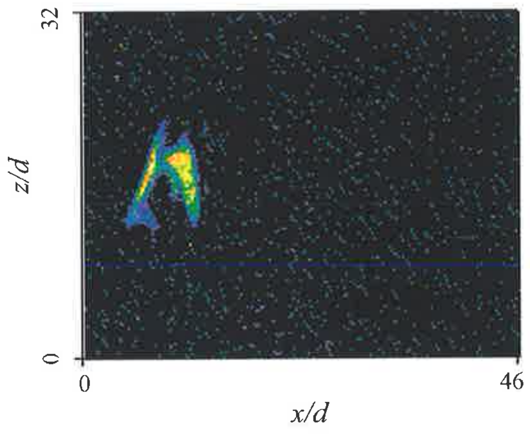

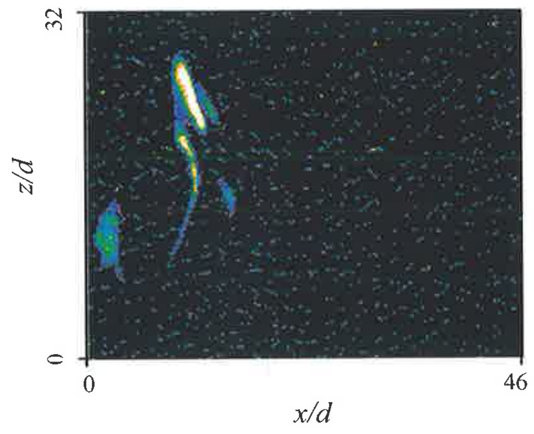

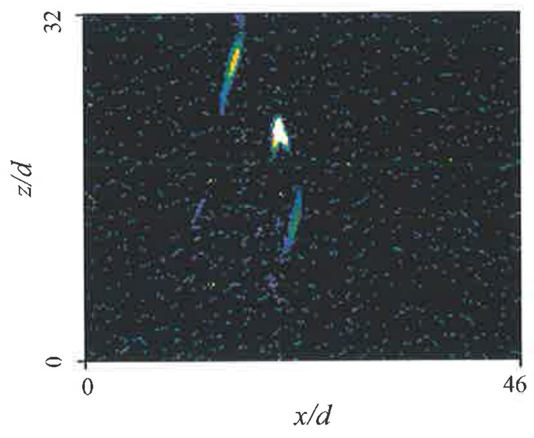

Appendix A-27

1. Experimental Conditions

$Re = 5437$; $St = 0.0091$; $f = 33\ Hz$; $P = 6\ kPa$; $U_0 = 17.96\ m\ s^{-1}$

2. Typical Images from the Zones of Soot Formation

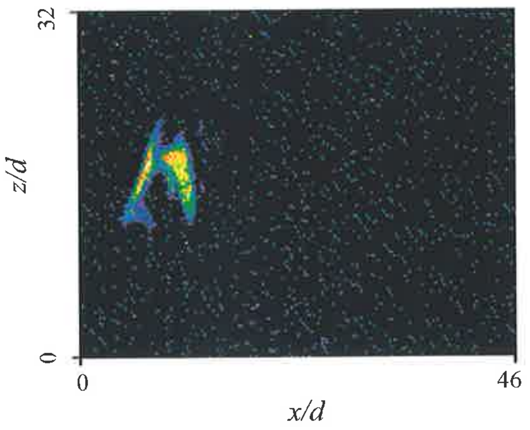

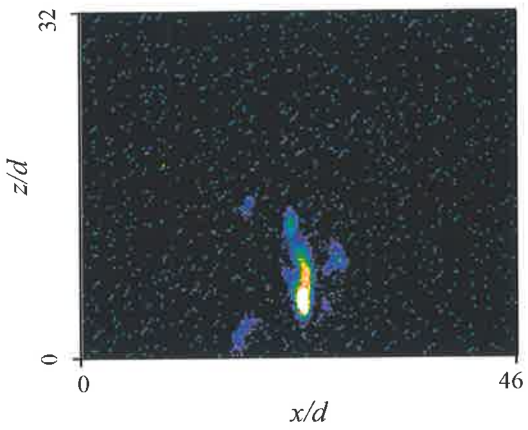

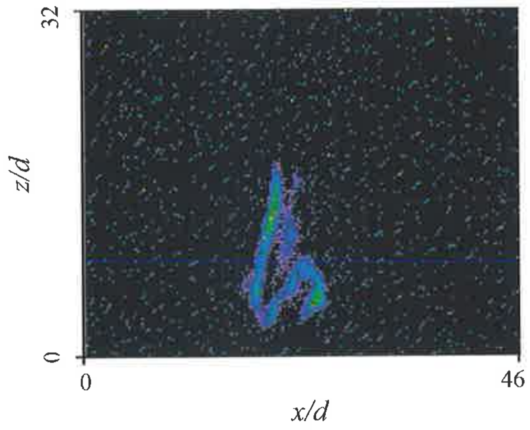

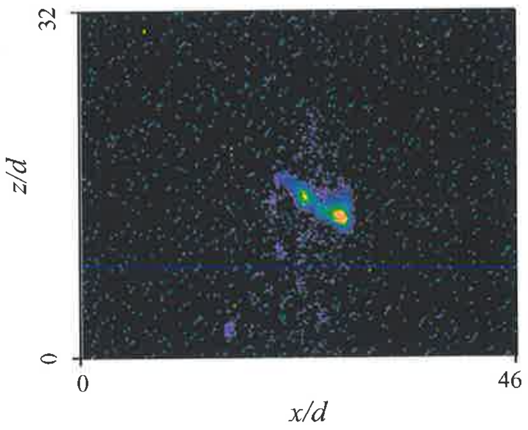

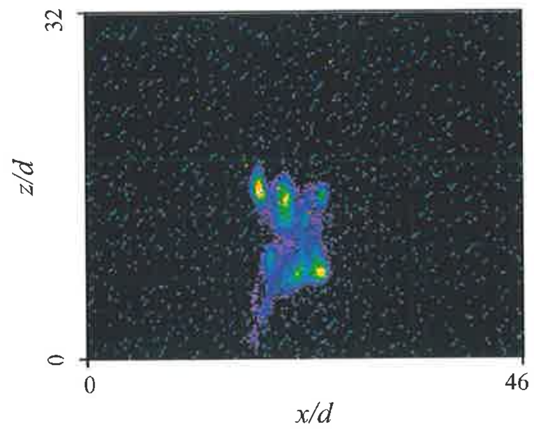

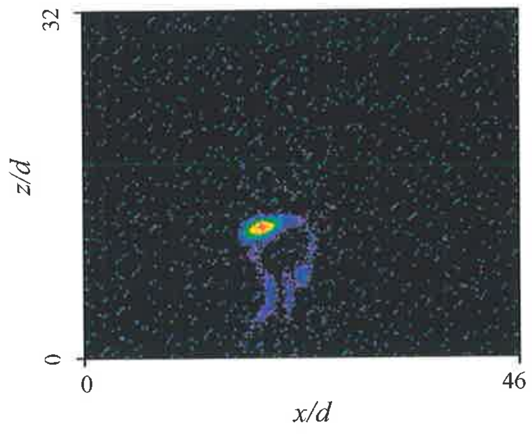

Appendix A-28

1. Experimental Conditions

$Re = 6555$; $St = 0.0091$; $f = 40\ Hz$; $P = 7\ kPa$; $U_0 = 21.65\ m\ s^{-1}$

2. Typical Images from the Zones of Soot Formation

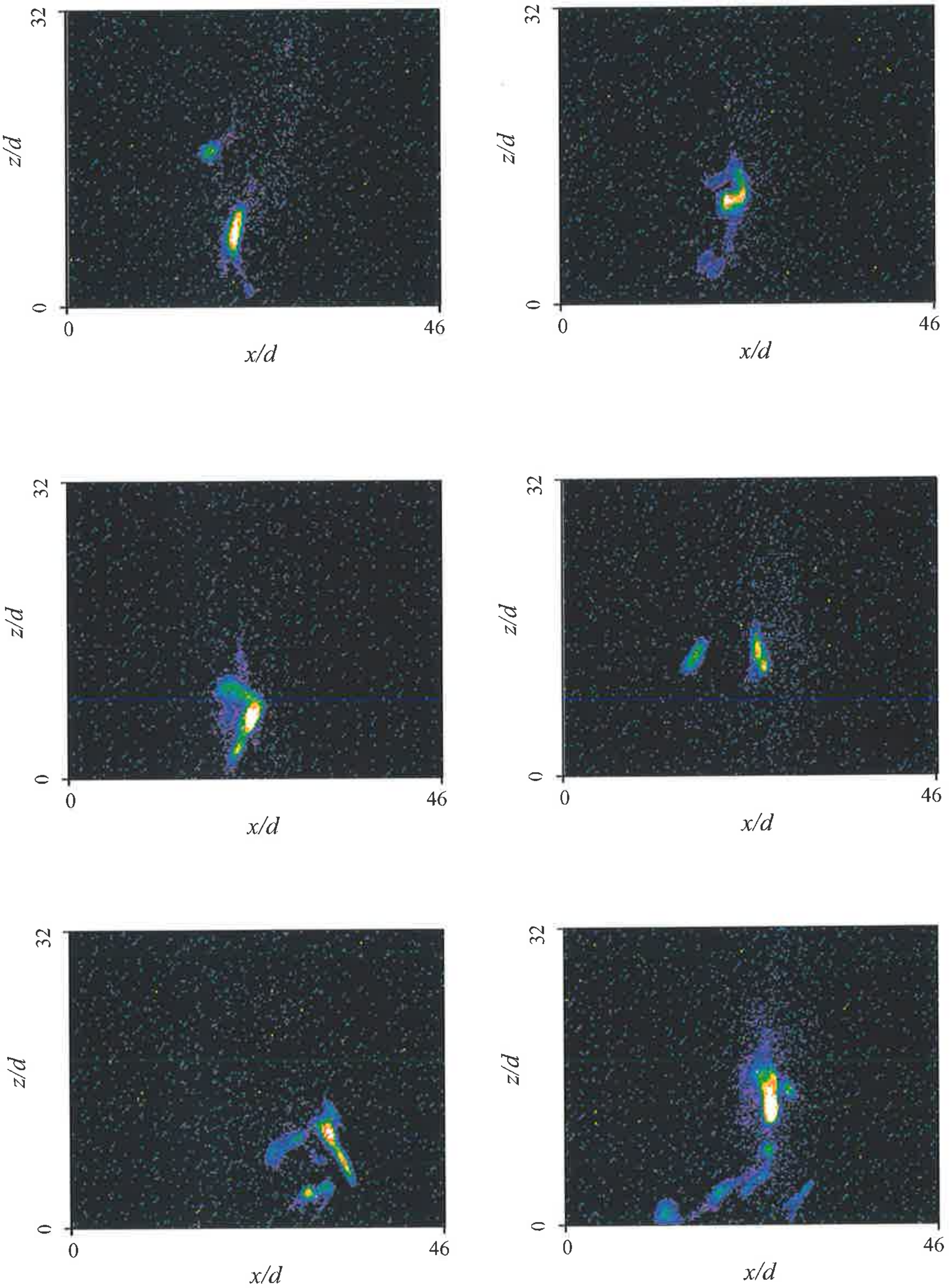

Appendix A-29

1. Experimental Conditions

$Re = 7682$; $St = 0.0091$; $f = 46.6\ Hz$; $P = 8\ kPa$; $U_0 = 25.38\ m\ s^{-1}$

2. Typical Images from the Zones of Soot Formation

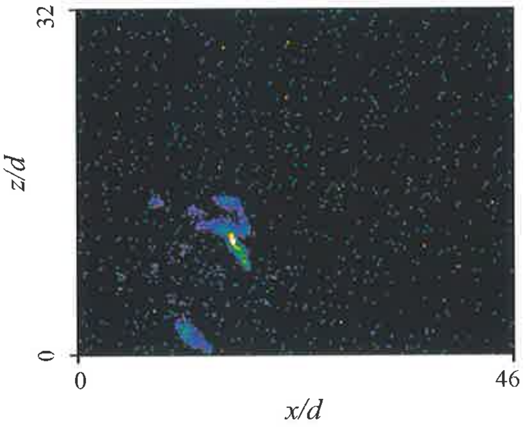

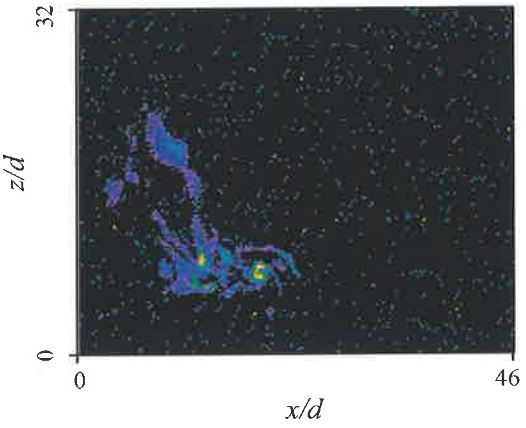

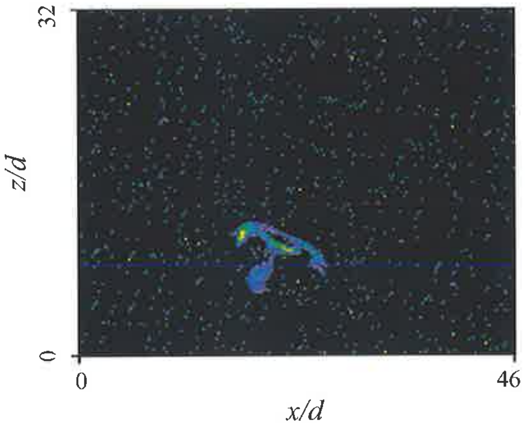

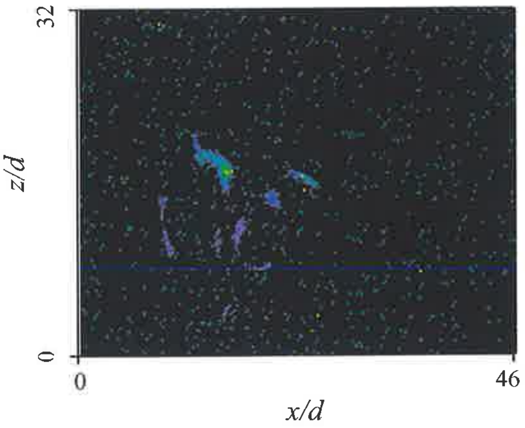

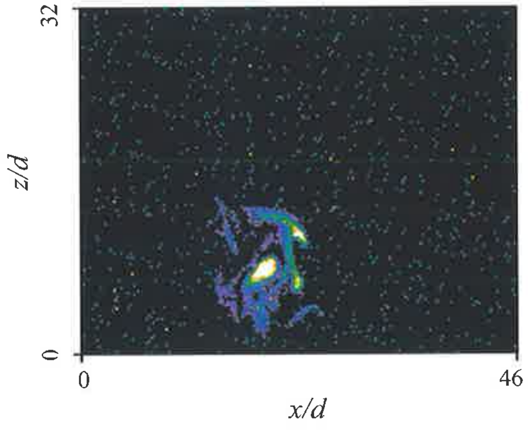

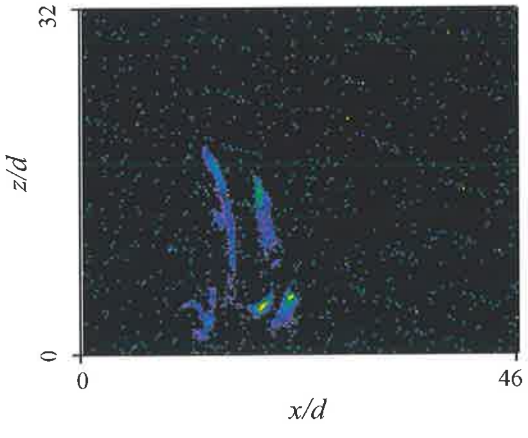

Appendix A-30

1. Experimental Conditions

$Re = 8840$; $St = 0.0091$; $f = 53.3\ Hz$; $P = 9.5\ kPa$; $U_0 = 29.20\ m\ s^{-1}$

2. Typical Images from the Zones of Soot Formation

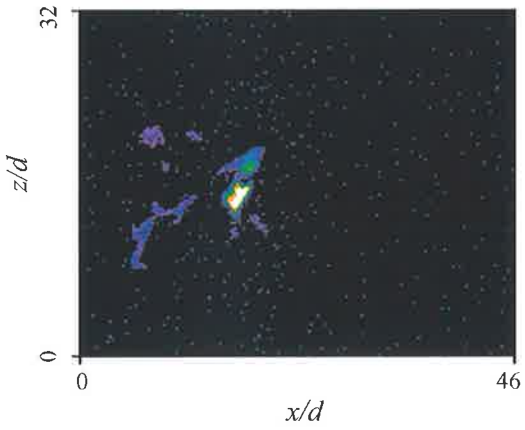

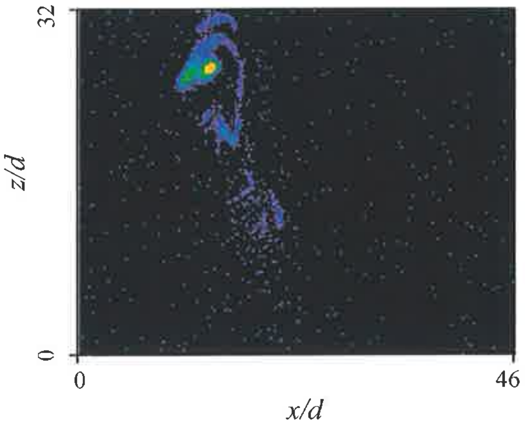

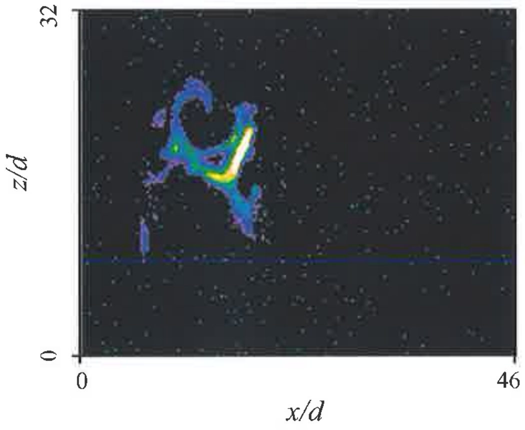

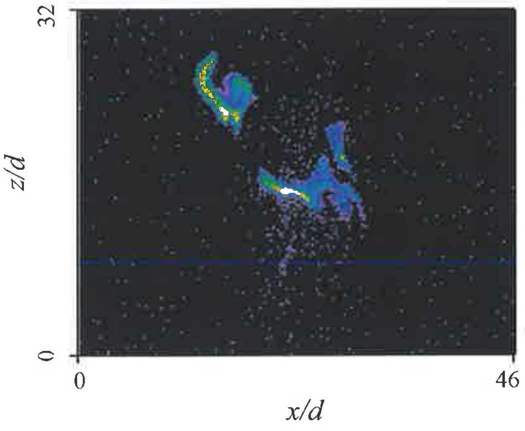

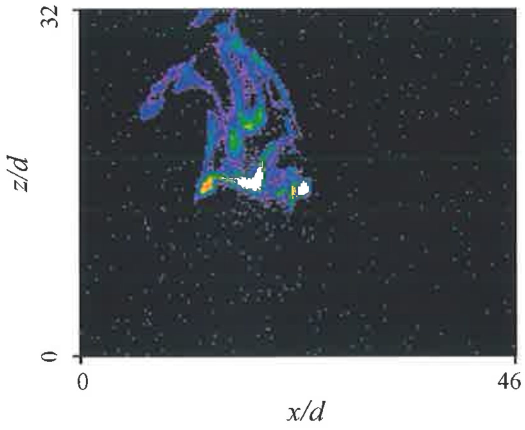

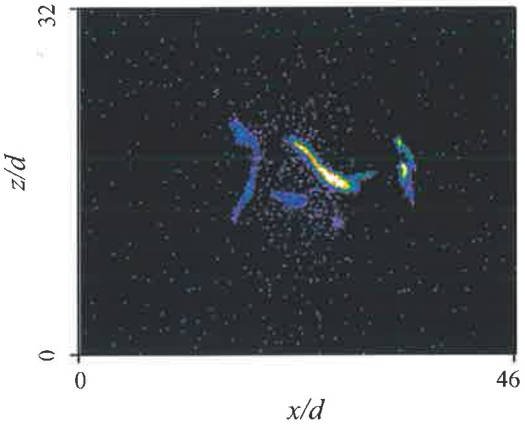

Appendix A-31

1. Experimental Conditions

$Re = 10012$; $St = 0.0091$; $f = 60\ Hz$; $P = 11\ kPa$; $U_0 = 33.08\ m\ s^{-1}$

2. Typical Images from the Zones of Soot Formation

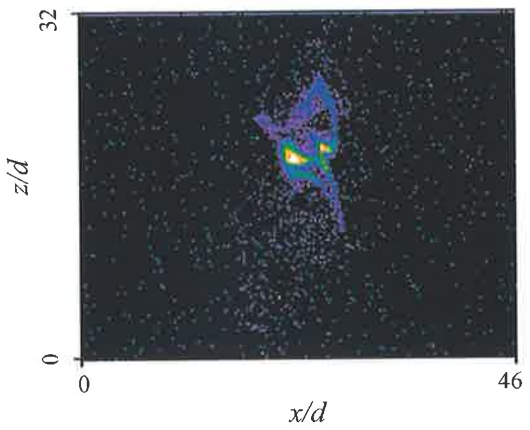

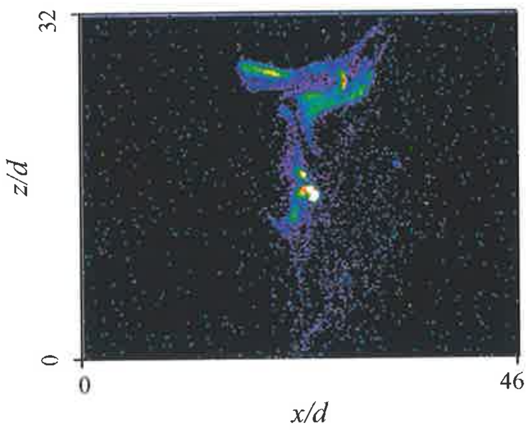

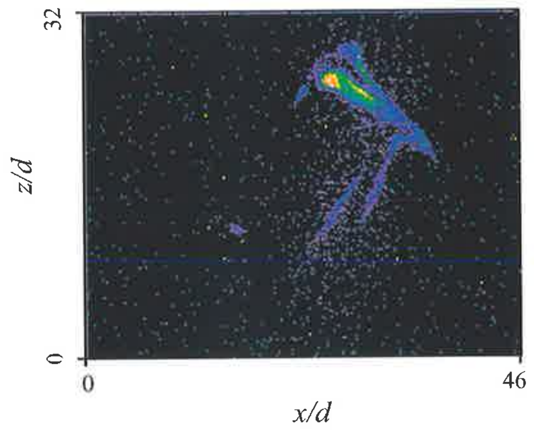

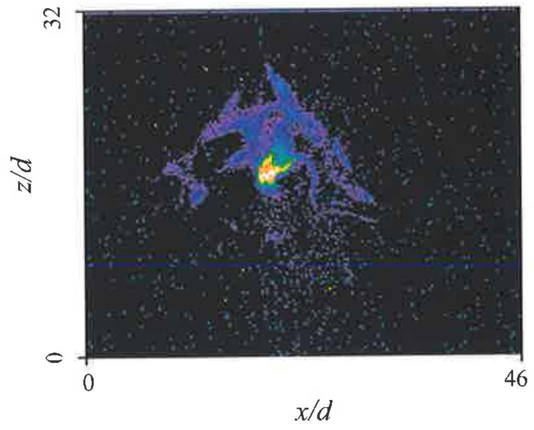

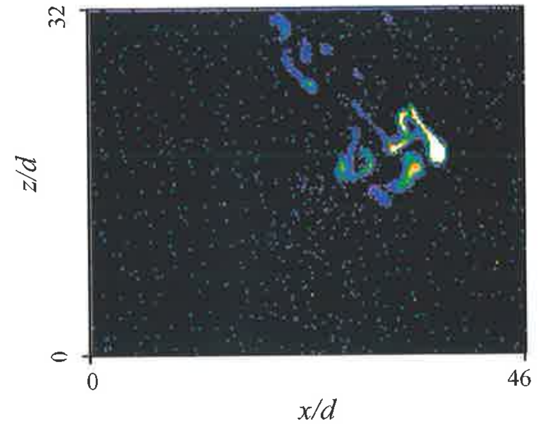

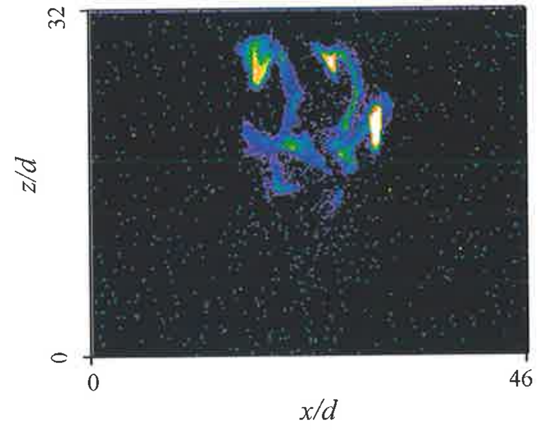

Appendix A-32

1. Experimental Conditions

$Re = 11223$; $St = 0.0091$; $f = 66\ Hz$; $P = 13\ kPa$; $U_0 = 37.08\ m\ s^{-1}$

2. Typical Images from the Zones of Soot Formation

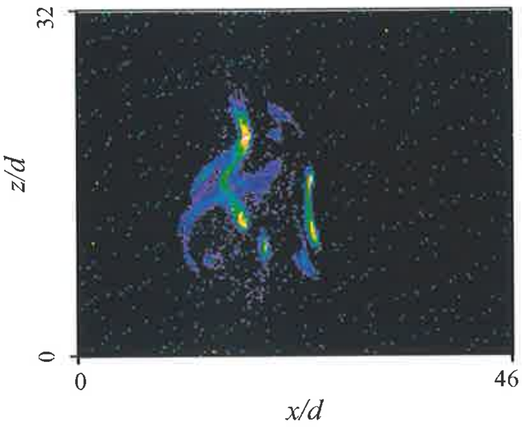

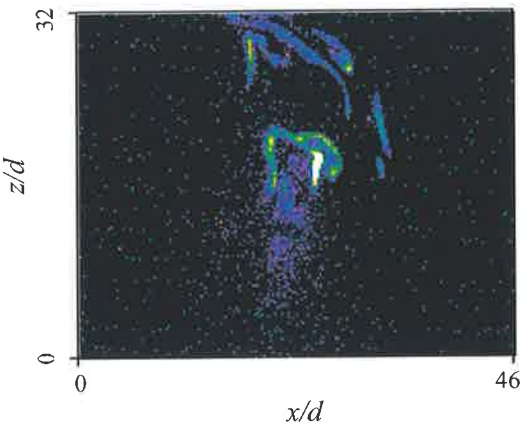

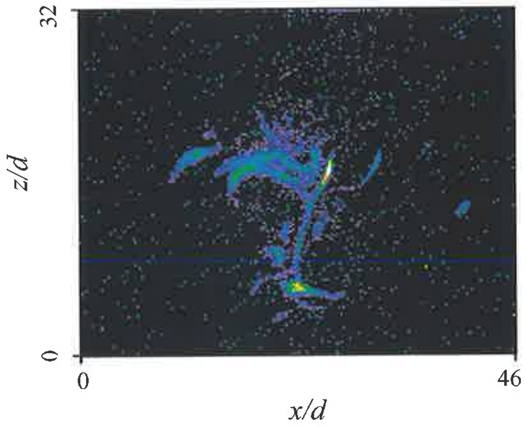

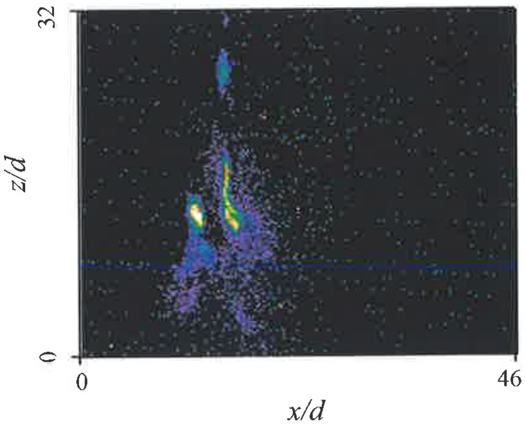

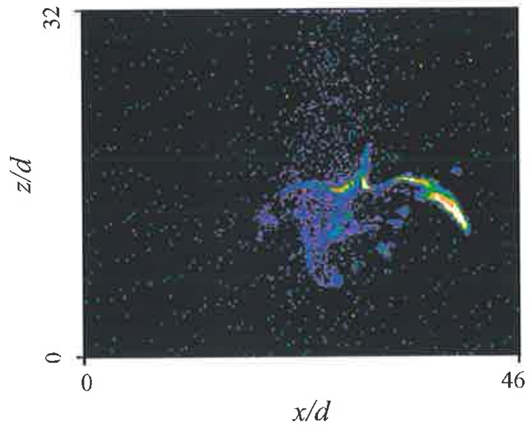

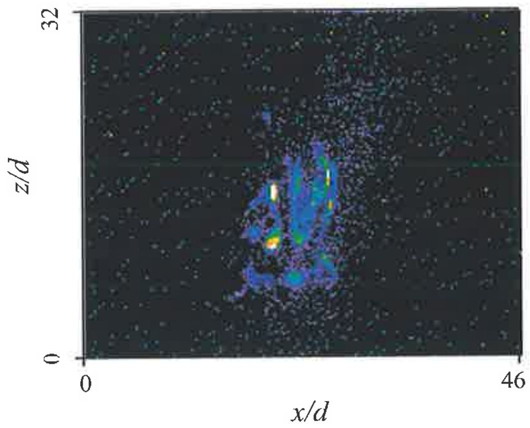

Appendix A-33

1. Experimental Conditions

$Re = 4329$; $St = 0.0106$; $f = 30.5\ Hz$; $P = 5\ kPa$; $U_0 = 14.30\ m\,s^{-1}$

2. Typical Images from the Zones of Soot Formation

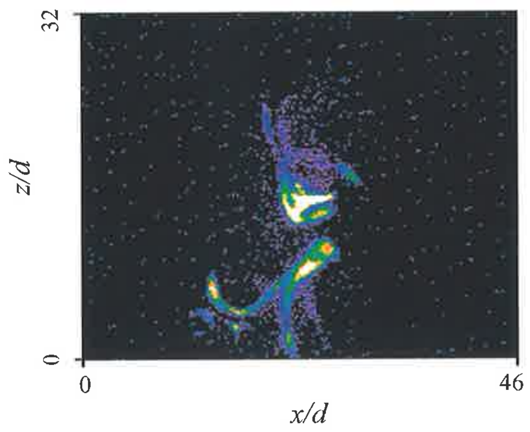

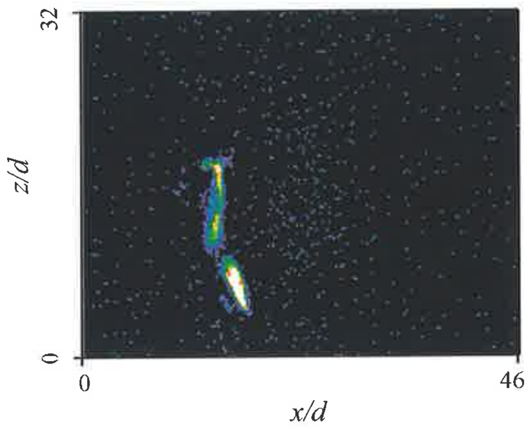

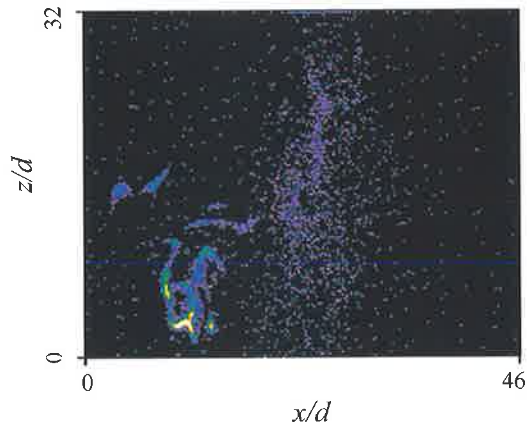

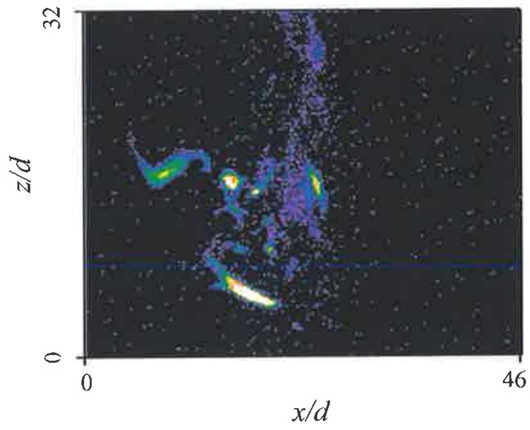

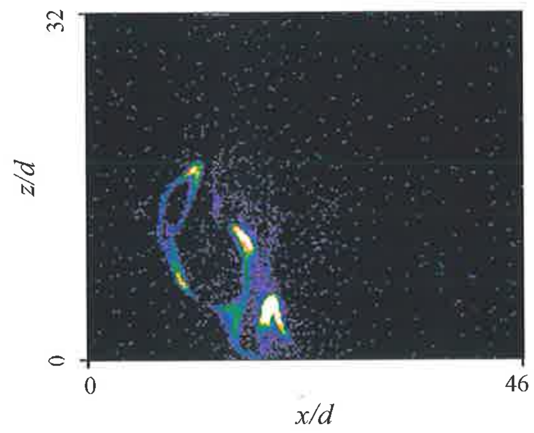

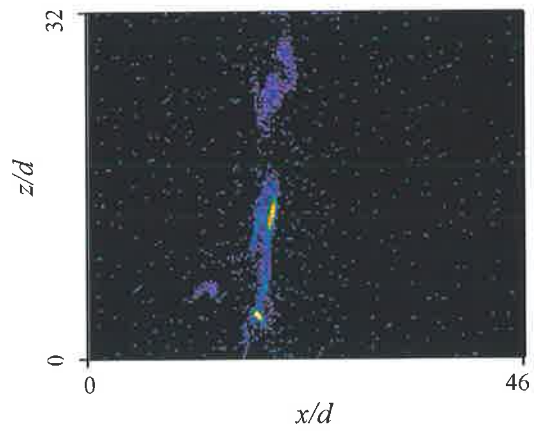

Appendix A-34

1. Experimental Conditions

$Re = 5437$; $St = 0.0106$; $f = 38\ Hz$; $P = 6\ kPa$; $U_0 = 17.96\ m\ s^{-1}$

2. Typical Images from the Zones of Soot Formation

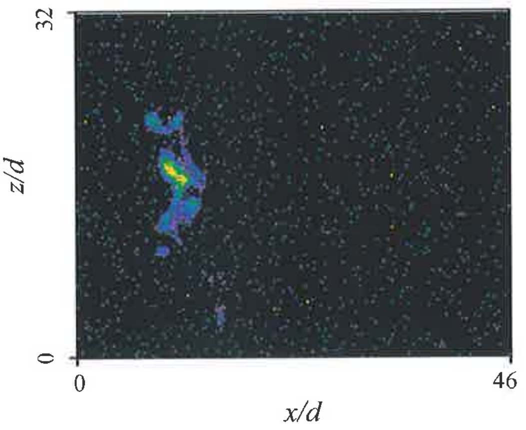

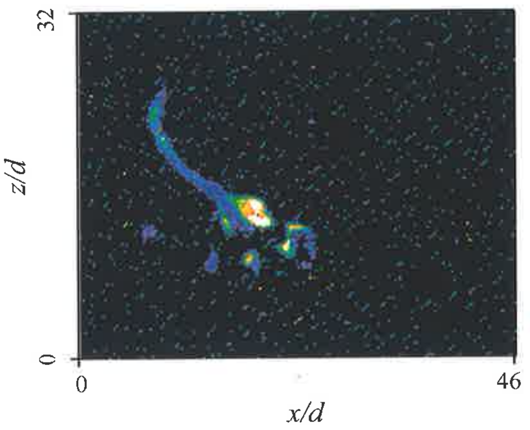

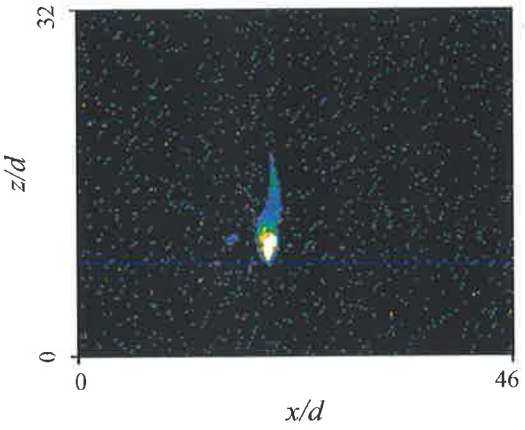

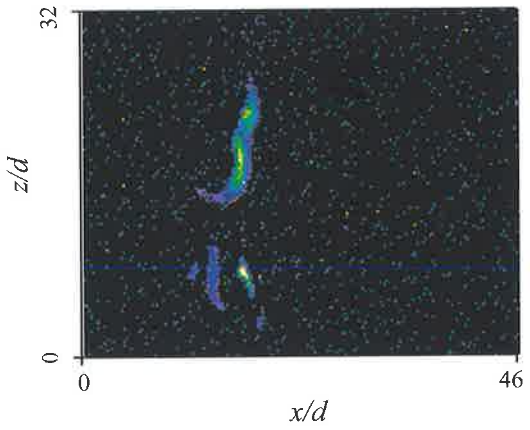

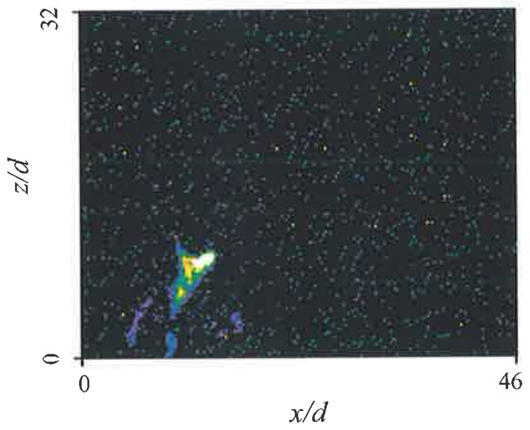

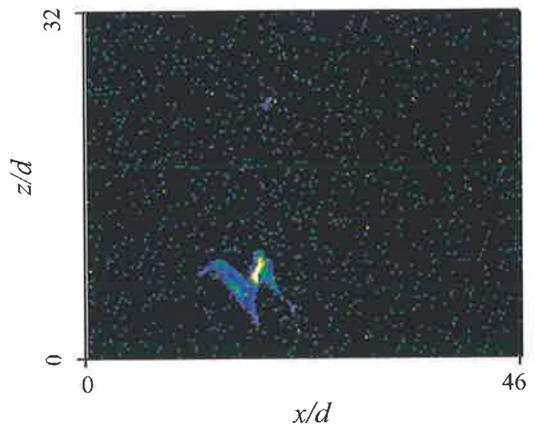

Appendix A-35

1. Experimental Conditions

$Re = 6555$; $St = 0.0106$; $f = 46\ Hz$; $P = 7\ kPa$; $U_0 = 21.65\ m\ s^{-1}$

2. Typical Images from the Zones of Soot Formation

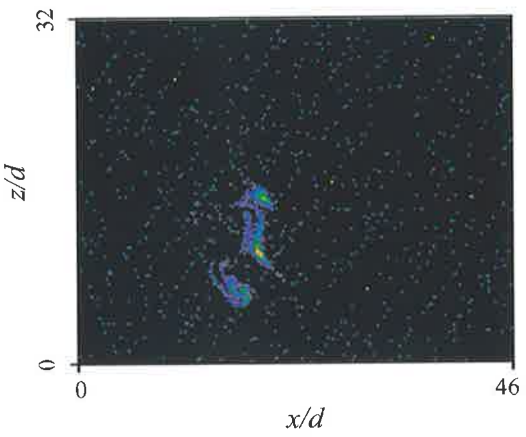

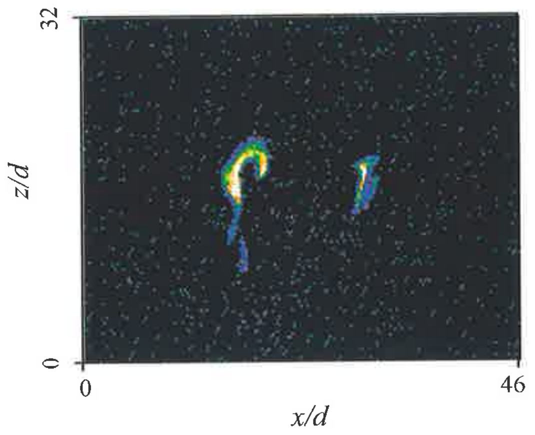

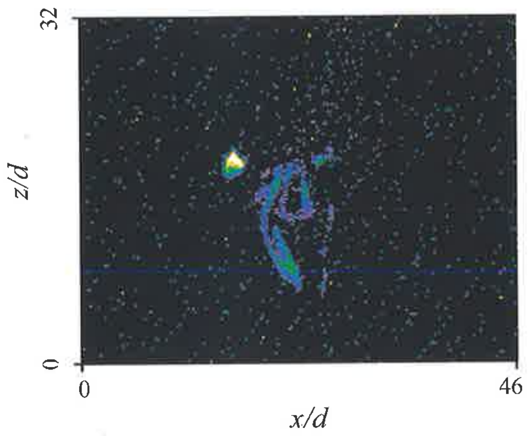

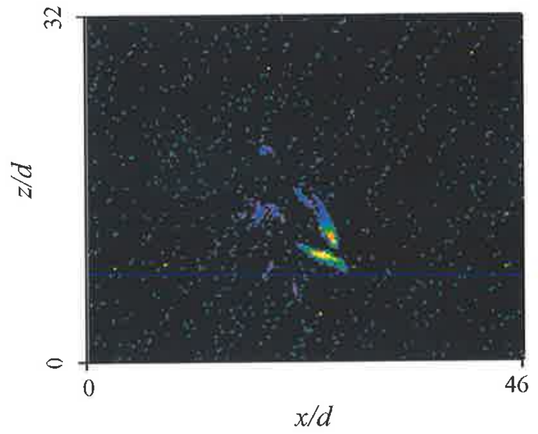

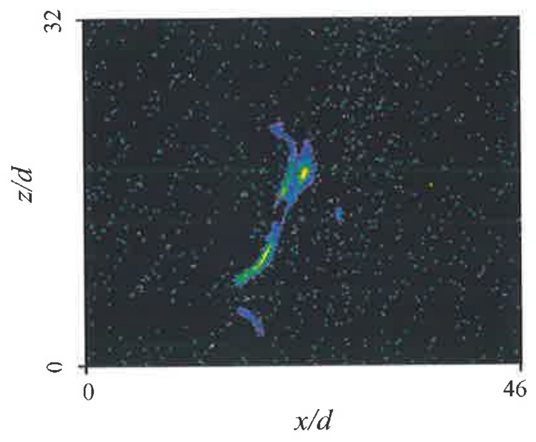

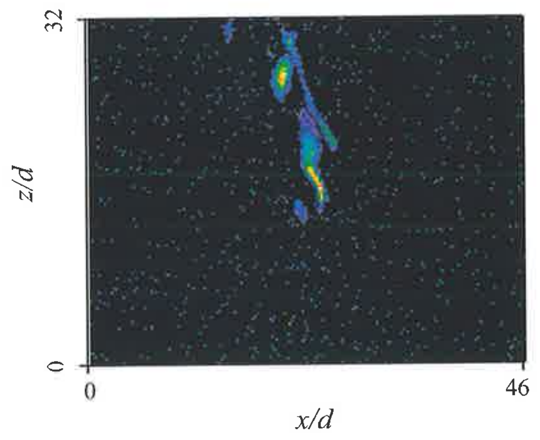

Appendix A-36

1. Experimental Conditions

$Re = 7682$; $St = 0.0106$; $f = 54\ Hz$; $P = 8\ kPa$; $U_0 = 25.38\ m\ s^{-1}$

2. Typical Images from the Zones of Soot Formation

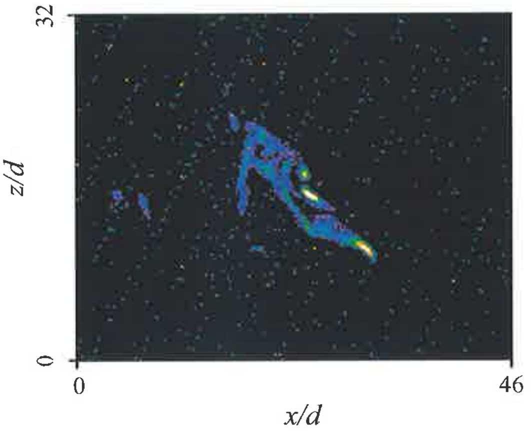

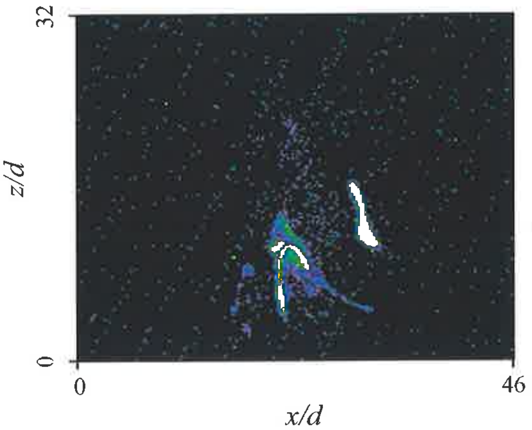

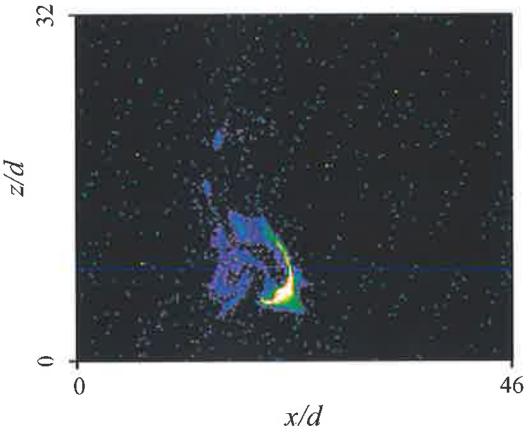

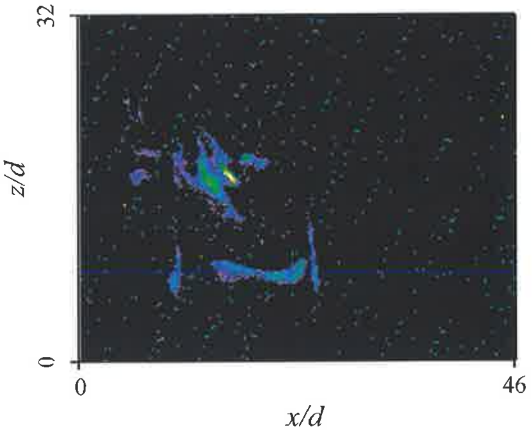

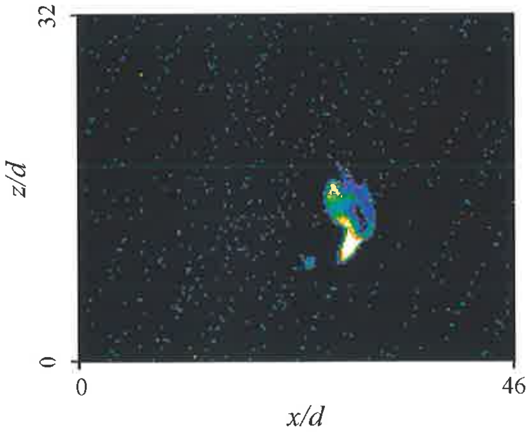

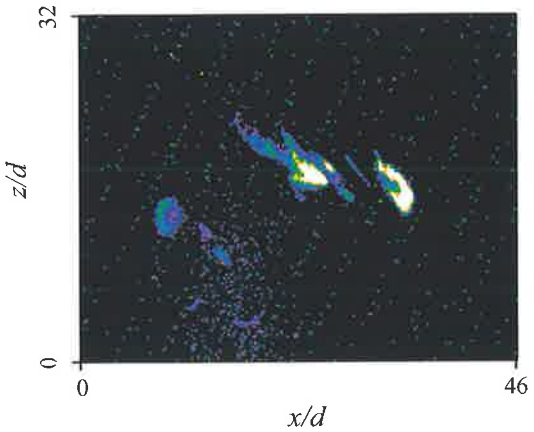

Appendix A-37

1. Experimental Conditions

$Re = 8840$; $St = 0.0106$ $f = 61.7\ Hz$; $P = 9{,}5\ kPa$; $U_0 = 29.20\ m\ s^{-1}$

2. Typical Images from the Zones of Soot Formation

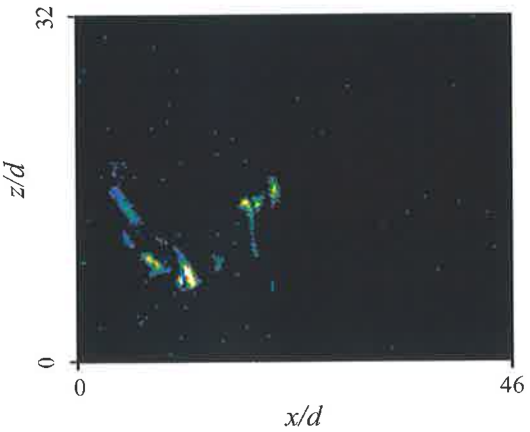

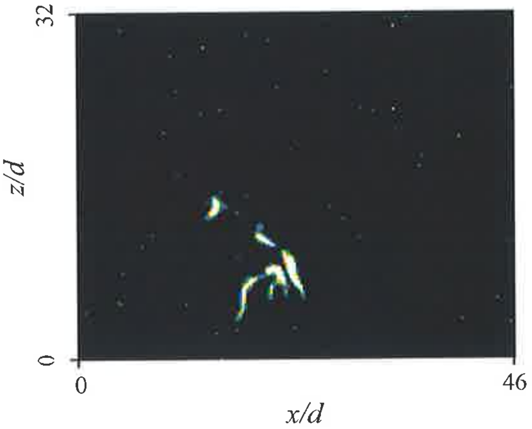

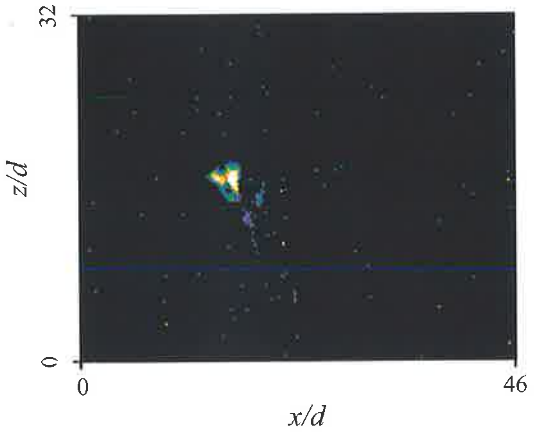

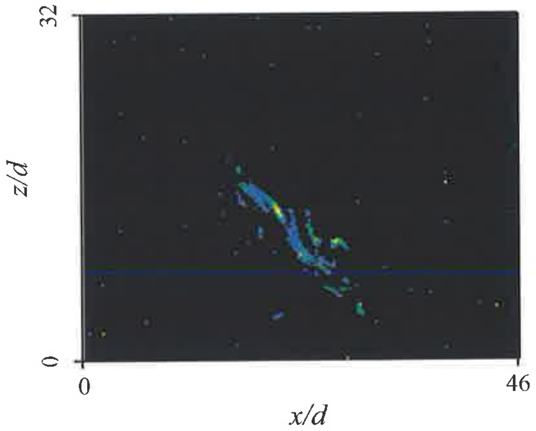

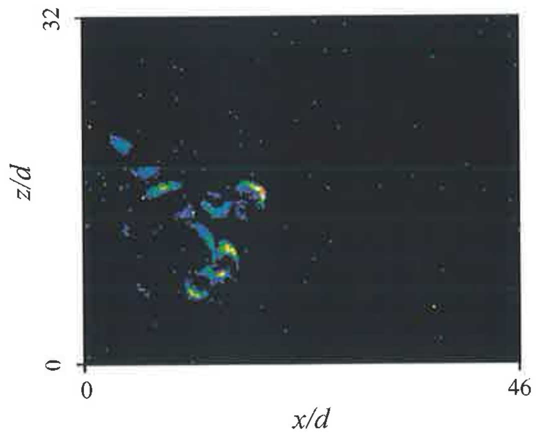

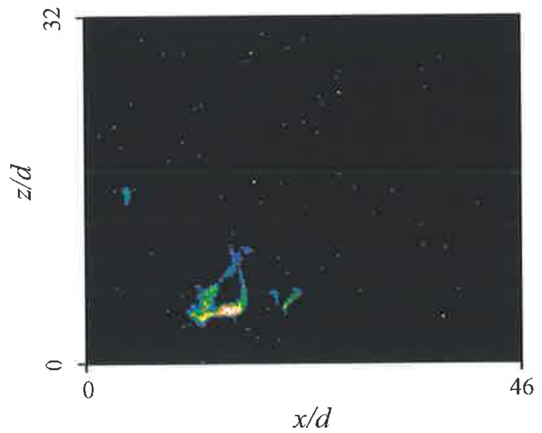

Appendix A-38

1. Experimental Conditions

$Re = 10012$; $St = 0.0106$; $f = 70Hz$; $P = 11kPa$; $U_0 = 33.08 m\,s^{-1}$

2. Typical Images from the Zones of Soot Formation

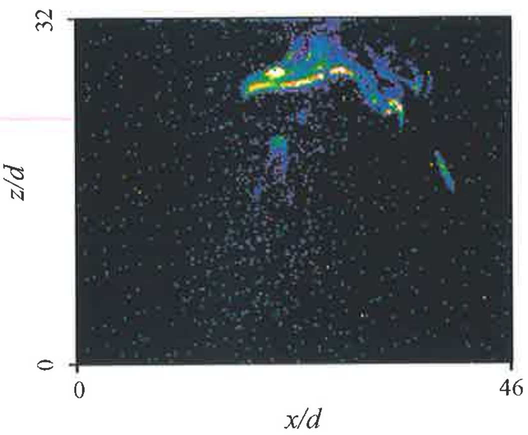

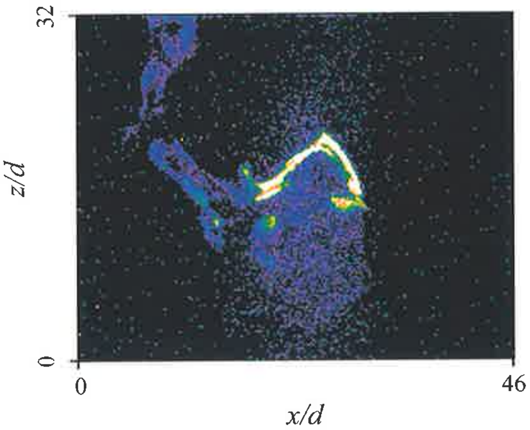

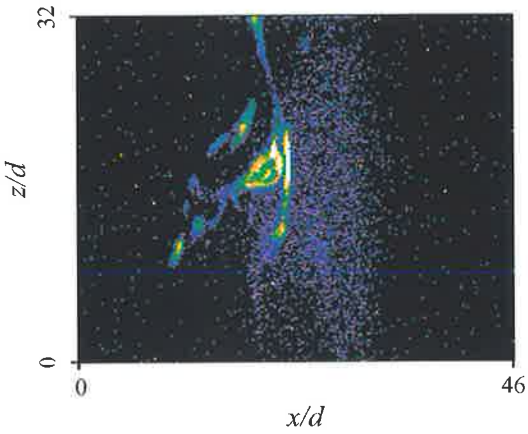

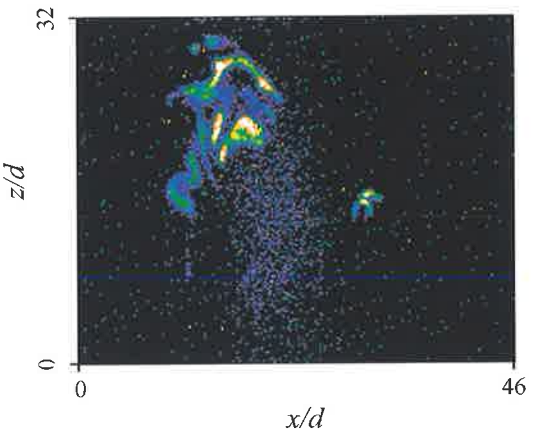

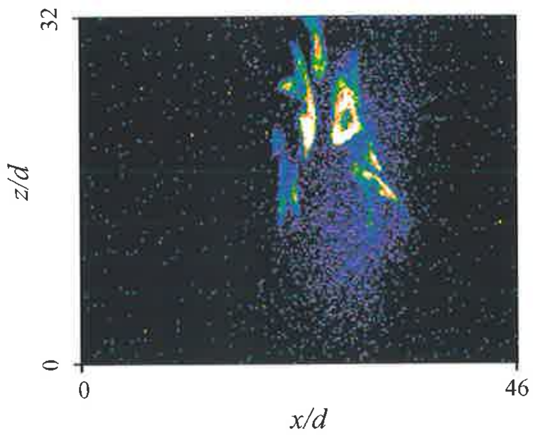

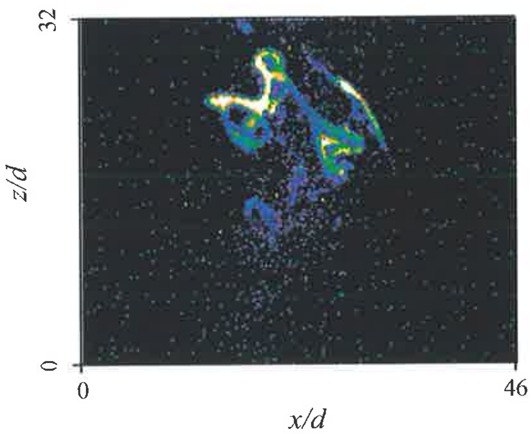

Appendix A-39

1. Experimental Conditions

$Re = 4329$; $St = 0.0116$; $f = 33.3\ Hz$; $P = 5\ kPa$; $U_0 = 14.30\ m\ s^{-1}$

2. Typical Images from the Zones of Soot Formation

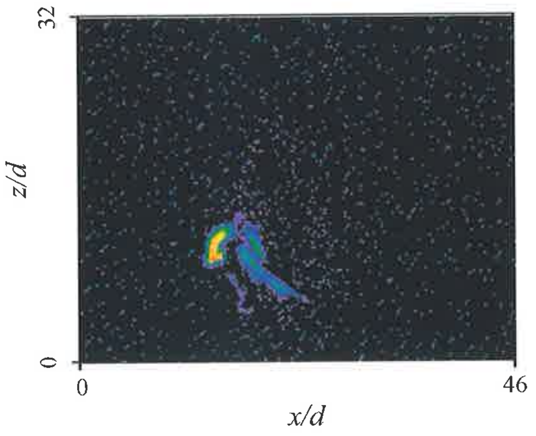

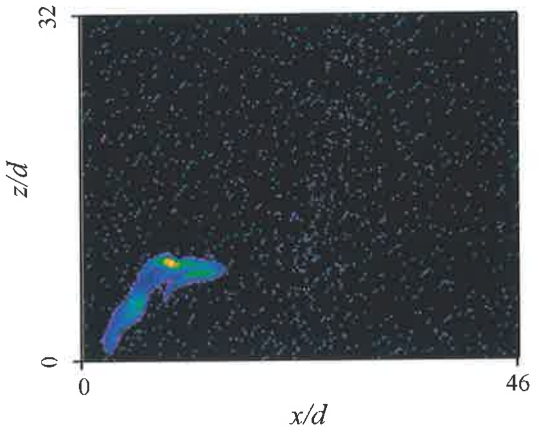

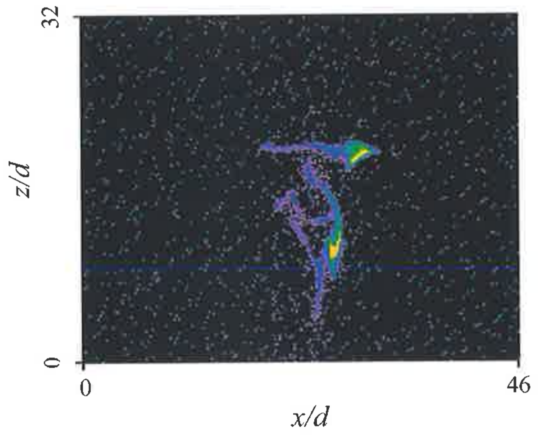

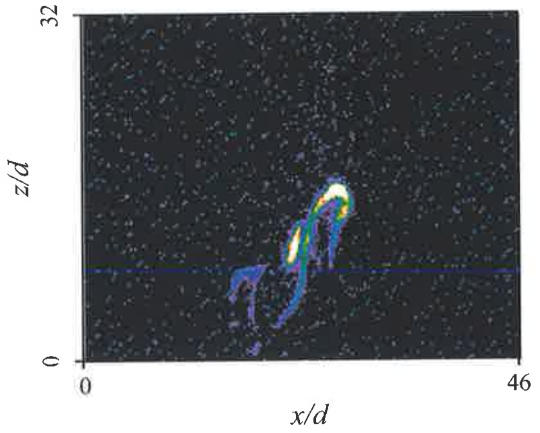

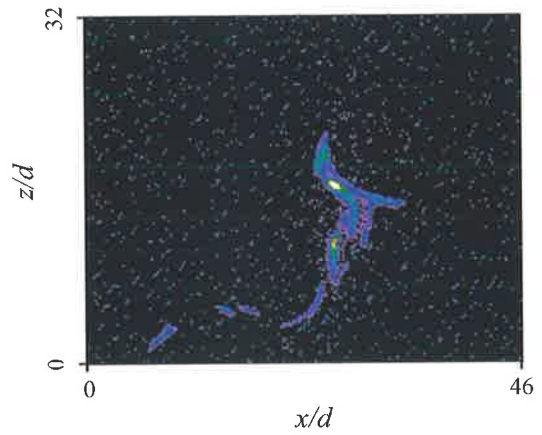

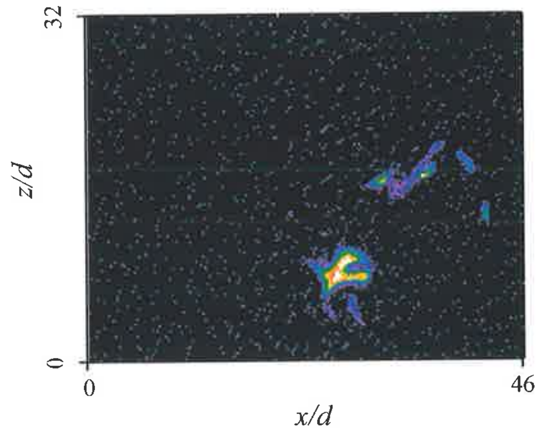

Appendix A-40

1. Experimental Conditions

$Re = 5437$; $St = 0.0116$; $f = 41.5\ Hz$; $P = 6\ kPa$; $U_0 = 17.96\ m\ s^{-1}$

2. Typical Images from the Zones of Soot Formation

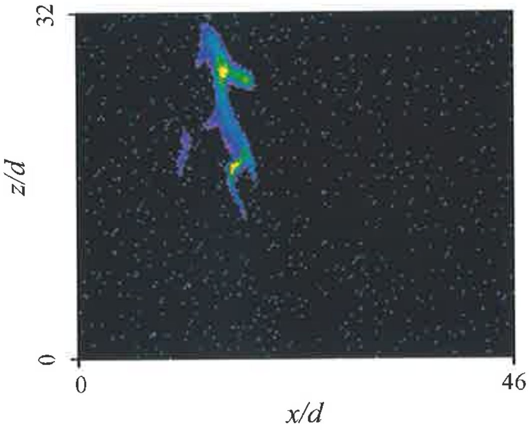

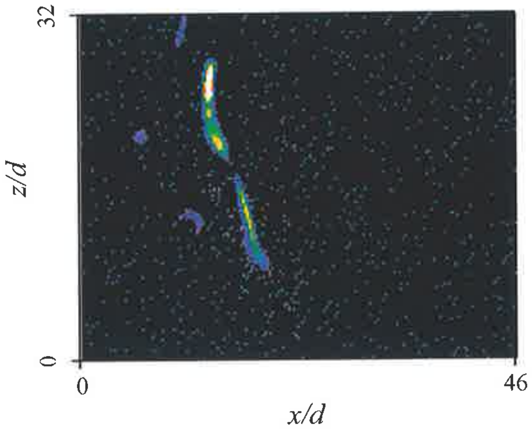

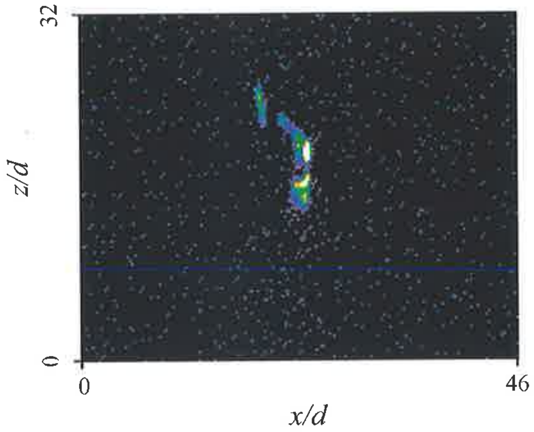

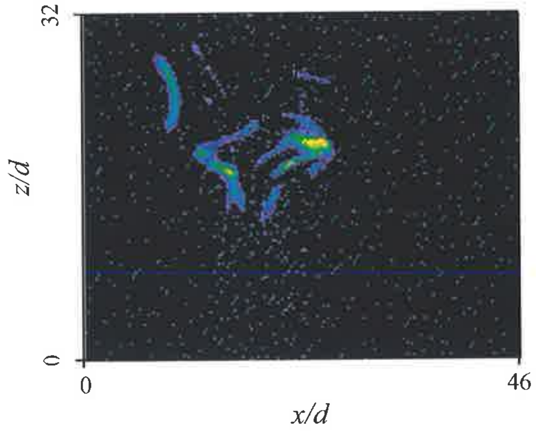

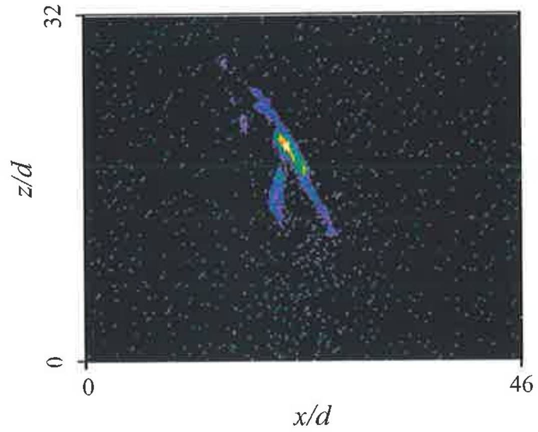

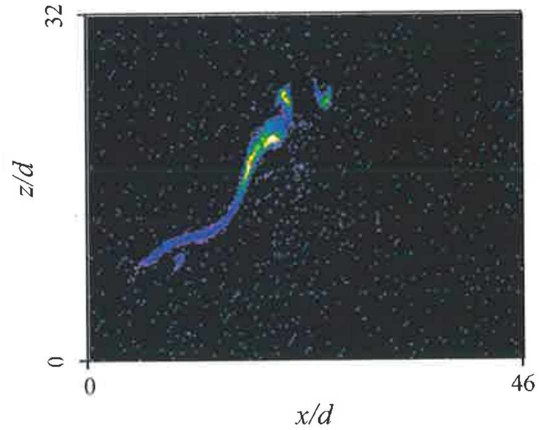

Appendix A-41

1. Experimental Conditions

$Re = 6555$; $St = 0.0116$; $f = 50\ Hz$; $P = 7\ kPa$; $U_0 = 21.65\ m\ s^{-1}$

2. Typical Images from the Zones of Soot Formation

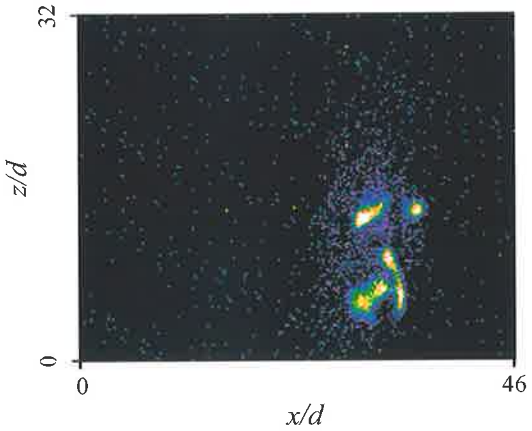

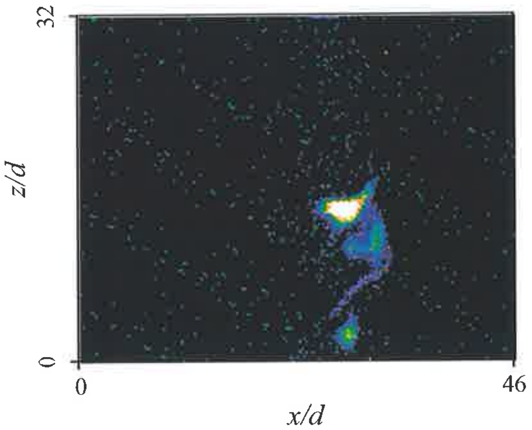

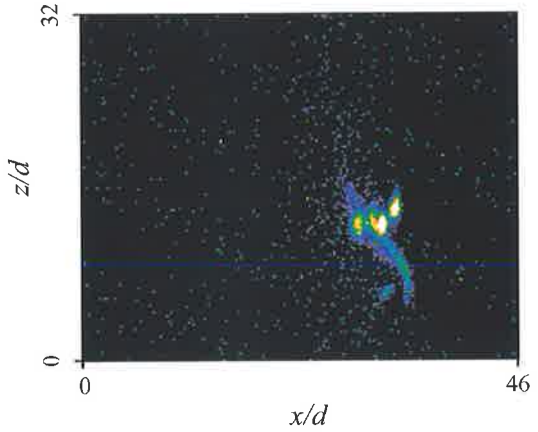

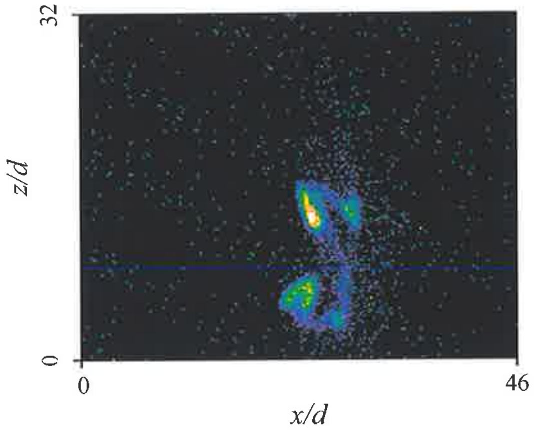

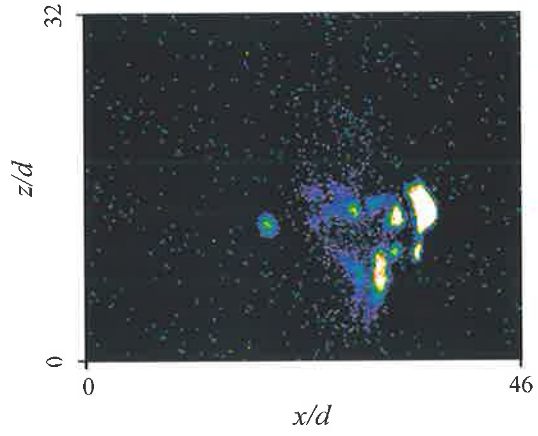

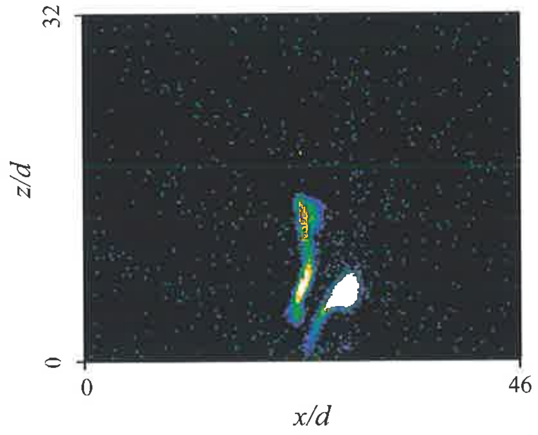

Appendix A-42

1. Experimental Conditions

$Re = 7682$; $St = 0.0116$; $f = 59.1\ Hz$; $P = 8\ kPa$; $U_0 = 25.38\ m\ s^{-1}$

2. Typical Images from the Zones of Soot Formation

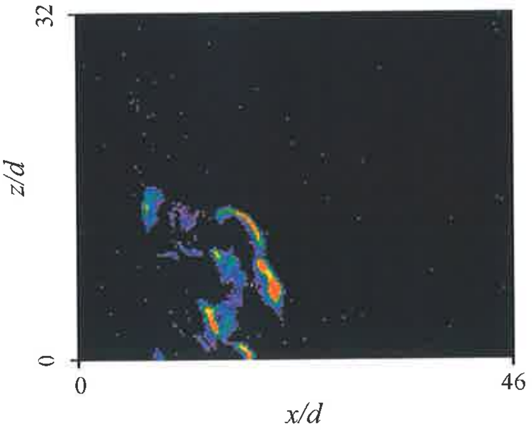

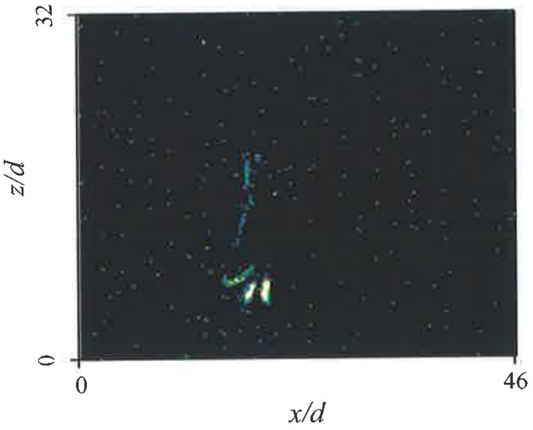

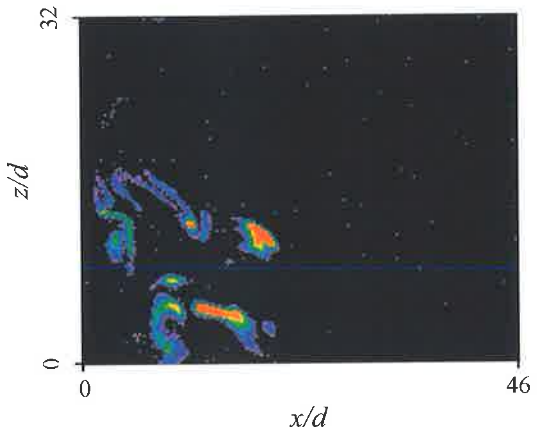

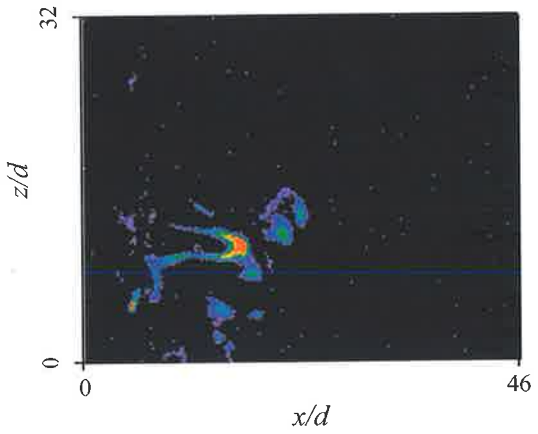

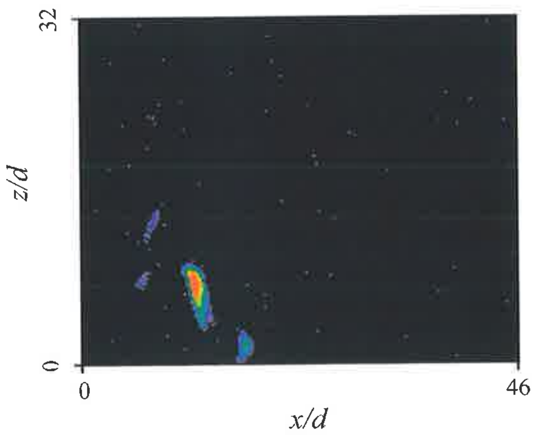

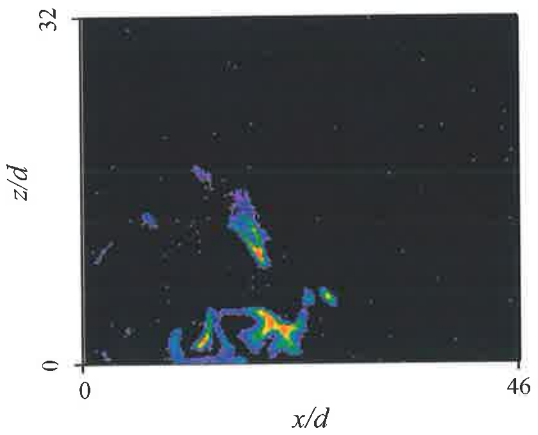

Appendix A-44

1. Experimental Conditions

$Re = 4329$; $St = 0.0139$; $f = 40\ Hz$; $P = 5\ kPa$; $U_0 = 14.30\ m\ s^{-1}$

2. Typical Images from the Zones of Soot Formation

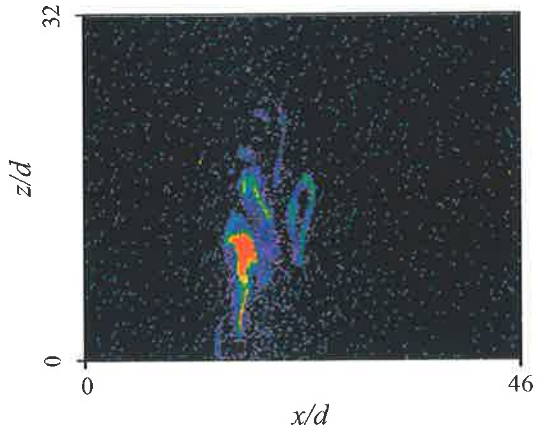

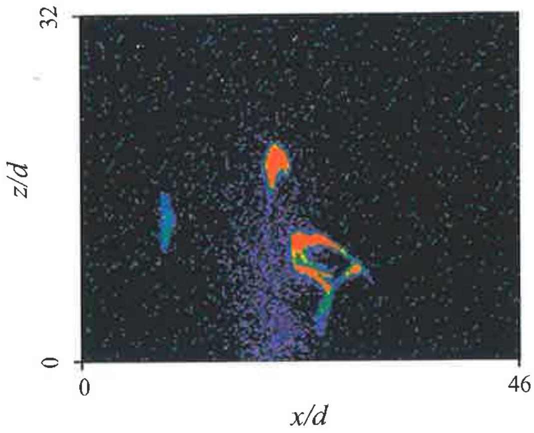

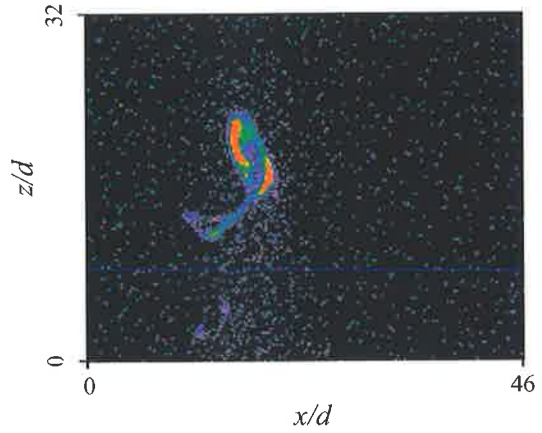

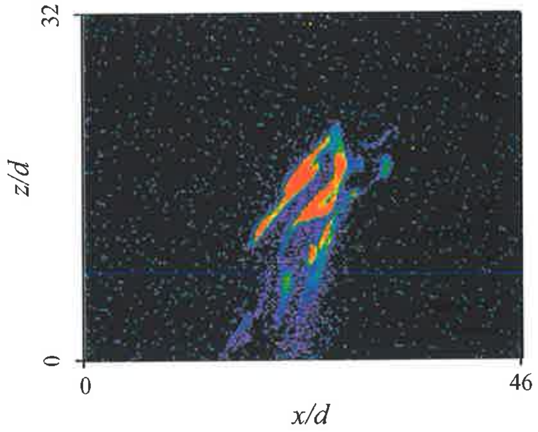

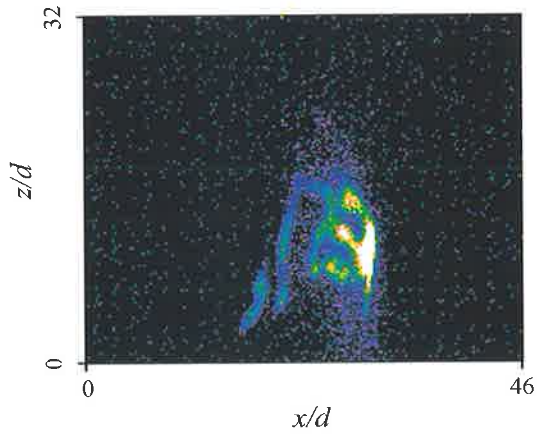

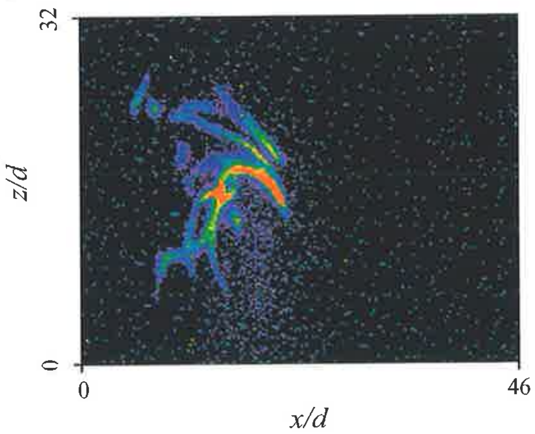

Appendix A-50

1. Experimental Conditions

$Re = 4329$; $St = 0.0210$; $f = 60\ Hz$; $P = 5\ kPa$; $U_0 = 14.30\ m\ s^{-1}$

2. Typical Images from the Zones of Soot Formation

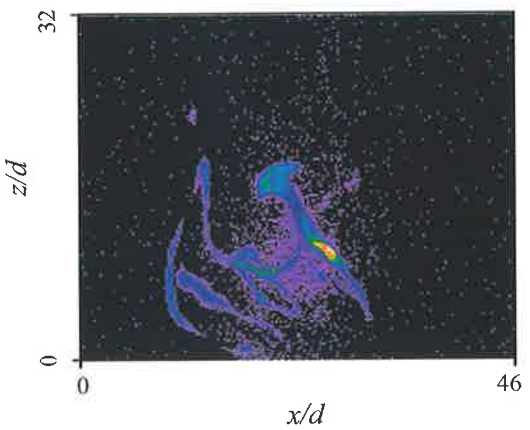

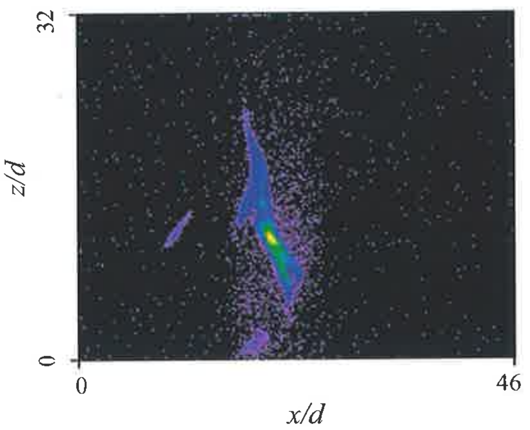

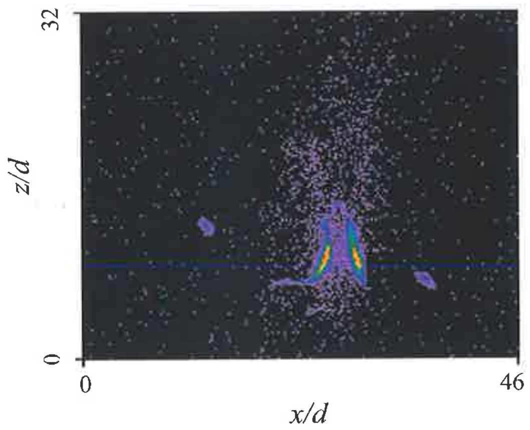

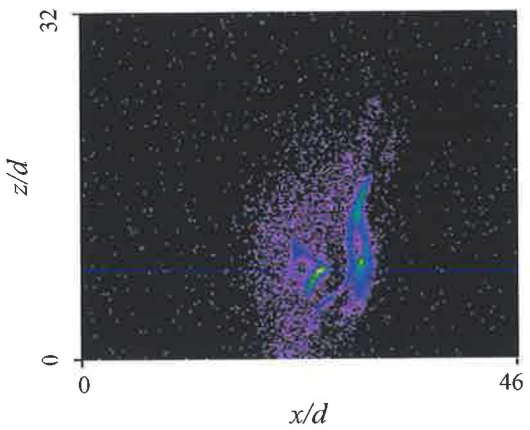

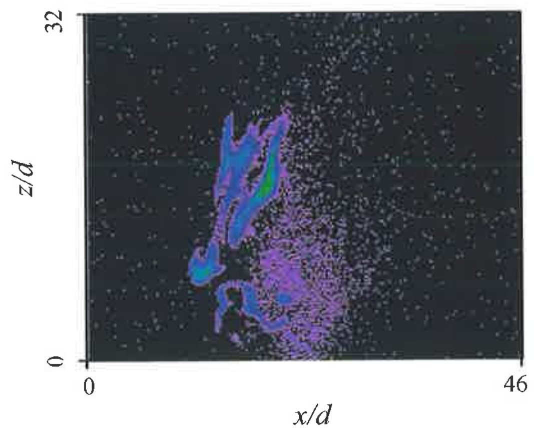

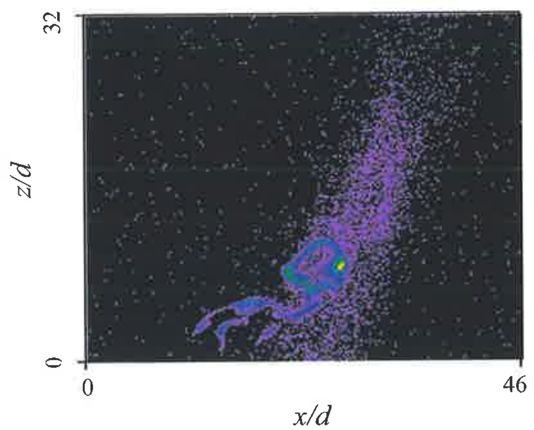

Appendix A-51

1. Experimental Conditions

$Re = 4329$; $St = 0.0245$; $f = 70\ Hz$; $P = 5\ kPa$; $U_0 = 14.30\ m\ s^{-1}$

2. Typical Images from the Zones of Soot Formation

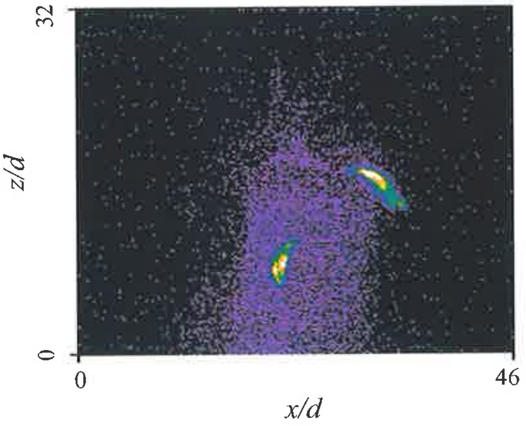

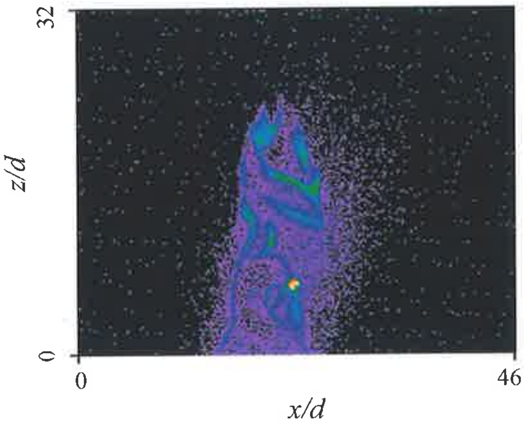

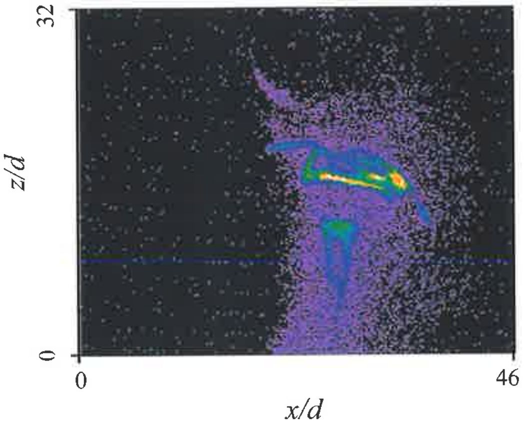

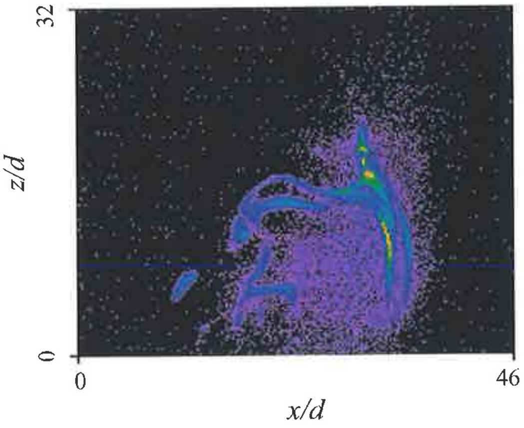

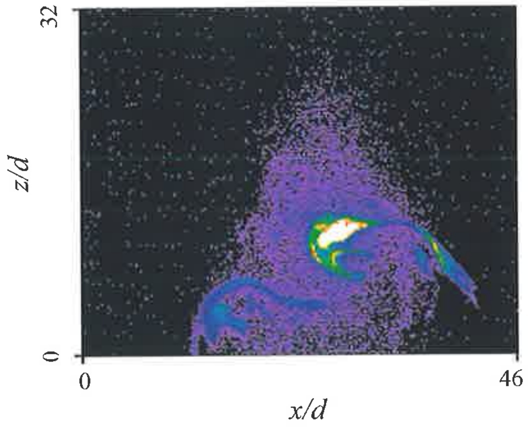

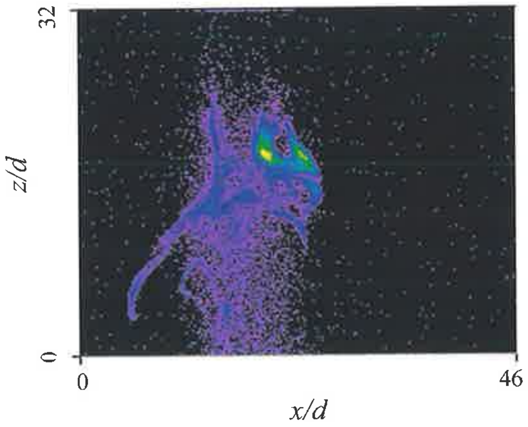

Appendix A-52

1. Experimental Conditions

$Re = 5437$; $St = 0.0050$; $f = 18\ Hz$; $P = 6\ kPa$; $U_0 = 17.96\ m\ s^{-1}$

2. Typical Images from the Zones of Soot Formation

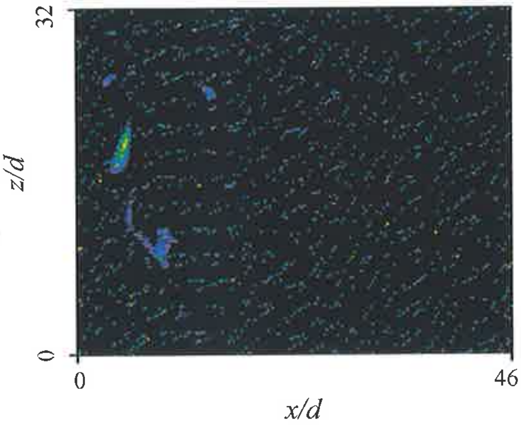

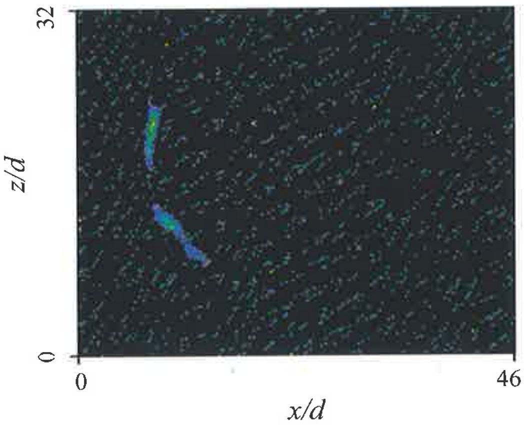

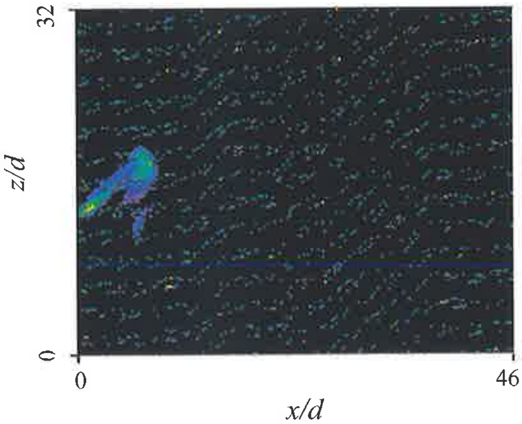

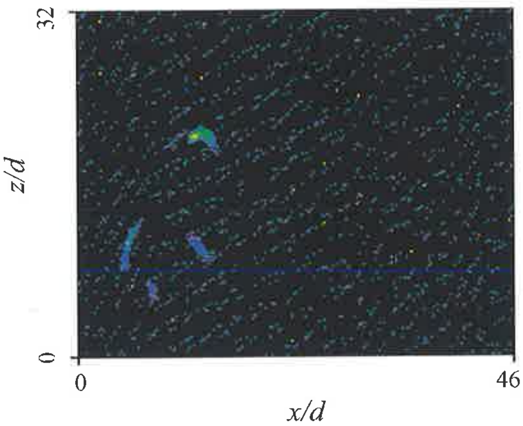

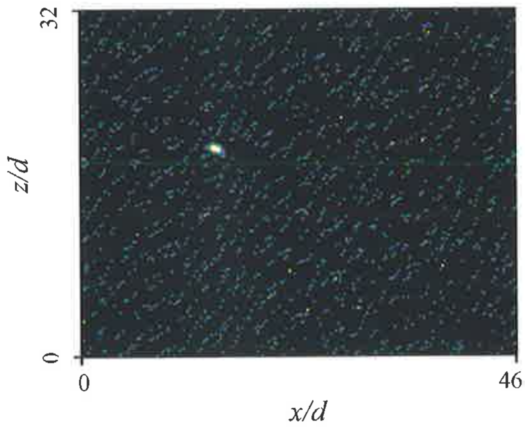

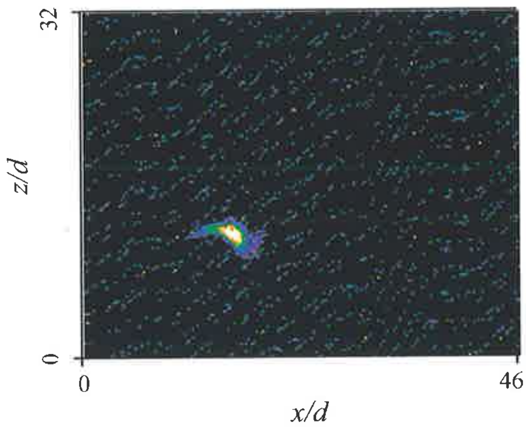

Appendix A-53

1. Experimental Conditions

$Re = 5437$; $St = 0.0167$; $f = 60\ Hz$; $P = 6\ kPa$; $U_0 = 17.96\ m\ s^{-1}$

2. Typical Images from the Zones of Soot Formation

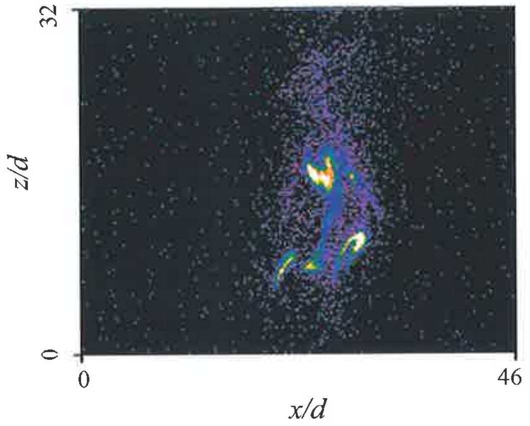

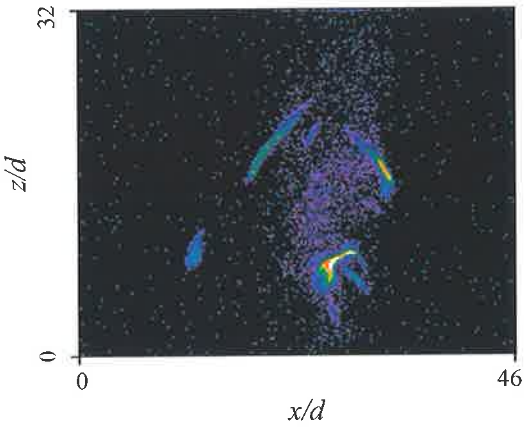

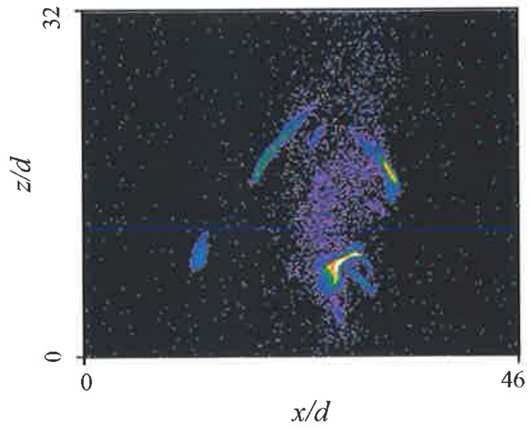

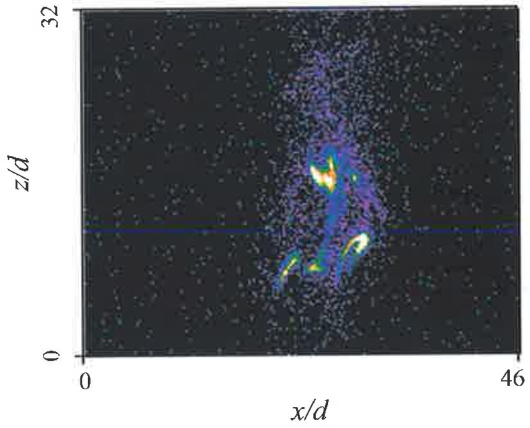

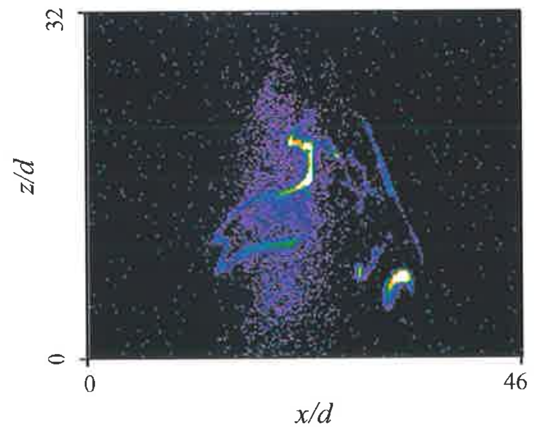

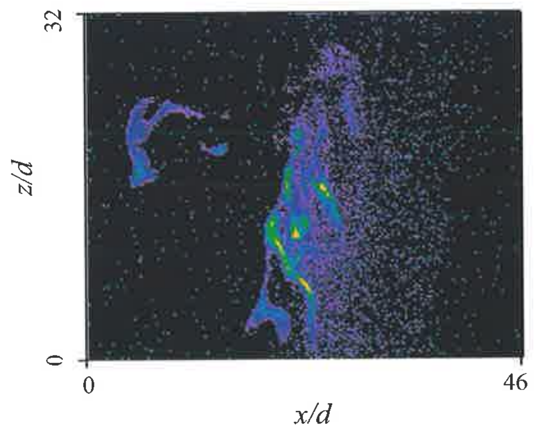

Appendix A-54

1. Experimental Conditions

$Re = 5437$; $St = 0.0195$; $f = 70\ Hz$; $P = 6\ kPa$; $U_0 = 17.96\ m\ s^{-1}$

2. Typical Images from the Zones of Soot Formation

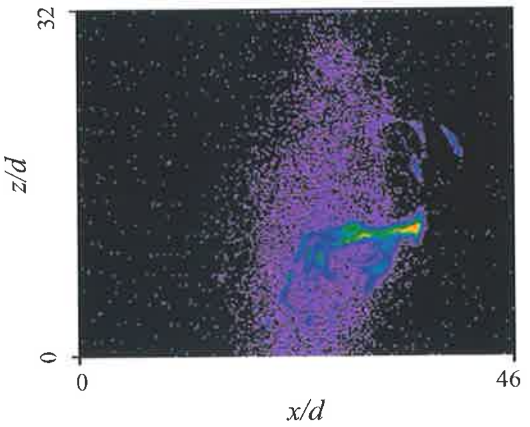

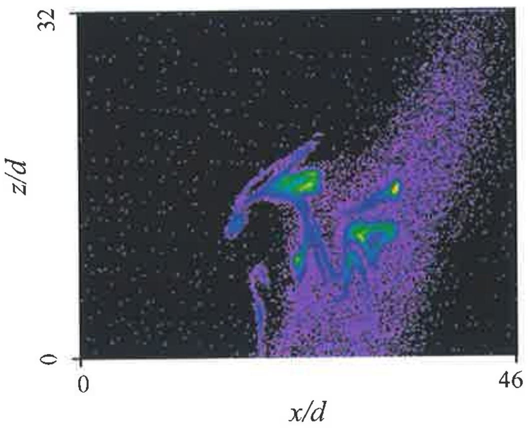

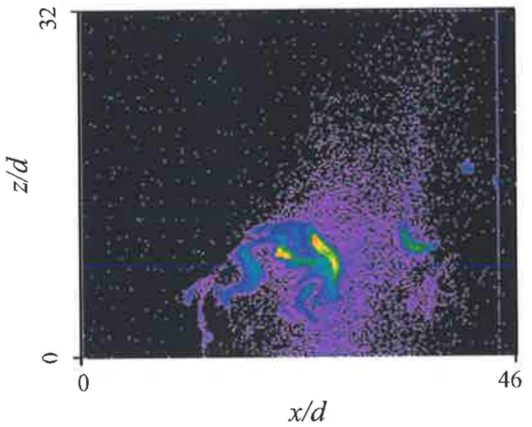

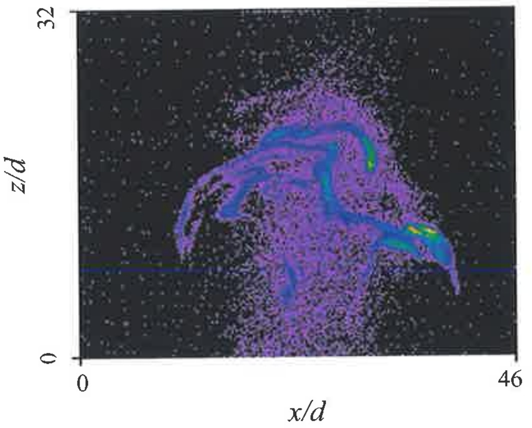

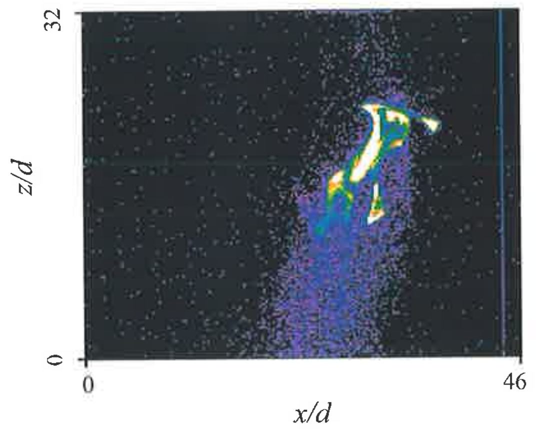

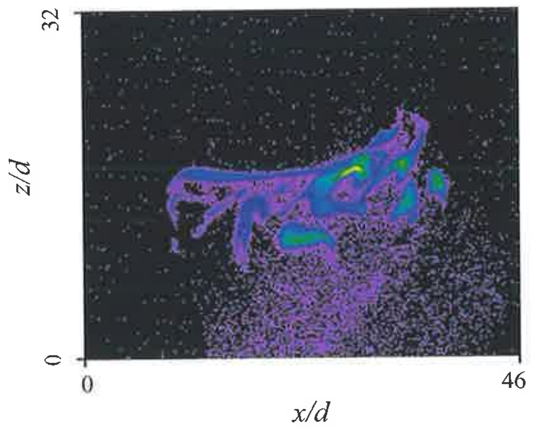

Appendix A-55

1. Experimental Conditions

$Re = 6555$; $St = 0.0042$; $f = 18\ Hz$; $P = 7\ kPa$; $U_0 = 21.65\ m\,s^{-1}$

2. Typical Images from the Zones of Soot Formation

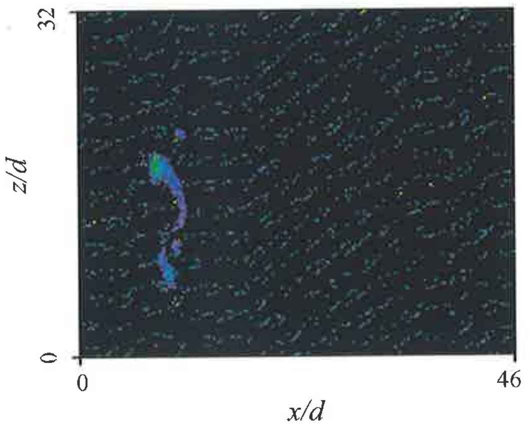

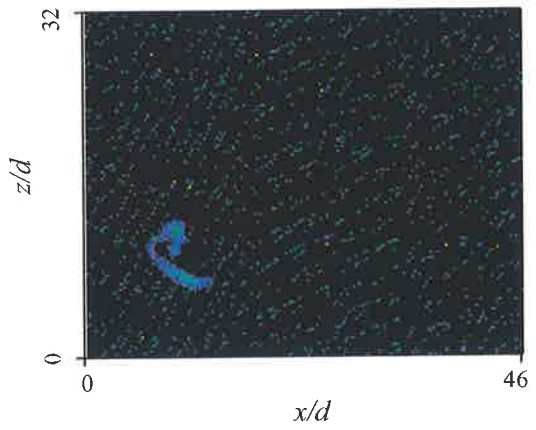

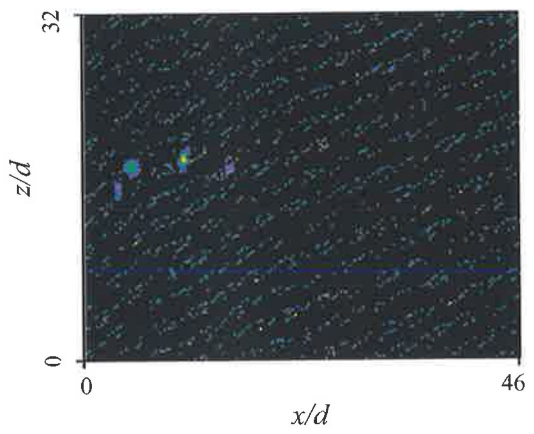

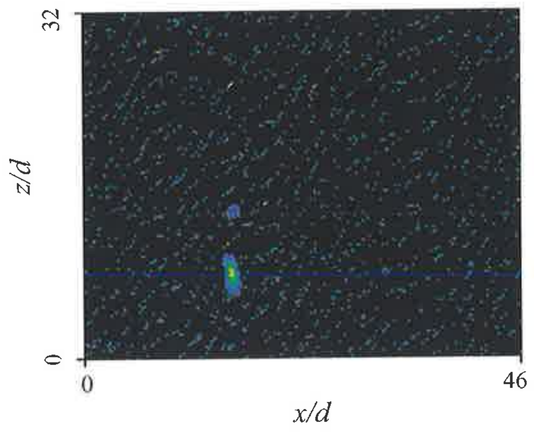

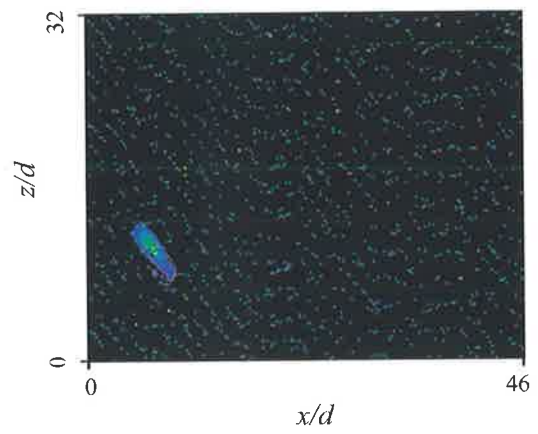

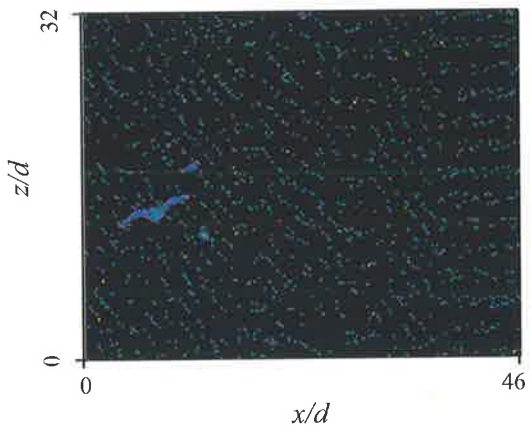

Appendix A-56

1. Experimental Conditions

$Re = 6555$; $St = 0.0046$; $f = 20\ Hz$; $P = 7\ kPa$; $U_0 = 21.65\ m\,s^{-1}$

2. Typical Images from the Zones of Soot Formation

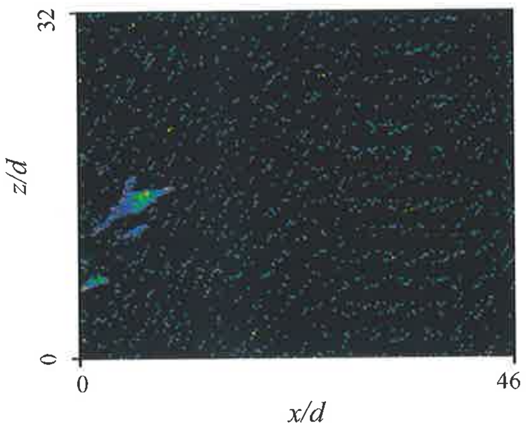

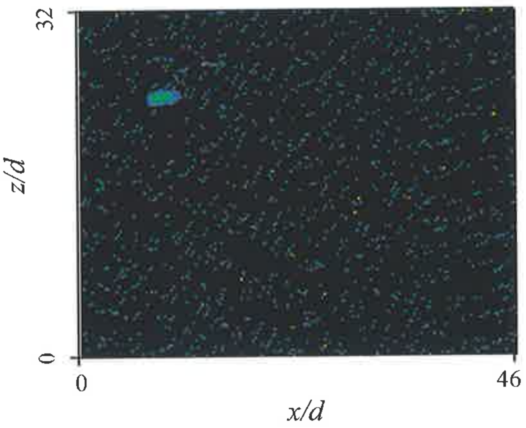

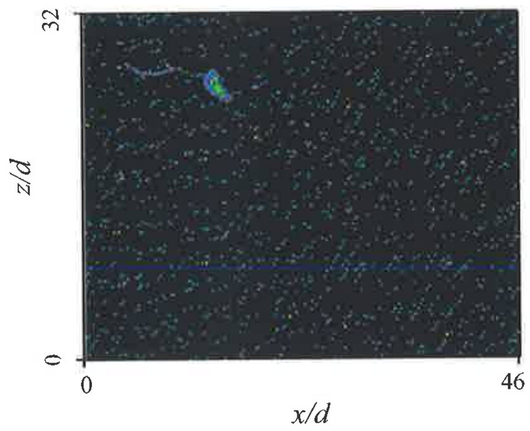

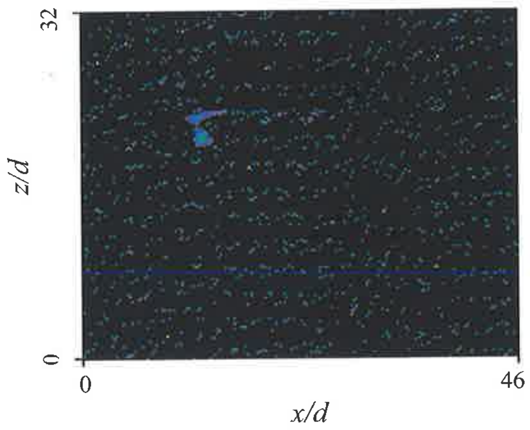

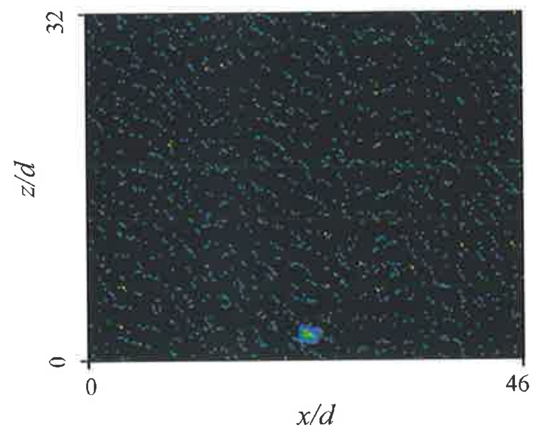

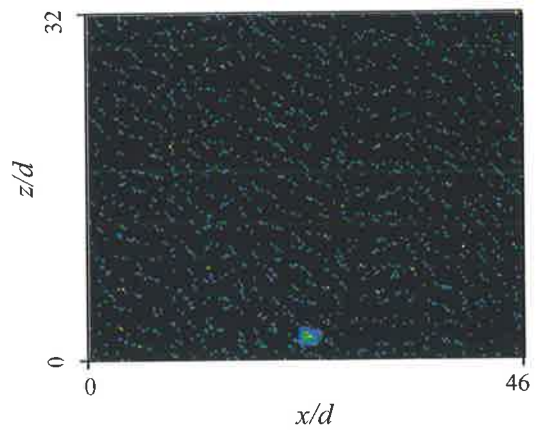

Appendix A-57

1. Experimental Conditions

$Re = 6555$; $St = 0.0052$; $f = 22.4\ Hz$; $P = 7\ kPa$; $U_0 = 21.65\ m\ s^{-1}$

2. Typical Images from the Zones of Soot Formation

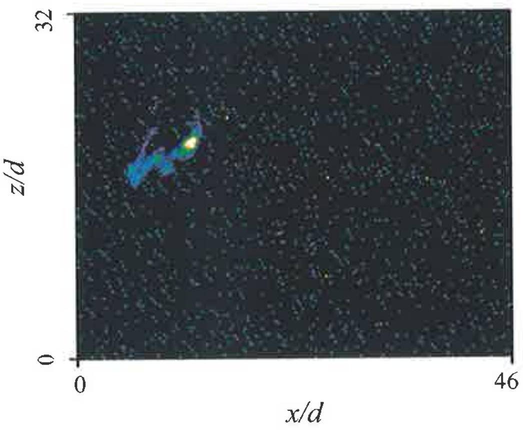

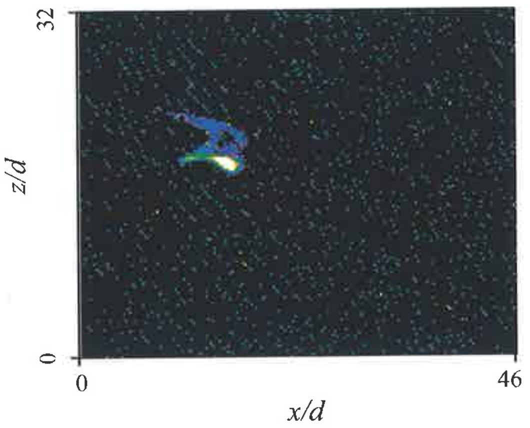

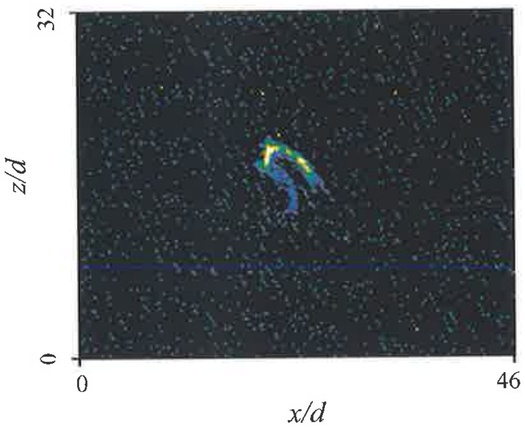

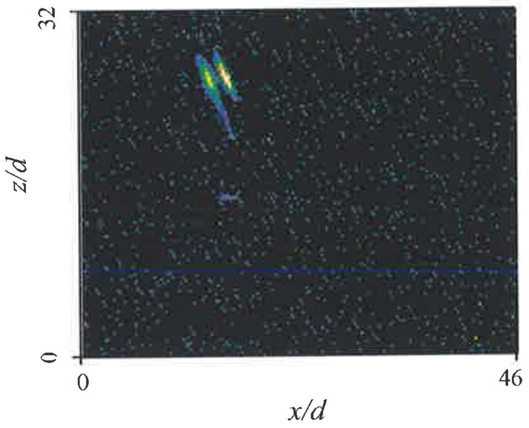

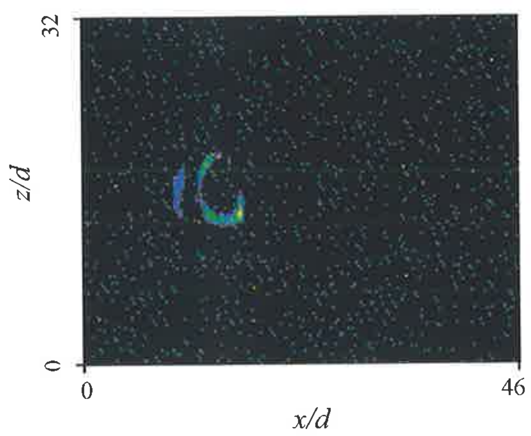

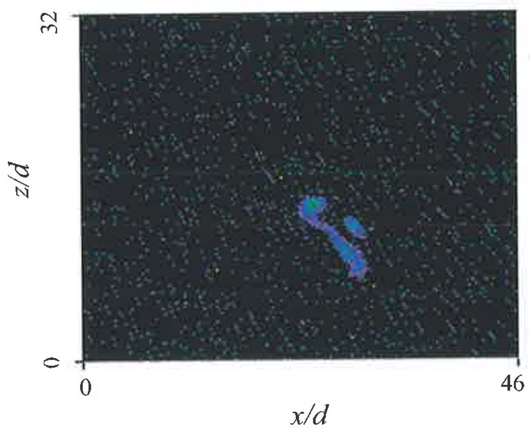

Appendix A-58

1. Experimental Conditions

$Re = 6555$; $St = 0.0083$; $f = 36.2\ Hz$; $P = 7\ kPa$; $U_0 = 21.65\ m\ s^{-1}$

2. Typical Images from the Zones of Soot Formation

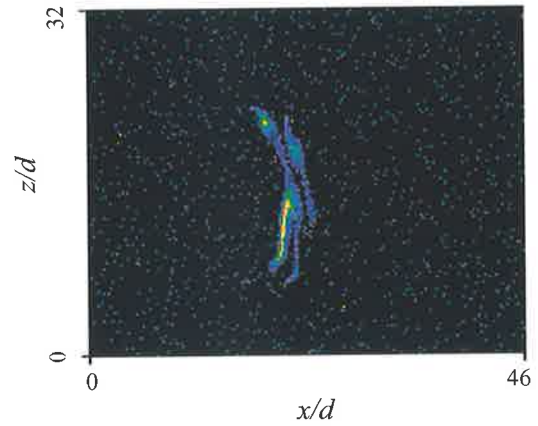

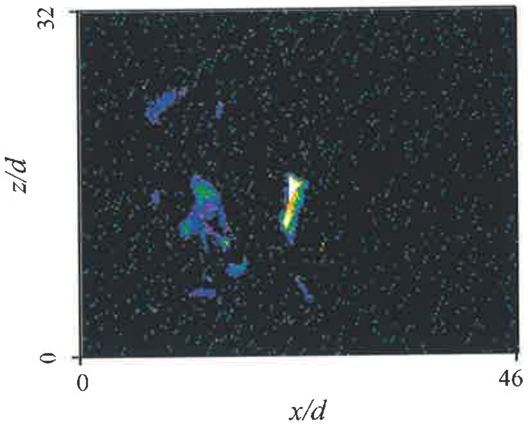

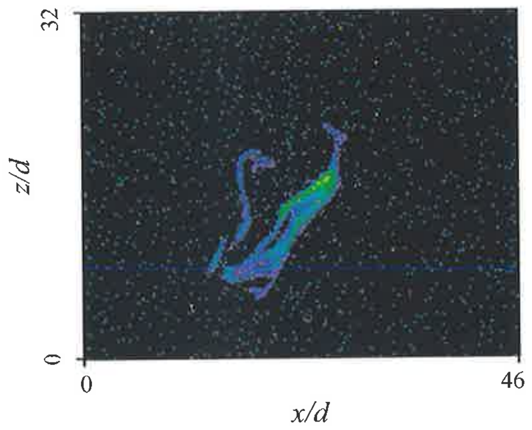

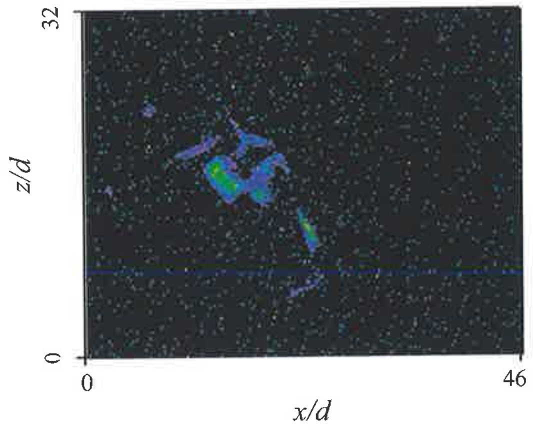

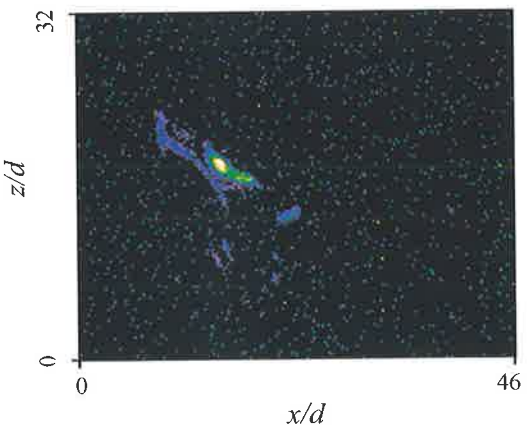

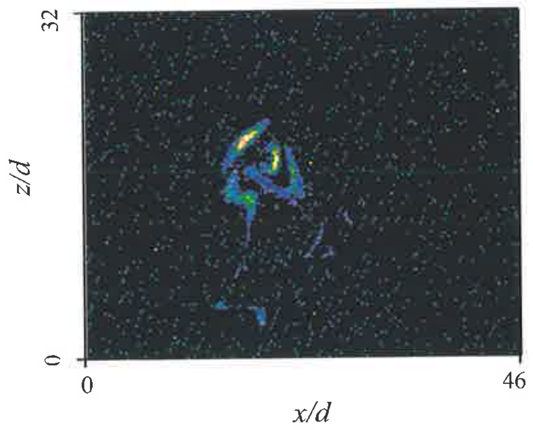

Appendix A-60

1. Experimental Conditions

$Re = 7682$; $St = 0.0044$; $f = 22.4\ Hz$; $P = 8\ kPa$; $U_0 = 25.40\ m\ s^{-1}$

2. Typical Images from the Zones of Soot Formation

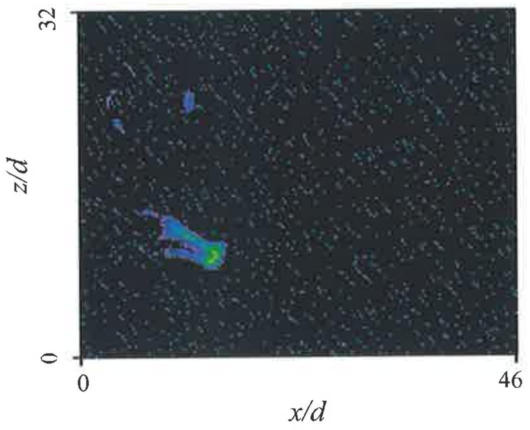

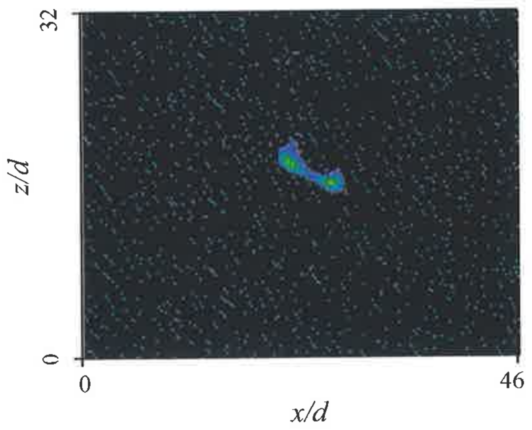

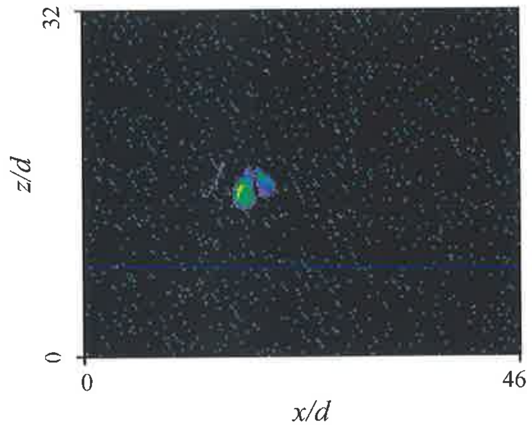

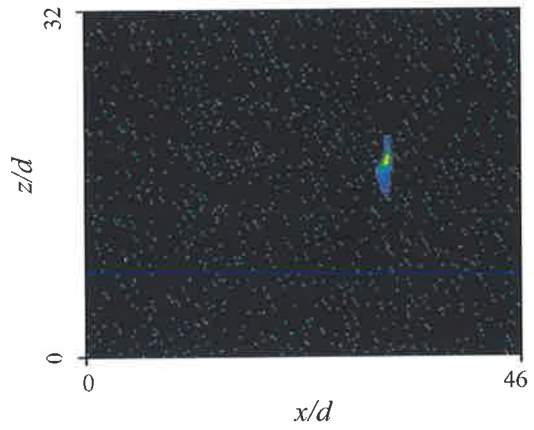

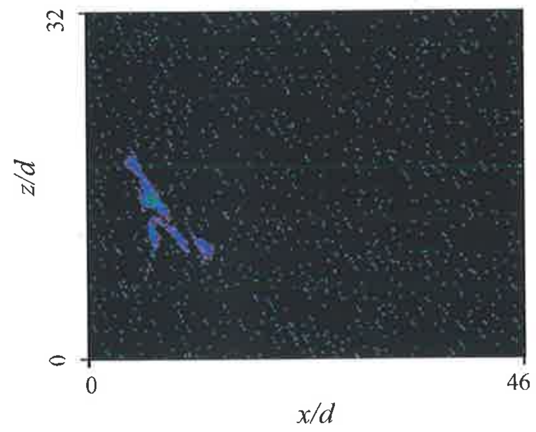

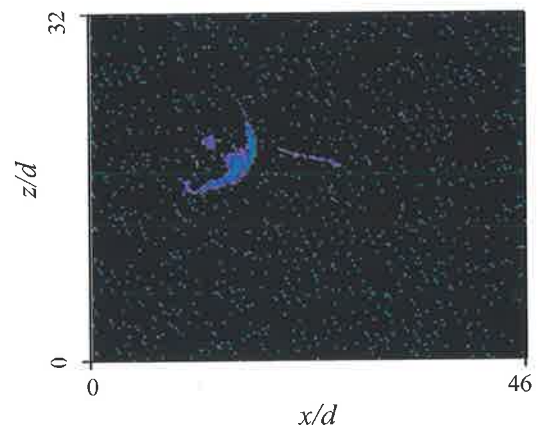

Appendix A-61

1. Experimental Conditions

$Re = 7682$; $St = 0.0048$; $f = 24.2\ Hz$; $P = 8\ kPa$; $U_0 = 25.40\ m\ s^{-1}$

2. Typical Images from the Zones of Soot Formation

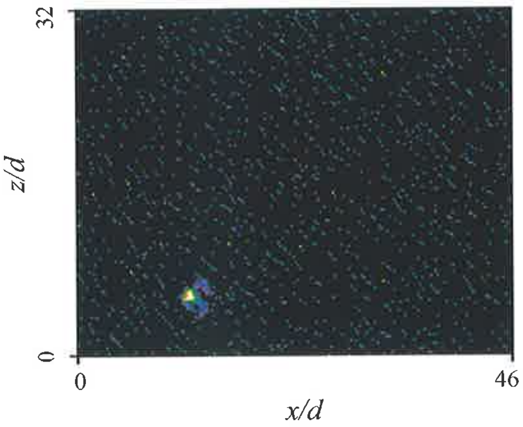

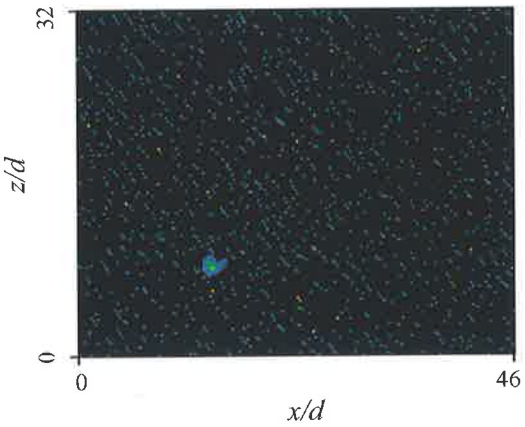

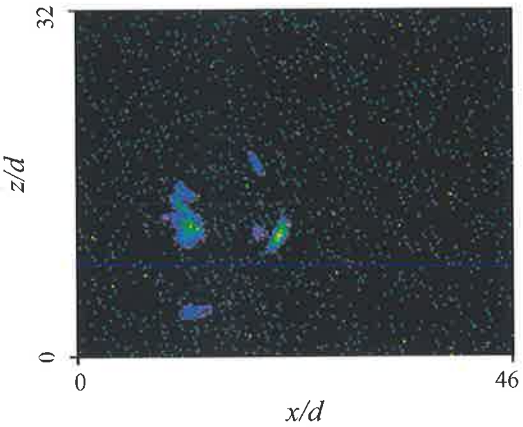

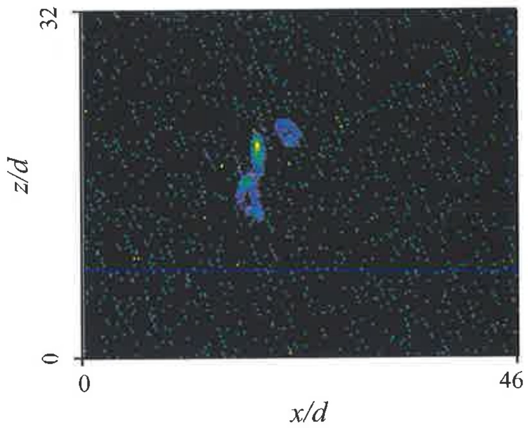

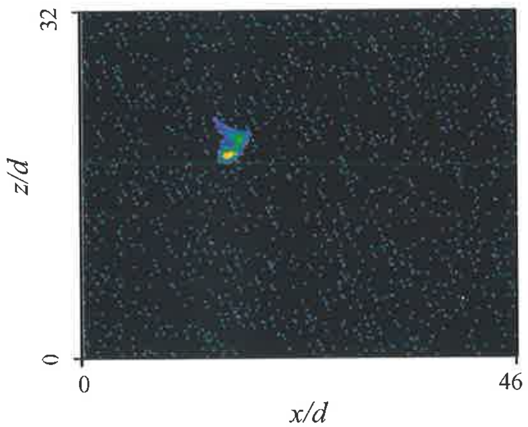

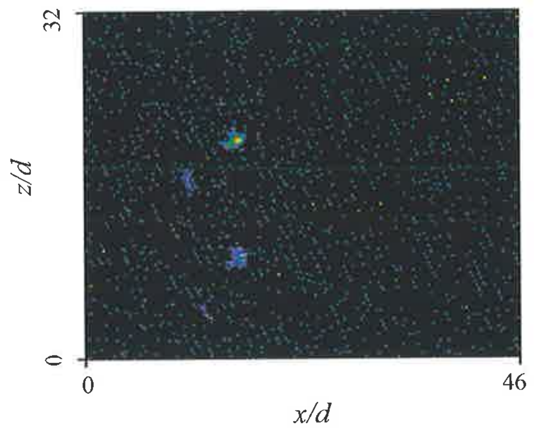

Appendix A-62

1. Experimental Conditions

$Re = 7682$; $St = 0.0053$; $f = 27\ Hz$; $P = 8\ kPa$; $U_0 = 25.40\ m\ s^{-1}$

2. Typical Images from the Zones of Soot Formation

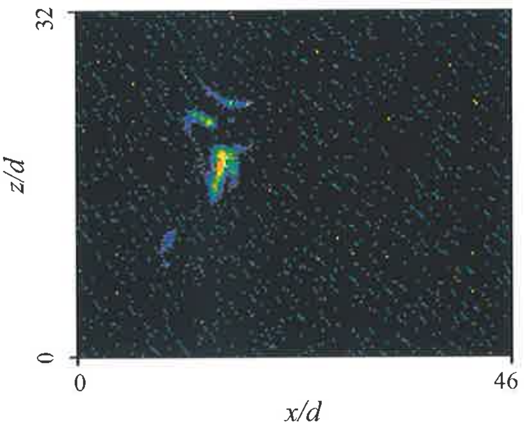

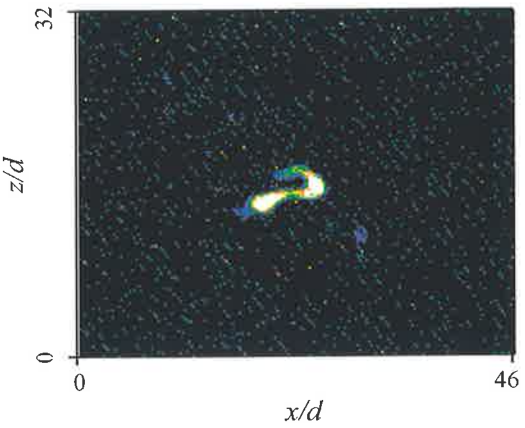

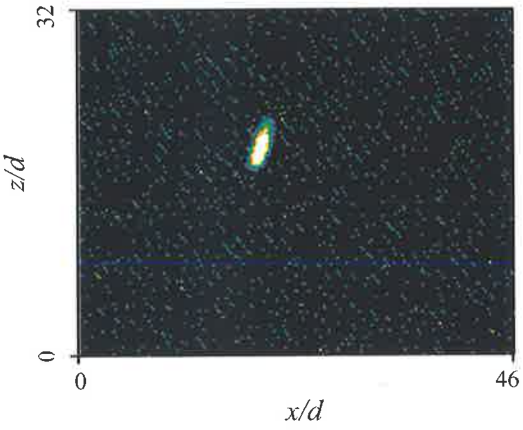

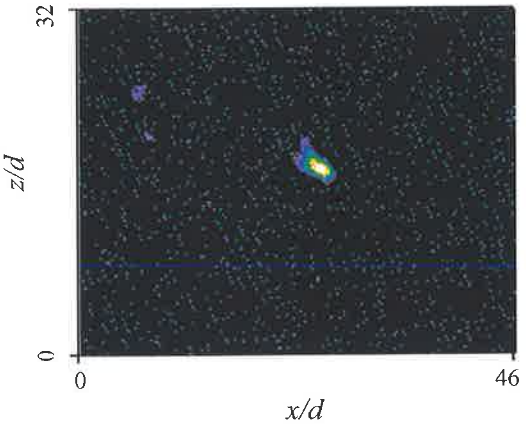

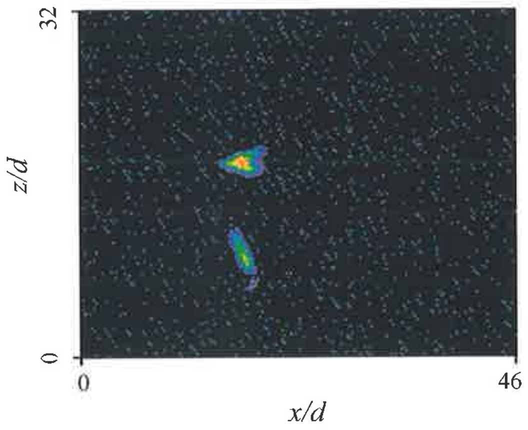

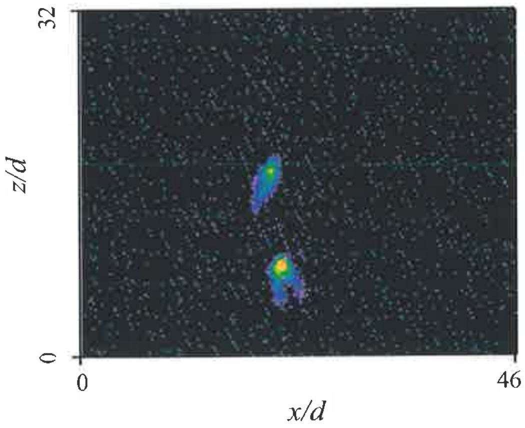

Appendix A-63

1. Experimental Conditions

Re 7682= ; $St = 0.0059$; $f = 30\ Hz$; $P = 8\ kPa$; $U_0 = 25.40 m\ s^{-1}$

2. Typical Images from the Zones of Soot Formation

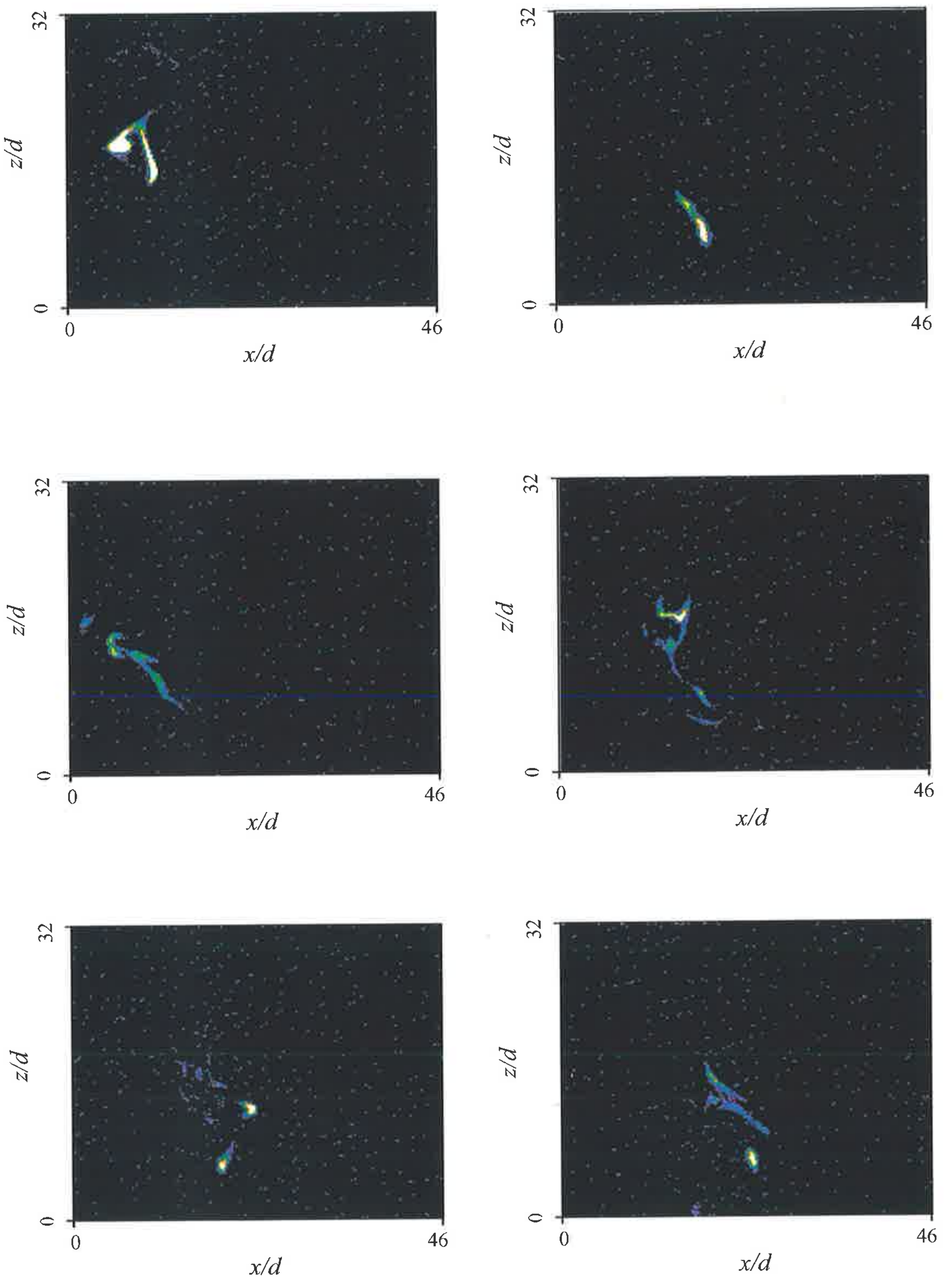

Appendix A-64

1. Experimental Conditions

$Re = 7682$; $St = 0.0079$; $f = 40\ Hz$; $P = 8\ kPa$; $U_0 = 25.40\ m\ s^{-1}$

2. Typical Images from the Zones of Soot Formation

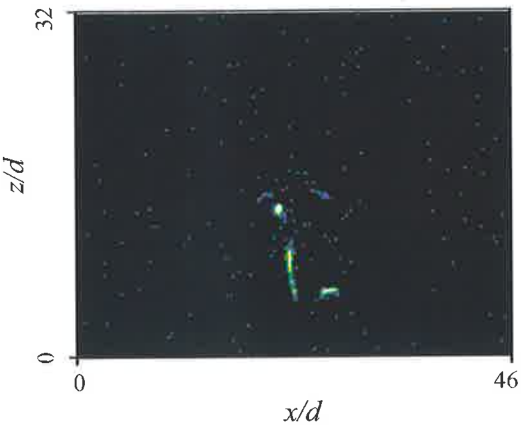

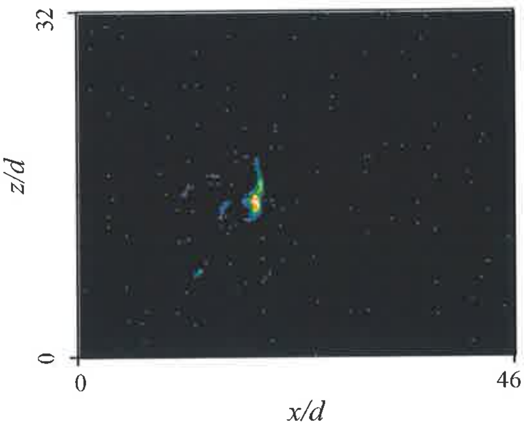

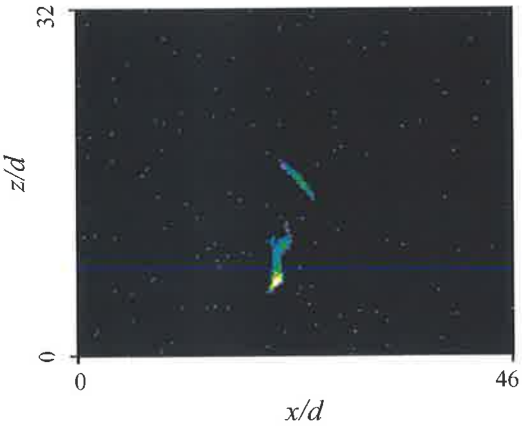

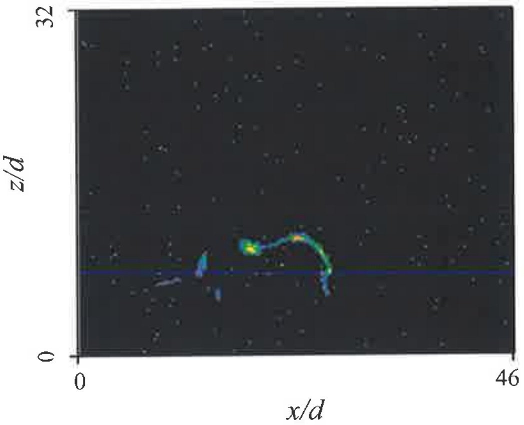

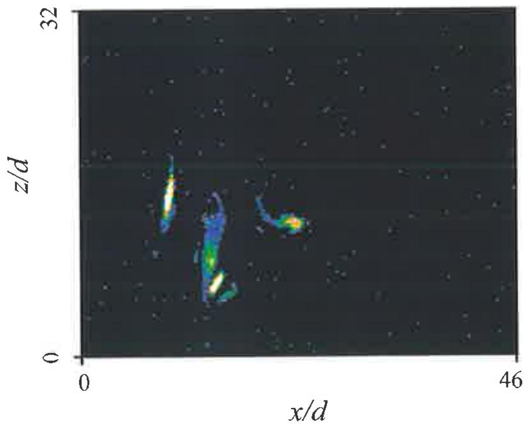

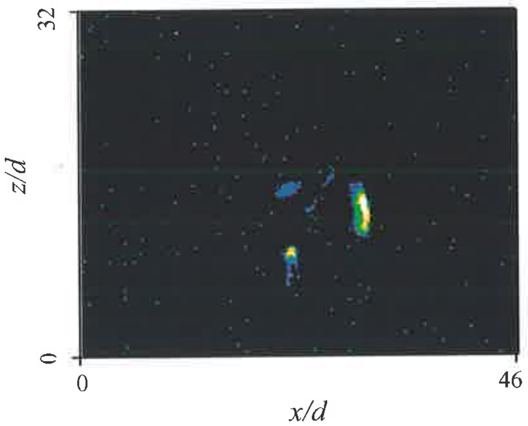

Appendix A-65

1. Experimental Conditions

$Re = 7682$; $St = 0.0099$; $f = 50\ Hz$; $P = 8\ kPa$; $U_0 = 25.40\ m\ s^{-1}$

2. Typical Images from the Zones of Soot Formation

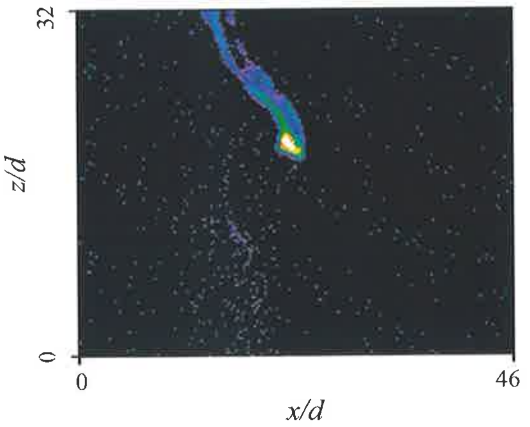

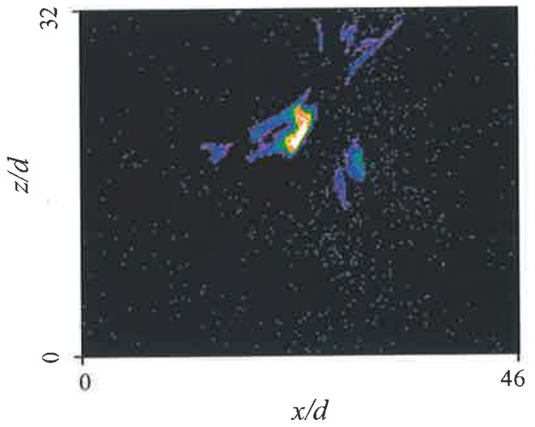

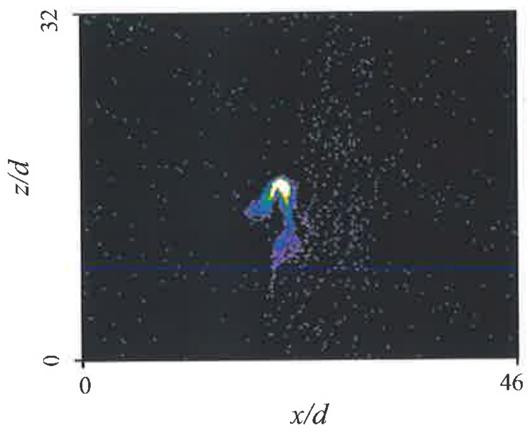

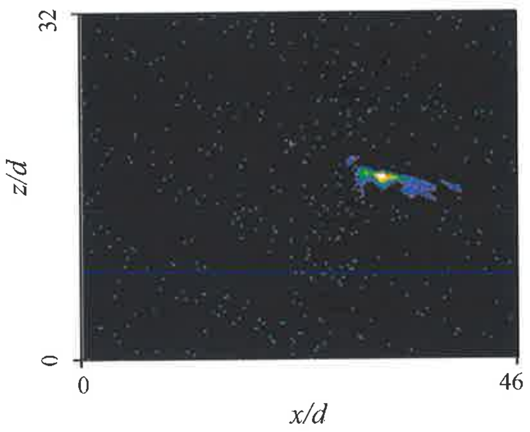

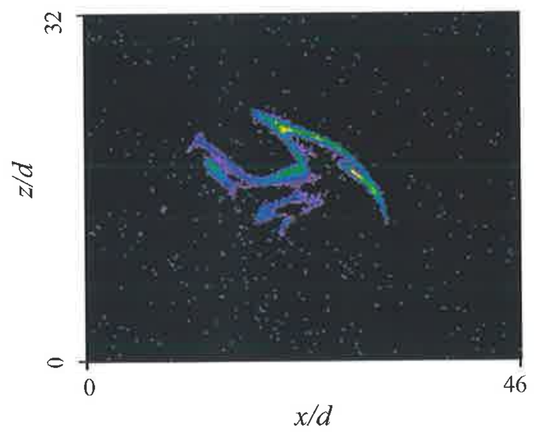

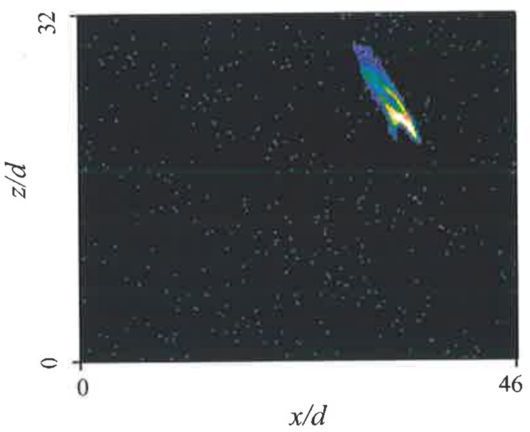

Appendix A-66

1. Experimental Conditions

$Re = 8840$; $St = 0.0046$; $f = 26.6\ Hz$; $P = 9.5\ kPa$; $U_0 = 29.20\ m\ s^{-1}$

2. Typical Images from the Zones of Soot Formation

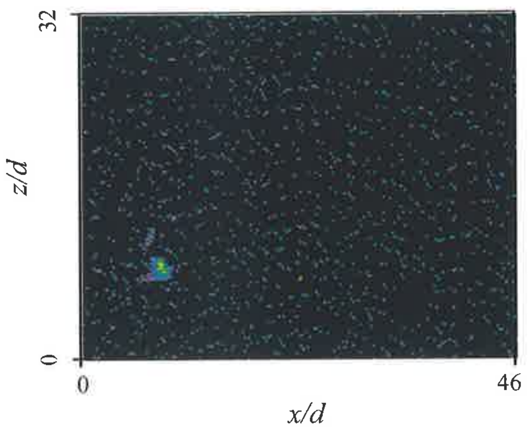

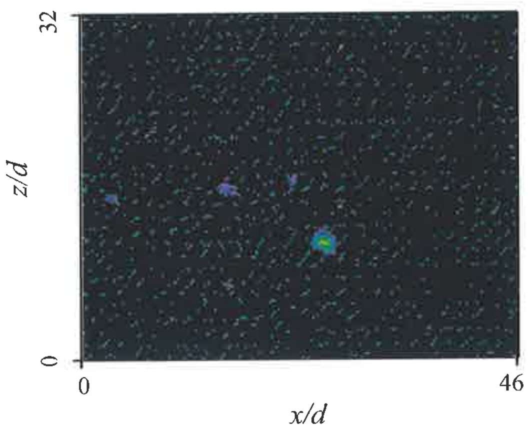

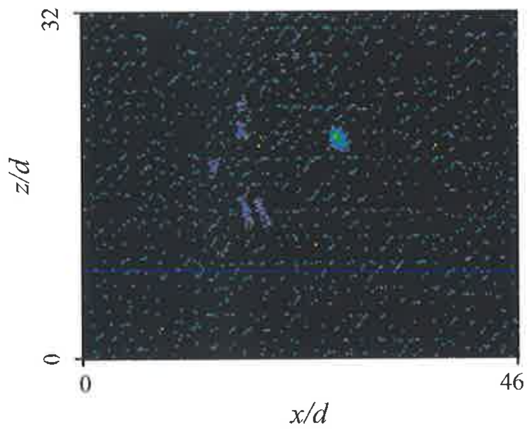

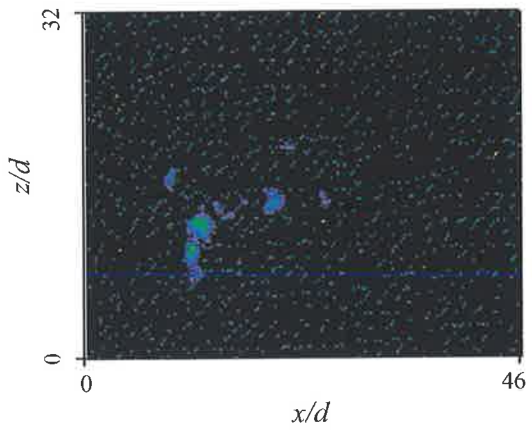

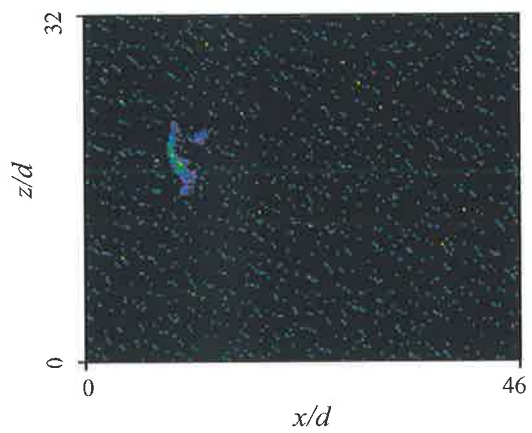

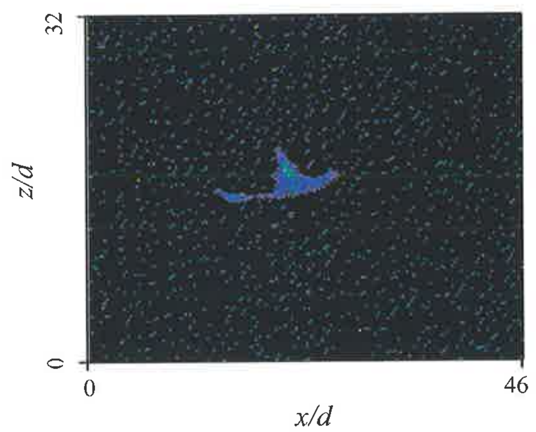

Appendix A-67

1. Experimental Conditions

$Re = 8840$; $St = 0.0077$; $f = 45\ Hz$; $P = 9.5\ kPa$; $U_0 = 29.20\ m\ s^{-1}$

2. Typical Images from the Zones of Soot Formation

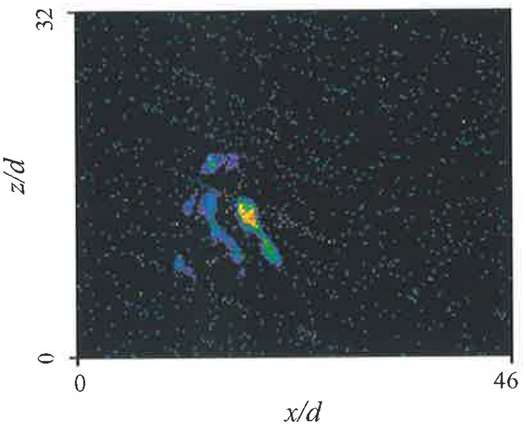

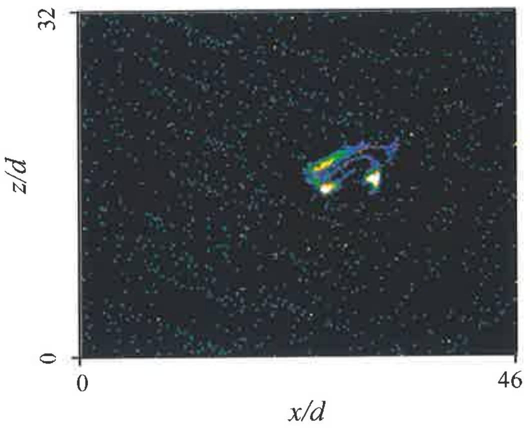

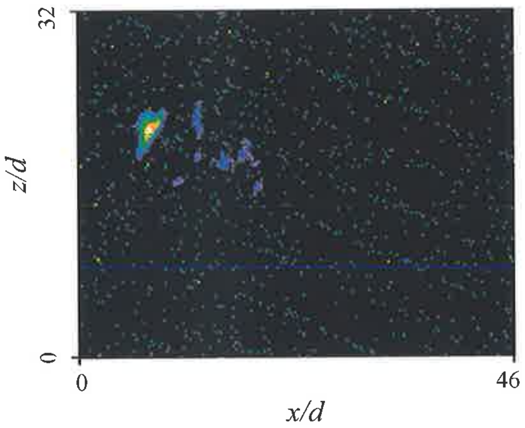

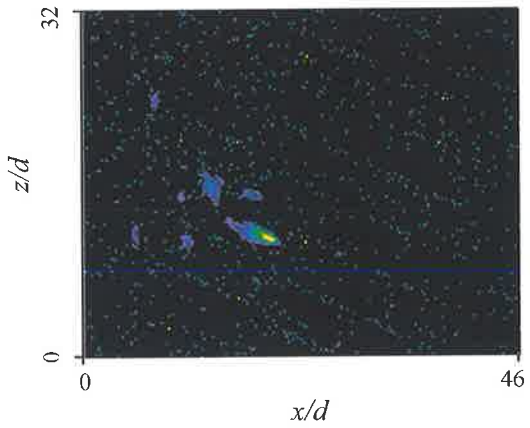

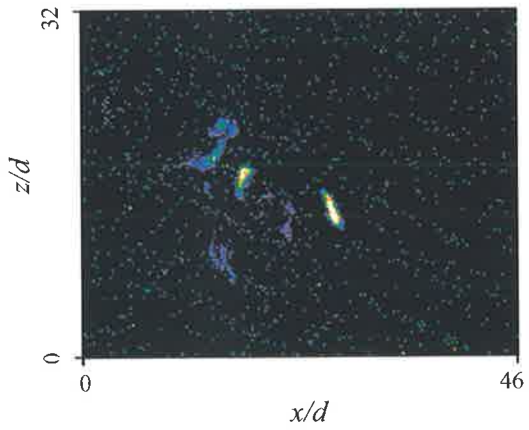

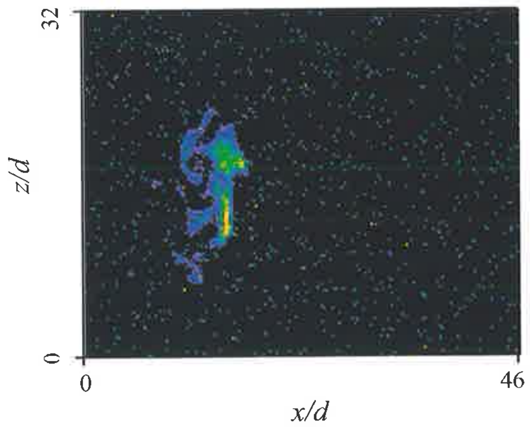

Appendix A-68

1. Experimental Conditions

$Re = 8840$; $St = 0.0113$; $f = 66\ Hz$; $P = 9.5\ kPa$; $U_0 = 29.20\ m\ s^{-1}$

2. Typical Images from the Zones of Soot Formation

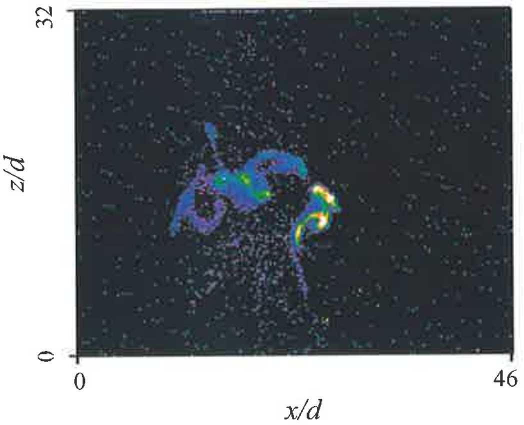

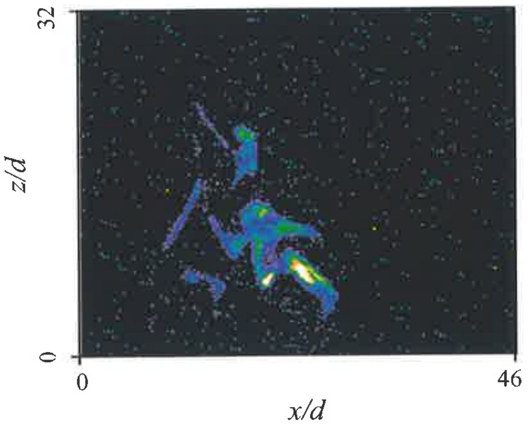

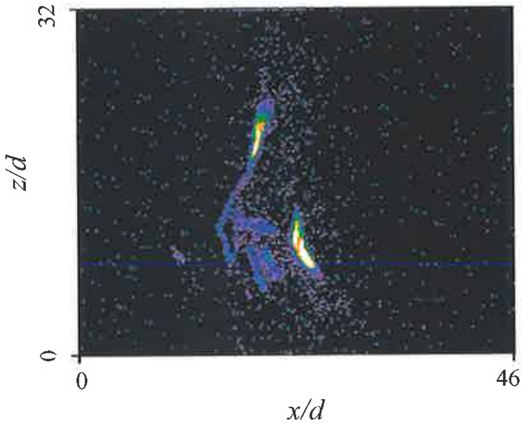

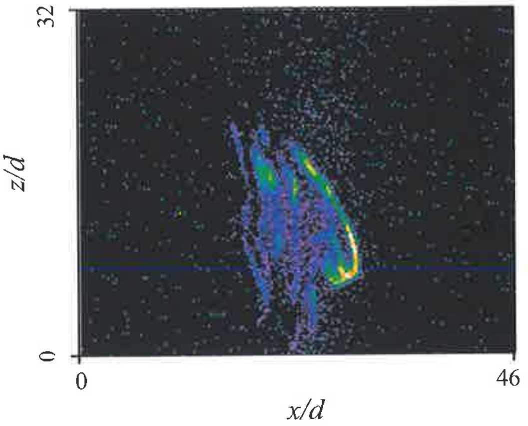

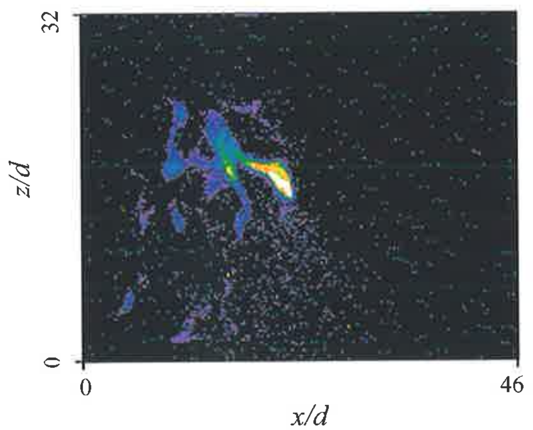

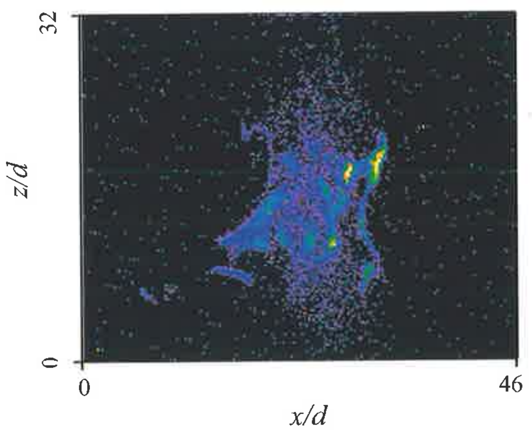

Appendix A-69

1. Experimental Conditions

$Re = 10012$; $St = 0.0061$; $f = 40\ Hz$; $P = 11\ kPa$; $U_0 = 33.08\ m\ s^{-1}$

2. Typical Images from the Zones of Soot Formation

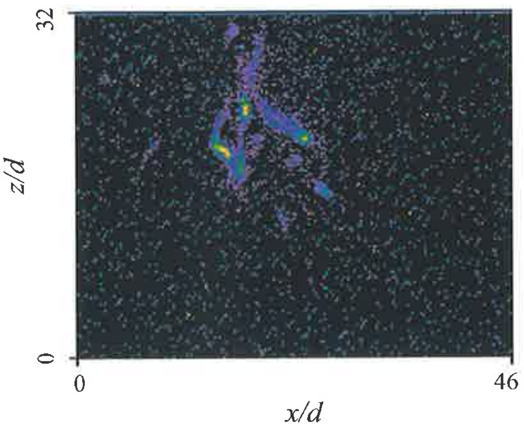

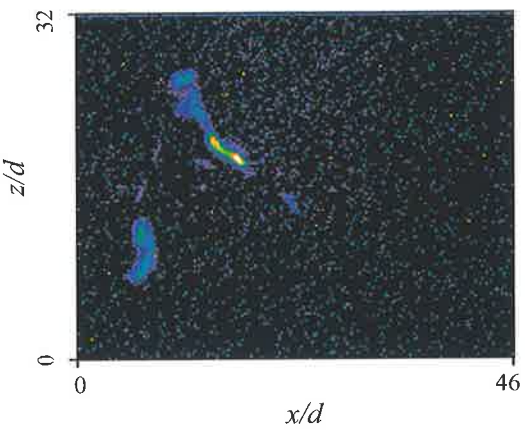

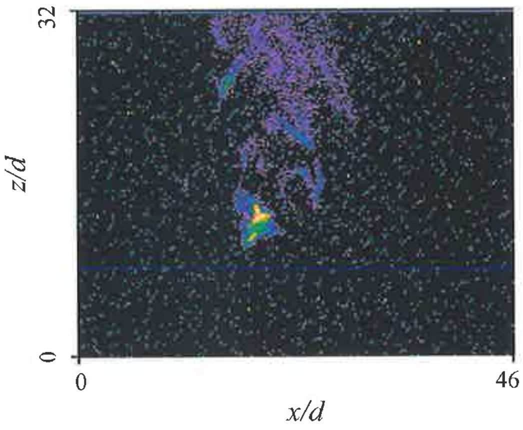

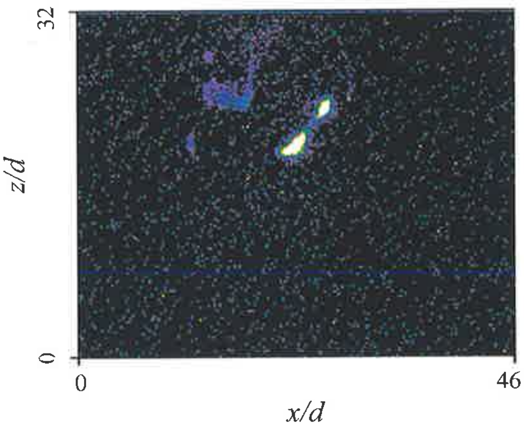

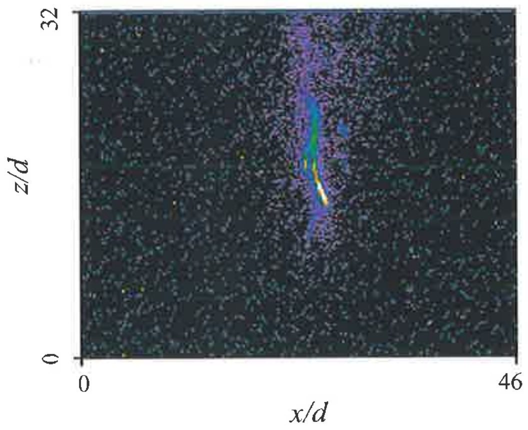

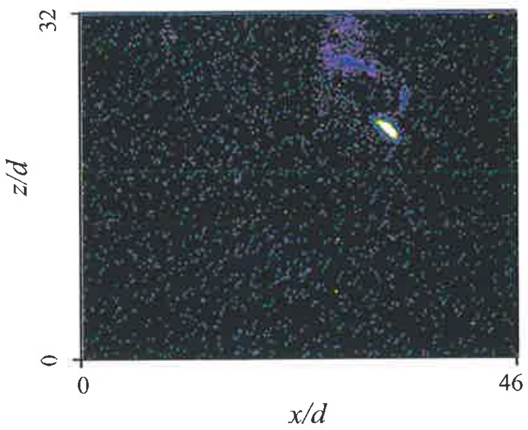

Appendix A-70

1. Experimental Conditions

$Re = 11223$; $St = 0.0049$; $f = 36\ Hz$; $P = 13\ kPa$; $U_0 = 37.08\ m\ s^{-1}$

2. Typical Images from the Zones of Soot Formation

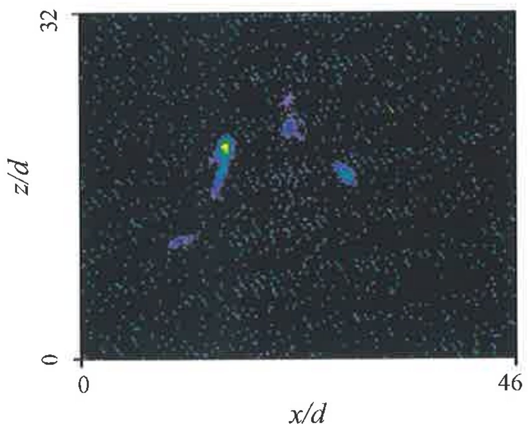

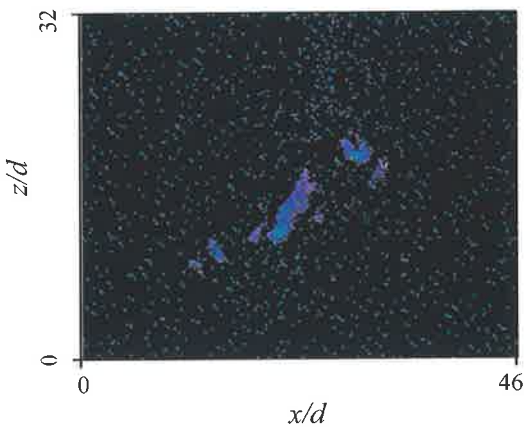

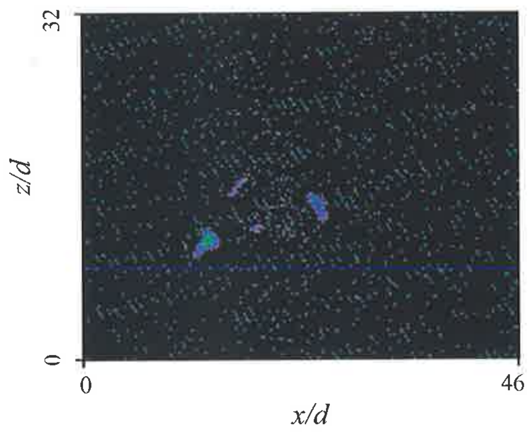

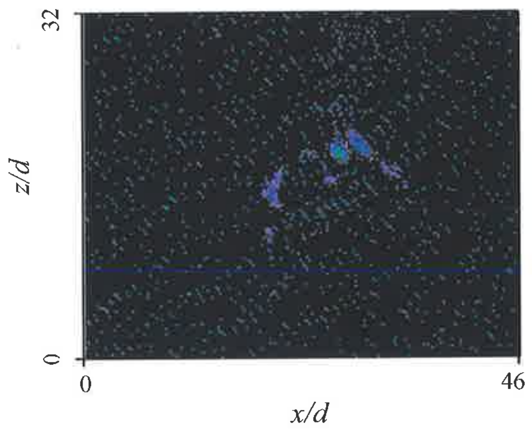

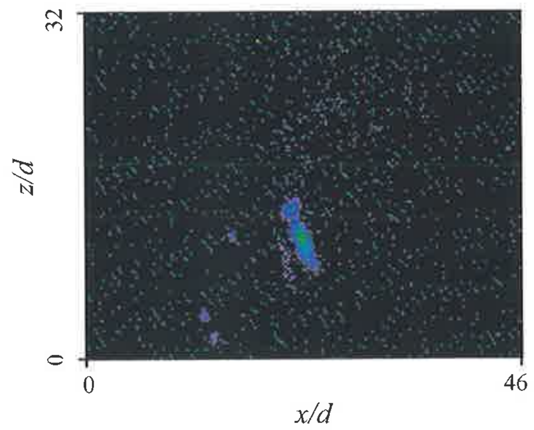

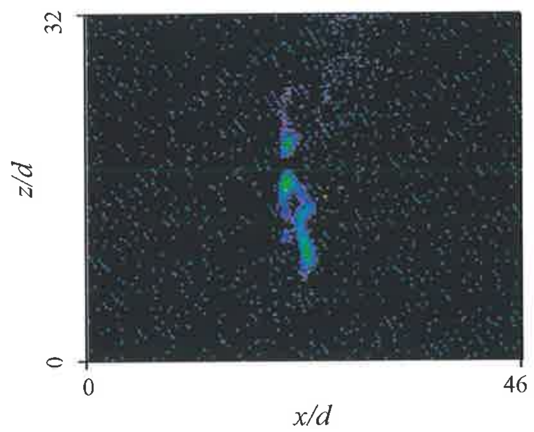

Appendix A-71

1. Experimental Conditions

$Re = 11223$; $St = 0.0094$; $f = 70\ Hz$; $P = 13\ kPa$; $U_0 = 37.08\ m\,s^{-1}$

2. Typical Images from the Zones of Soot Formation

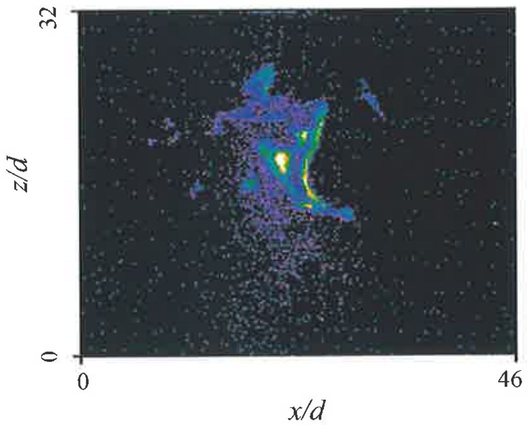

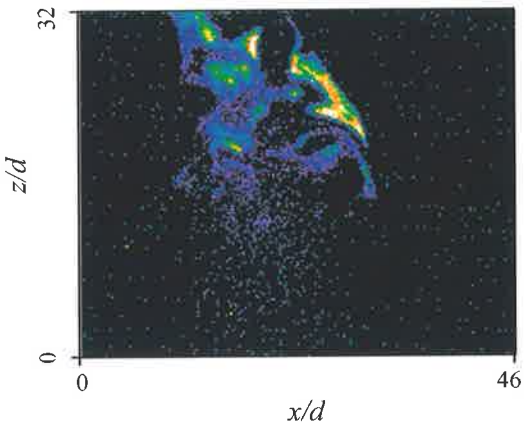

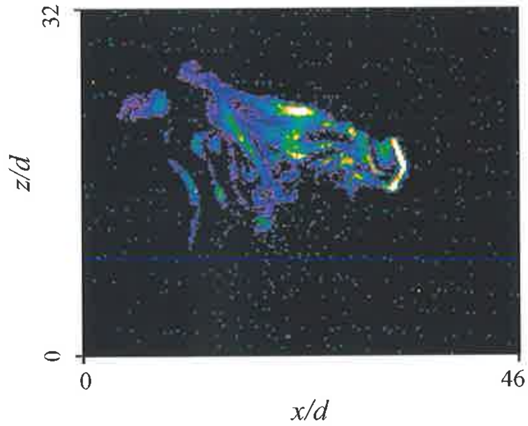

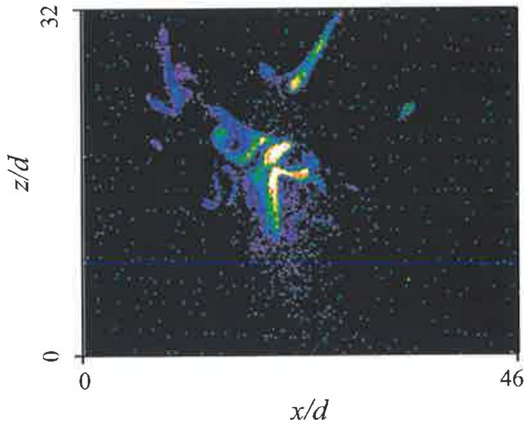

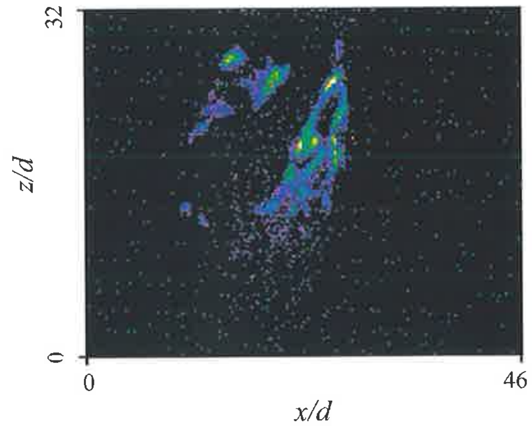

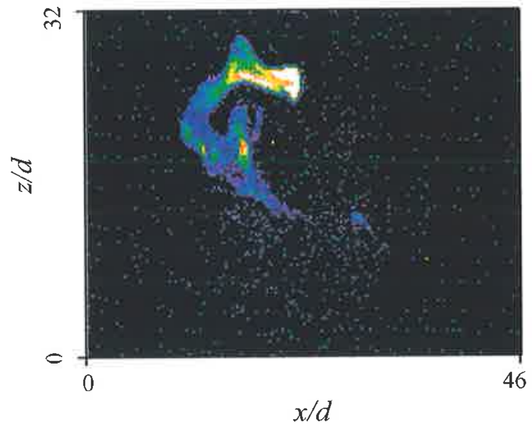

Appendix B

Visual Examination of Zones of High Luminosity

The first aim of this investigation was to estimate the height and width of flames produced by the mechanical precessing jet (MPJ) nozzle for different conditions of flow and frequency of precession, and correspondingly, to locate the zones of high luminosity (these are the zones of high soot volume fraction), [so that Mie scattering images could be taken of these regions.]

1. Experimental Equipment

The experimental system is illustrated by the schematic diagram shown in Figure B-1. The performance characteristics of most of the equipment (MPJ Burner, Gas Controlling Board, etc.) are given in Chapter 3.

The data acquisition equipment included a digital video camera (model DCR-TRV900E), together with focusing and filtering devices. The specification of the camera is given in Table B. The field of view of the camera could be altered by adjusting the distance between the flame to be imaged and the camera. The distance between the camera and the flame was fixed at 2.5 *m*, which allowed the capturing of the entire flame. Images were initially taken using five different shutter speeds for each condition (300, 600, 1000, 1250 and 1750). The images were then examined, and the highest shutter speed (1750) selected for further use.

Appendix B

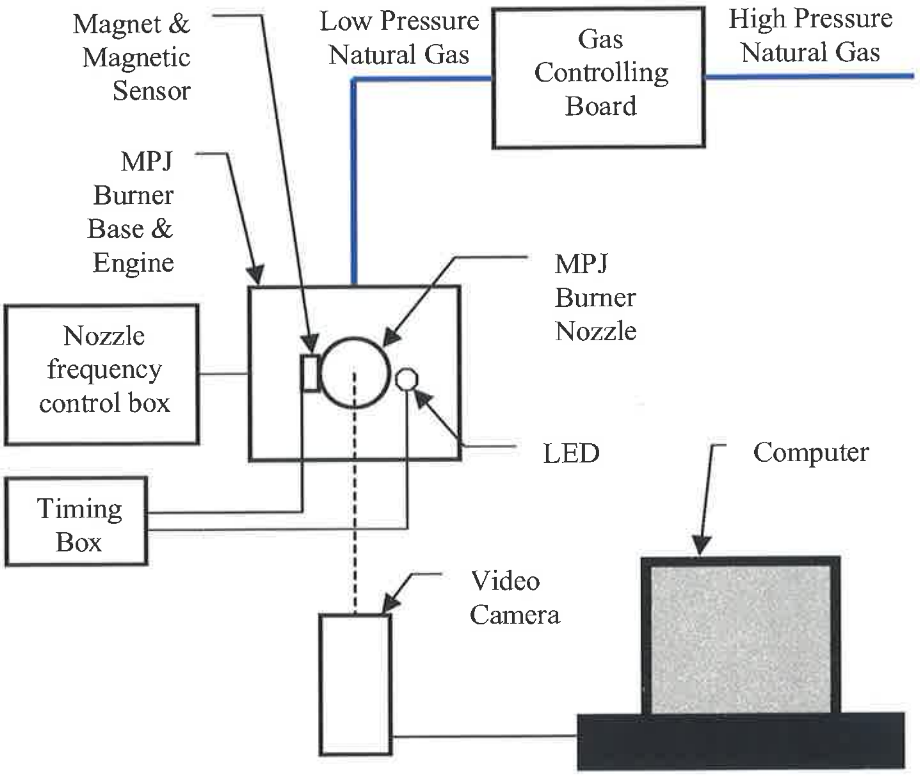

Fig. B-1. A schematic diagram of the experimental system used to determine flame height, width and zones of high luminosity.

Table B. Specification of digital video camera (model DCR-TRV900E), Sony (1998).

Image device	3CCD (Charge Coupled Device ¼"), 32 bit
Lens	Combined power zoom lens, 48× (digital), 12× (optical)
Focal distance	from 4.3 to 51.6 *mm*
Illumination range	from 4 to 100 000 *lux*
Frame frequency	25 s^{-1}
Shutter frequency	from 4 to 10000 s^{-1}

Appendix B

A high shutter speed is favourable, as it reduces the likelihood of saturation of same pixels when images are taken. The shutter speed had to be low enough, however, to allow the light from the LED to be seen[1].

Before carrying out the experiment, standard operating procedures were established for starting up and shutting down of the flame, as well as safety and emergency procedures. These procedures were approved by the safety officer of the School of Chemical Engineering at the University of Adelaide. A full risk assessment and hazard identification checklist were also written up and approved.

A) Start-up Procedure

The start-up procedure included a sequence of the following steps:

1. Ensure suction fan of exhaust duct is on.
2. Check that fuel on/off valve is closed.
3. Open valve on bottle and set operating pressure using regulator.
4. Select suitable frequency of rotation of the electrical engine using the control box.
5. Open fuel on/off valve.
6. Select suitable low gas flow rate for ignition.
7. Ignite the natural gas.
8. Turn on the control box.

---

[1] To provide a phase reference for the determination of conditionally averaged images, a high-intensity LED was attached to the timing box and placed in the field of view of the camera. A magnetic Hall-effect sensor was mounted to the rotating base of the MPJ burner to generate a triggering pulse with each rotation. The LED was energised for 1.1 *ms* following each signal from the sensor.

9. Select suitable shutter speed on the video camera.
10. Turn on the video camera.

B) Data Collection

Filming was carried out in the dark to minimise background noise. For each condition, the flame was filmed for approximately 20 seconds. For each condition, approximately 10 images were downloaded from the camera onto the computer. Images were selected from the camera corresponding to the [diode light] being on. This indicated that the magnet on the nozzle had passed the magnetic sensor and a signal had been sent to the timing box at a constant phase of the nozzle relative to the camera.

C) Shut-down Procedure

1. Turn off the video camera.
2. Reduce the flow rate to minimum.
3. Turn off the fuel on/off valve.
4. Turn off the engine.
5. Turn off the valve at the gas cylinder.

2. Experimental Results

A range of conditionally sampled experiments was carried out at various combinations of *Re* and *St* numbers from 4329 and 0.0042 to 11223 and 0.0245, respectively, nozzle diameter of

5 *mm* and the jet exit angle of 45 degrees. Typical visual images of the flames for the selected cases at various *Re* and *St* numbers are shown in Figure B-2. The size of the visual images is fixed on 27 *cm* width and 44 *cm* height. The bright yellow colour is produced by the soot particles.

It was found that the flame size and shape were variable and they depended on the required experimental conditions (*Re* and *St* numbers). The flame height increases, while the width decreases with the increase of *Re* number. The change of the *St* number does not impact significantly on the flame size. The flame luminosity increased with increase in both *Re* and *St* numbers, however, the latter was more influential.

Since the size of the image field of the ICCD camera used for the instantaneous Mie scattering imaging is much smaller (0.23 *m* × 0.16 *m*) than the actual flame size (typically 0.25 *m* × 0.4 *m*), only selected areas of the flame could be captured. The distance between the axis of the laser beam and the top of the MPJ burner was chosen to be 0.15 *m*. The instantaneous Mie scattering images were taken from the area with height of 0.16 *m*, symmetrically located along the laser beam axis.

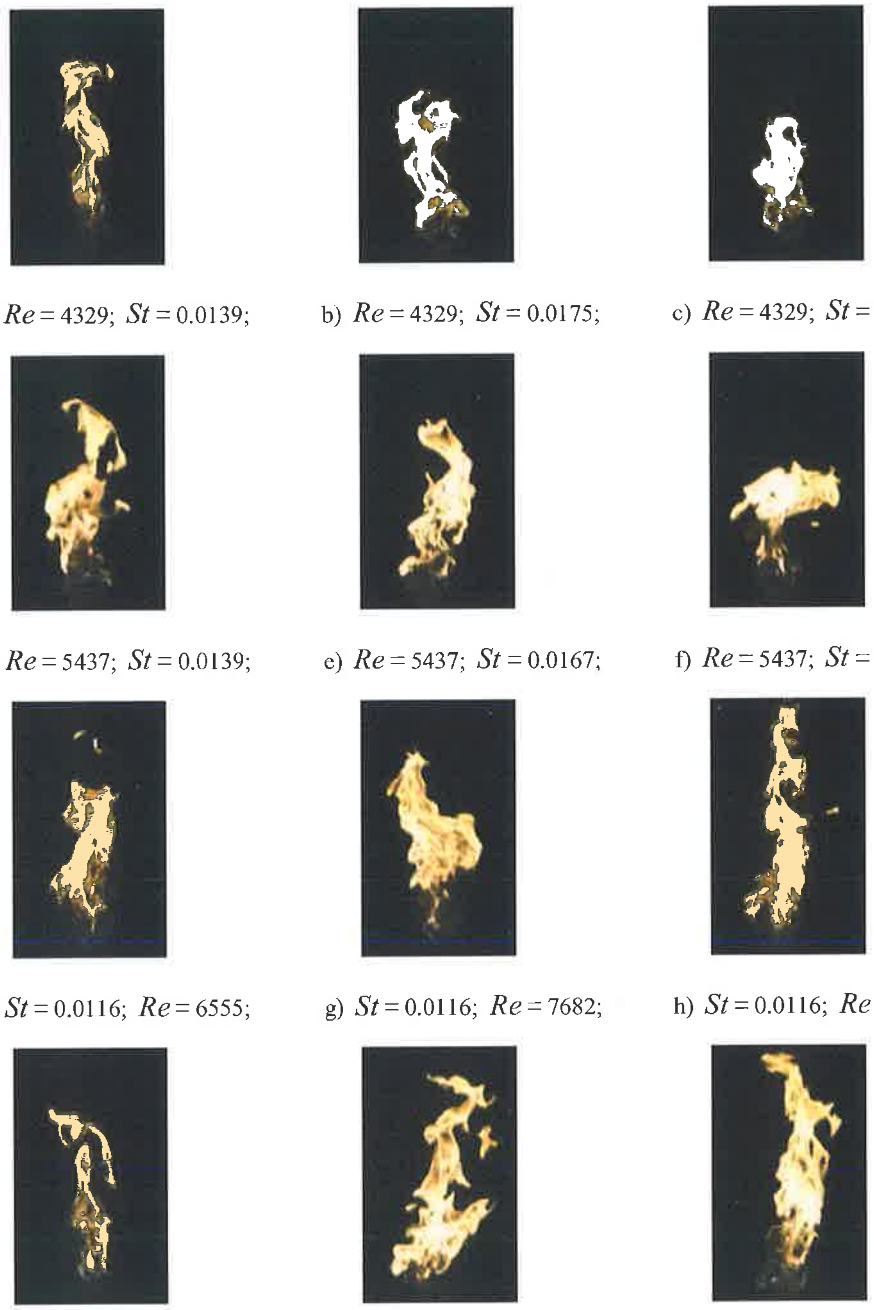

a) $Re = 4329$; $St = 0.0139$; b) $Re = 4329$; $St = 0.0175$; c) $Re = 4329$; $St = 0.0245$;

d) $Re = 5437$; $St = 0.0139$; e) $Re = 5437$; $St = 0.0167$; f) $Re = 5437$; $St = 0.0195$;

f) $St = 0.0116$; $Re = 6555$; g) $St = 0.0116$; $Re = 7682$; h) $St = 0.0116$; $Re = 8840$;

i) $St = 0.0139$; $Re = 4329$; j) $St = 0.0139$; $Re = 6555$; k) $St = 0.0139$; $Re = 7682$;

Fig. B-2. Typical images of the visual flames for the selected cases at various *Re* and *St* numbers. The size of the visual images is fixed on 27 *cm* width and 44 cm height.